THESIS FOR THE DEGREE OF LICENCIATE OF ENGINEERING

Characterization of Different Interface Types for HVDC Extruded Cable Applications

ESPEN H. DOEDENS

High Voltage Engineering
Department of Electrical Engineering
CHALMERS UNIVERSITY OF TECHNOLOGY
Gothenburg, Sweden 2018

Characterization of Different Interface Types for HVDC Extruded Cable Interfaces.
ESPEN H. DOEDENS

ISSN 1403-226X
Technical report no. R004/2018

High Voltage Engineering
Department of Electrical Engineering
Chalmers University of Technology
SE-412 96 Gothenburg
Sweden
Telephone + 46 (0)31-772 1000

Cover:
HVDC extruded cable end on the beach ready for jointing. Further explanation of the layers in the HVDC extruded cable can be found under section 2.1. With inset illustrations (top to bottom): impact of surface roughness on charge injection (found in section 2.3.3.1), SEM of an abraded surface (found in section 4.1.1), remolded breakdown channel observed from above (found in section 4.2.1.1) and a band gap illustration of the cable end (found in section 4.2.1.1). The background illustration is a private photo taken at the beach of Redwood creek picnic area, Reading rock state marine conservation area, California, USA. This is not an actual installation of an extruded HVDC system.

Chalmers Bibliotek, Reproservice
Gothenburg, Sweden 2018

“A physical experiment which makes a bang is always worth more than a quiet one. Therefore, a man cannot strongly enough ask of Heaven: if it wants to let him discover something, may it be something that makes a bang. It will resound into eternity.”

– Lichtenberg, Georg Christoph, and Albert Leitzmann. 1906.

Abstract

In extruded HVDC cable systems a variety of interface types can be found, and the interfacial properties depend on the application within the system. Such applications can be joints, terminations or the cable itself and they all have different material combinations and manufacturing methods. To ensure at least 40 years of faultless operation of the cable system and its interfaces, proper design and quality control is essential. This requires detailed knowledge on how physical, measurable quantities of polymer surfaces relate to electrical characteristics such as electric field and space charge accumulation. This work aims to expand our understanding by assessing polymer surfaces created with different, industrializable preparation methods resulting in varying degrees of surface roughness. Breakdown tests, charge decay measurements, optical profilometry and other characterization methods have been performed on cable peelings created from full-sized HVDC cables. It was found that, depending on preparation method, very different roughness levels and textures are created on the polymer surfaces. There were also other impacts of the preparation method found, such as altered surface morphology or the introduction of surface states. A clear relation between surface roughness and the localized field distribution was found, which mainly depended on the arithmetical surface height parameter Sa, but also to a minor degree on the shape of the surface texture. Field dependent bulk conductivity was found to reduce the tail in the surface field distribution histogram, but was not able to fully remove the distribution itself. The surface field distribution showed to have a clear impact on space charge injection, and was capable of creating a field threshold effect. This effect could not be accounted for by a fixed field parameter in the Schottky equation. In this work, charge injection was assumed to be the sum of Schottky and Fowler-Nordheim injection, which resulted in a very significant increase in charge injection above the threshold field. This led to bulk-limited charge injection above the threshold field, along with significant homocharge accumulation. Increased roughness was observed to reduce the breakdown field in the tested samples, which for the larger test objects scaled well with the calculated threshold fields. For the cable peelings, an impact of surface roughness was found as well, but at significantly higher field levels. The origin of this scaling effect is further discussed in this thesis. The threshold fields were also found for rough surfaces in the charge decay measurement. By utilizing rough ground electrodes, significantly higher decay currents were measured above the field thresholds. The increase in decay speed is related to opposite charge injection during the poling phase before the measurement. The findings of this work are believed to be applicable to many high voltage applications, especially in cases where solid insulation with low conductivity is used at high electric fields.

Keywords: HVDC, extruded cable, XLPE, interfaces, polymer surfaces, cable peelings, DC breakdown, Charge decay, Voltage decay, Roughness, Field enhancement factors, Charge injection, Schottky injection, Fowler-Nordheim injection, Roughness assisted charge injection.

Sammanfattning

Extruderade HVDC-kabelsystem kan innehålla många olika gränsytor, där de faktiska egenskaperna beror på själva applikationen i systemet. Applikationerna kan vara skarvar, termineringar eller själva kabeln och dessa har olika materialkombinationer och tillverkningsmetoder. För att säkerställa 40 år felfri drift för kabelsystemet och dess gränssnitt, är det viktigt med rätt design och noggrann kvalitetsäkerställning. Detta kräver goda kunskaper om hur fysiska, mätbara parametrar för polymera gränsytor påverkar elektriska egenskaper såsom elektriskt fält och laddningsackumulation. Detta arbete syftar till att öka denna förståelse genom att utvärdera polymeriska ytor skapade genom olika, industrialiserbara prepareringsmetoder som leder till olika grader av ytråhet. Genomslagstester, ytladdningsmätningar, optisk profilometri och andra karakteriseringsmetoder har genomförts på kabelsnitt tagna från fullskala HVDC-kablar. En mycket varierande grad av ytråhet och ytstruktur blev uppmätt på ytan, beroende på prepareringsmetoden. Även annan inverkan av prepareringsmetoden observerades såsom ändrad ytmorfologi eller introduktionen av yttillstånd. En tydlig inverkan på lokal fältfördelning mot ytan på grund av ytråheten upptäcktes, som till största del var kopplad till den aritmetiska höjdparametern Sa, men även till viss del av själva ytstrukturen. Fältberoende ledningsegenskaper i bulken mildrade effekten av fältfördelningen, men lyckades inte ta bort den helt. Fältfördelningen hade en tydlig inverkan på laddningsinjektion, och ledde till en tröskeleffekt som inte kan förutses genom en fältparameter i Schottky ekvationen. I detta arbete antogs laddningsinjektionen var summan av Schottky injektion och Fowler-Nordheim injektion, vilket ledde till en signifikant ökning av strömtäthet över fälttröskeln. Detta kan leda till att laddningsinjektionen över tröskeln blir begränsad av bulkeffekter, där lokalt hög densitet av laddning samlas med samma polaritet som elektroden. Låg genomslagshållfasthet upptäcktes för de råaste ytorna på större testobjekt, vilka korrelerade bra med fältröskeln. För kabelsnitten, så fanns det också en inverkan av ytråhet, fast med mycket högre hållfasthet än de större testobjekten. Orsaken till denna skalningseffekt diskuteras vidare i avhandlingen. De elektriska fält-trösklarna blev även uppmätta på de råaste ytorna genom ytladdningsmätning. Genom att använda råa ytor på jordsidan i denna test, kunde mycket högre strömtäthet uppmätas över fälttröskeln. Ökningen av strömtäthet är relaterad till injektion av laddningsbärare med motsatt polaritet under polningsfasen innan mätningen. Upptäckterna i detta arbete tros vara applicerbara för många högspänningsapplikationer, speciellt i fall där solid isolation med låg ledningsförmåga utsätts för höga elektriska fält.

Acknowledgements

Nexans Norway AS is greatly acknowledged for the funding and the opportunity they have provided for this work.

I want to start by giving my deepest acknowledgement to my parents, Folkert Barkhuyzen and Geertje Doedens, who throughout my youth have supported me in my education and have contributed towards the development of my practical abilities, through the many projects and endeavors we faced together. Next, I would like to thank my wife, Louise Doedens, for her love and support throughout the thesis. I would also like to thank Maja Lif for putting a roof over our heads.

Next, to give meaning to the expression "standing on the shoulders of giants", I would like to express my gratitude for my mentors who have contributed greatly to my personal development. Here, Jan Varreng is deeply acknowledged for his mentorship and positive attitude towards research and high voltage engineering. Dr. Christian Frohne is acknowledged for his contributions to this thesis, and support for the realization of this project. Professor Stanislaw Gubanski is acknowledged for his mentorship in this project, and in my previous scientific work. I would also like to thank Dr. Markus Jarvid for his theoretical insights and for supervising this Licenciate thesis.

For giving me the opportunity to realize this research, I would like to thank my manager, Per-Arne Osborg and the project manager of the Norwegian HVDC extruded team, Dr. Roberto Gaspari.

For aid with the performed measurements, I would like to thank Jan-Are Sundby for carrying out the FTIR-ATR measurements and Andreas Nyborg for carrying out the HPLC analysis in this thesis. I would also like to thank Dr. Dimitri Charrier for the exchange of knowledge and expertise. Also Dr. Xiangdong Xu is acknowledged for theoretical discussions and for creating the software used in the DCBD experiments. Professor Yuriy Serdyuk is acknowledged for theoretical discussion and for aid in carrying out the calculation of field enhancement factors.

Brynjar Jacobsen and Nils-Bertil Frisk are acknowledged for their flawless execution of my past role in the extruded HVDC project, allowing me to fully focus on this thesis. All other members of the Nexans extruded HVDC project are also acknowledged for their research contributions. Together we have developed a robust cable system, and have done so by constructing a solid foundation of theoretical and practical expertise.

Espen Doedens

Gothenburg, Sweden

April, 2018

List of abbreviations

HVDC – High Voltage Direct Current
HVAC – High Voltage Alternating Current
MI - Mass Impregnated
GIS – Gas Insulated Switchgear
LDPE – Low Density Polyethylene
HDPE – High Density Polyethylene
XLPE – Crosslinked Polyethylene
PDP – Peroxide Decomposition Products
CB - Carbon Black
SC - Semiconductor
PD - Partial Discharges
SFE – Surface Free Energy
MWS – Maxwell Wagner Sillars
SE - Schrödingers Equation
DOS – Density Of States
FEM – Finite Element Method
FEF – Field Enhancement Factor
HPLC – High Performance Liquid Chromatography
FTIR – Fourier Transform Infrared Spectroscopy
ATR - Attenuated Total Reflection
SPD – Surface Potential Decay
DCBD – Direct Current Break Down
BD – Breakdown
PEA – Pulsed Electroacoustic measurement

Table of Contents

Chapter 1

Introduction

Today only around 10% of global energy consumption originates from renewable resources [1]. According to BP:s energy forecast [1], electric power contributes with 42% to the total energy usage, while for example the transport sector contributes by 19%. The use of renewable energy sources not only protects the intrinsic value of nature and the environment by reducing CO_2 emissions, but also increases the intra-generational justice by preserving fossil fuels for non-substitutable materials in future manufacturing processes and products. The carbon intensity of European electricity generation is shown below in Figure 1. The amount of renewable energy resources integrated in the power grid is in direct relation to the magnitude of greenhouse gas emissions, which in turn is dependent on geographical location.

CO_2 intensity in the European power grid

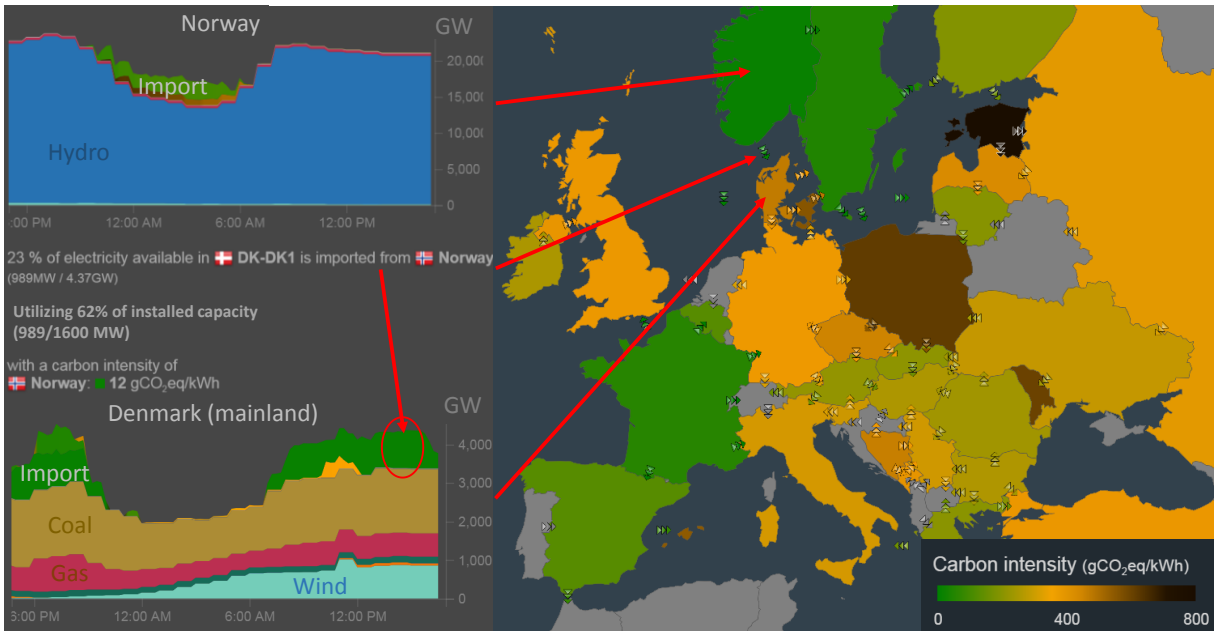

Figure 1. CO_2 intensity of European electric power generation on 13/3-2018 taken from "www.electricitymap.org" [2]*. The color bar indicates the degree of CO_2 emissions in gCO_2/kWh. The daily export from Norway to Denmark through the Skagerrak interconnection is shown to the left in the figure.*

The implementation of renewables for electric power generation has multiple difficulties to overcome:

1. Fluctuations in power output
2. Remoteness to urban areas where electric power is consumed
3. Long investment pay-back times for some of the technologies

Land based and submarine high voltage direct current (HVDC) transmission links are at the core of overcoming the above challenges. By utilizing HVDC transmission separate power grids can be interconnected in order to minimize load imbalances. Conventional mass impregnated (MI) HVDC cable systems have been around for many years and account for much

of the submarine transmission today. In Figure 1 the cross-border export of the 1.6 GW Skagerrak power transmission system (consisting of 4 MI cable systems) is highlighted and shows a utilized power transmission of 989 MW, transporting abundant Norwegian hydropower to compensate for a daily lack of wind power in Denmark and Germany. High voltage cables utilizing crosslinked polyethylene (XLPE) as insulating material, such as HVDC extruded cable systems, have in recent years entered the market. Thanks to development of voltage source converter (VSC) technology, polarity reversals are no longer required for power flow inversion. This development along with improvements to the base material of the insulation system, have led to the recent development of the 320kV HVDC cable technology [3] with further development ongoing. The power rating of the 320 kV DolWin 6 bipole HVDC extruded cable link is planned to be around 450 MW per pole/cable [4]. This new HVDC extruded technology is very competitive compared to traditional MI systems thanks to a higher maximal operation temperature and simplified jointing methods in the field.

Other benefits of using HVDC are that the transmission losses for HVDC links are typically lower than conventional high voltage alternating current (HVAC) systems when long transmission lengths are needed. Using HVDC cables instead of overhead lines for transmission also makes for less impact on the local environment and is the only practical solution for long submarine transmission lengths.

1.1 Background

An HVDC cable link is not complete without the cable accessories used in the application. Such accessories, such as joints and terminations, introduce material interfaces into the complex electrical system. Such interfaces, if poorly designed, can introduce weak points in the system and ultimately lead to premature failure leading to an outage of the entire cable system. Reliability is a key design factor for cable systems, and is closely related to the investment pay-back time. It is thus of absolute necessity to ensure the reliability of these interfaces through the lifespan of the cable system in order for the new HVDC extruded cable systems to compete with the proven in service reliability of MI HVDC systems exceeding 40 years of operational life time. The difficulty is that the nature of these material interfaces is still far from fully understood, which is also highlighted from the vast amount of research ongoing within this area. Guidance towards improved reliability and increased transmission capacity (by means of increased electrical field withstand level) could be the outcome of this research.

1.2 Purpose

The main purpose of this thesis is to further investigate the impact of physical surface preparations on the performance of cable accessories. In this work simplification of the real joints and terminations into cable peelings and other simplified geometries has been made in order to ensure a high statistical certainty in the results. Though, to keep the nature of the interface and material parameters unchanged in this downscaling, the samples themselves have been taken from full-scale cable accessories provided by Nexans Norway AS. Also, tests on medium voltage sized cables have been performed to ensure the scalability and applicability of the test results. This research thus aims directly at improving the understanding of the behavior of material interfaces and surfaces present in the HVDC extruded cable systems for ensuring their reliability in the field.

1.3 Outline of the thesis

Chapter 2 of this thesis begins with a thorough introduction to the HVDC extruded cable and its insulation system. After this the accessories are listed and practical aspects about their interfaces are mentioned. This follows by a review of conduction phenomena, starting in the macroscopic scale, and afterwards introducing conduction phenomena from a microscopic perspective. This follows by a summary of the microscopic conduction phenomena and possible impact from non-ideal surface parameters. Based on this theoretical framework a series of hypotheses are presented in the end of the chapter.

Chapter 3 goes through the used measurement methods to understand the practical aspects and familiarize the reader with the different test setups used for obtaining the results. The development of cable peelings, which has been essential for this work, is also summarized in the beginning of this chapter.

Chapter 4 presents the physical, chemical and electrical findings obtained in the thesis. It contains an analysis on the surface structure through optical profilometry. Chemical analysis was performed such as contact angle measurement, HPLC and FTIR-ATR. The performed electrical measurements, breakdown tests on different geometries and surface potential decay, are presented in the end of this chapter.

Chapter 5 presents the calculation results. It starts with macroscopic field calculations performed on the DC breakdown test setup. This is followed by a thorough analysis of the surface field distribution, which is estimated from the measured roughness profiles in this thesis. Afterwards the surface field distribution is used to estimate the effects on space charge injection. These calculations aid towards understanding the charge decay and breakdown characteristics.

Chapter 6 begins with discussing the limitations in this thesis. After this the hypotheses from the end of chapter 2 are revisited and evaluated further. At last, the most promising hypothesis, hypothesis A-1 is further extended, and used to give an explanation for most of the findings reported in this thesis.

Chapter 7 concludes the most important findings in this thesis. After this also the applicability of the discovered relation between roughness, surface field distribution and charge injection, within other research areas and applications is reflected upon.

Chapter 8 describes the future work required for strengthening the theoretical evidence for the extended hypothesis, as well as additional tests that could lead to further understanding about charge injection and the impact of non-ideal surface parameters.

1.4 List of publications

The following publications were prepared and presented during the course of the project work:

E. H. Doedens, N. B. Frisk, M. Jarvid, L. Boyer, and S. Josefsson, "Surface preparations on MV-sized cable ends for ramped DC breakdown studies," in *2016 IEEE Conference on Electrical Insulation and Dielectric Phenomena (CEIDP)*, 2016, pp. 360–362

E. Doedens, M. Jarvid, S. Gubanski, and C. Frohne, "Cable surface preparation: chemical, physical and electrical characterization and impact on breakdown voltage," in *2017 Jicable HVDC workshop*, 2017.

Under submission:

E. Doedens, M. Jarvid, S. Gubanski, and C. Frohne, "Roughness enhanced charge injection in HVDC extruded cable interfaces," *IEEE Trans. Electr. Insul.*

Chapter 2

Literature review and background

This chapter summarizes the present knowledge that is used within the thesis in order to better understand the nature of interfaces. First a description is made on which type of interfaces are of interest. Next, a macroscopic approach to electric field estimation is presented. At last, a microscopic approach is summarized along with possible theoretical approaches to be used.

2.1 High voltage cables

All HVDC XLPE cables are constructed differently depending on their application. Due to the large impact of material costs, every HVDC cable is design specifically for a certain installation location in order to optimize the design for the required power transmission, thermal environment, voltage level, transient withstand capability and other operating factors. For this reason, no two HVDC cables are exactly the same, though it is possible to divide the family of HVDC XLPE cables into land-based and submarine applications. The major differences between the two applications are in the water blocking technology, installation method and jointing operations. Below in Figure 2, an illustration of a submarine HVDC XLPE cable is shown for sake of highlighting the roles of different layers used in the design.

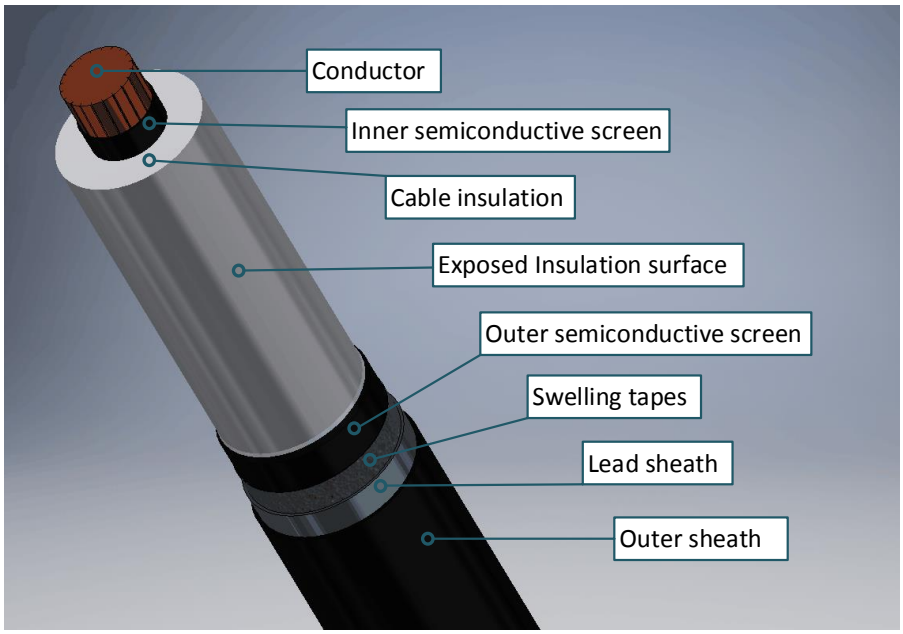

Figure 2. Illustration of a submarine HVDC XLPE cable ready for accessory mating.

As seen in Figure 2 the cable is constructed as follows:

- A copper or aluminum conductor is stranded in a production line. The design of its cross-section can be of the round-wired, sector-shaped, Milliken or solid shape depending on the application. The dimensions of the conductor are designed with the aid of ampacity and mechanical calculations.
- The inner semiconductive layer/conductor screen normally consists of a carbon black loaded XLPE. The smoothness of this layer is essential as any asperities will create

electric field enhancements. This layer is extruded simultaneously with the insulation layer and outer semiconductive layer through a triple extrusion process in order to minimize any possible contamination.

- The insulation layer is extruded along with the inner and outer semiconductive layer in a vertical or horizontal extrusion line. Directly after the extrusion, the cable passes through a long pressurized heat controlled zone for the crosslinking of the three layers, called a continuous vulcanization (CV) line. The thickness of the insulation layer is designed according to voltage level and design stress (electrical field).
- The exposed part of the insulation surface, as shown here, is only uncovered if a certain joint or termination is to be manufactured.
- The outer semiconductive layer is manufactured in the same manner as the inner semiconductive sheath. After the triple extrusion and crosslinking process, the cable is normally spooled to a drum or turntable for degassing in order to remove chemical by-products originating from the cross-linking process.
- The swelling tapes are needed to avoid longitudinal transport of moisture in the case of water ingress as result of a mechanical damage to the radial water barrier during operation. These tapes are lapped over the cable prior to the extrusion of the lead sheath.
- The lead sheath is extruded over the cable and serves as the radial water blocking barrier. For submarine cable designs, such a metallic barrier is crucial as even the tiny amounts of water that can permeate the polymeric sheaths can be enough to change the cable insulation properties significantly. The installation depths for submarine cables also put mechanical requirements on the water barrier as the external seawater pressure will reach high levels.
- The outer sheath is an extruded polymeric sheath which serves as mechanical protection layer for the metallic barrier underneath.
- Additional layers, not displayed in Figure 2 can be various armoring layers covered with polypropylene-yarns. The armoring is designed specifically to withstand the mechanical loading for a certain installation depth and is protected from corrosion with bitumen. The polypropylene yarns prevent the wash out of bitumen and can serve as identification when a different color combination is used for different phases.

The submarine cable is normally produced in certain production lengths, limited by practical factors such as the onset of scorch in the extrusion line. These production lengths are jointed in the factory prior to the armoring process with flexible factory joints. The completed installation length is then shipped to site and installed on the sea bottom. It is often the case that multiple installation lengths are required, as the total length of the link in these cases exceeds the loading capabilities of the installation vessel. Separate installation lengths can be jointed offshore utilizing submarine field joints. When different cable designs are to be used along the installation route, this can be done both by asymmetric factory or asymmetric field joints. When the submarine cable is connected to a section of land cable in a bunker close to the shore line, a transition joint or asymmetric land joint can be utilized. The land section will then often have multiple land joints along the route, as the maximum installation length on shore is greatly limited by transporting capabilities. In the two ends of the finalized link, terminations are utilized in order to connect the cable to a bus bar, gas insulated switchgear (GIS) or overhead lines. Terminations can contain dielectric fluids or gas, but can also be designed as a dry type. In case of offshore external damages to the cable, an additional length is jointed in and in this particular case a repair joint is utilized.

It is not the purpose of this particular work to in detail describe the complex construction of the cable accessories mentioned above, but to investigate the nature of the interfaces used in some

of the accessories mentioned above. A more detailed description of these accessories can also be found in [5]. In section 2.1.2 a list of interface types found in the various cable accessories is presented in order to highlight to which applications this research is contributing.

2.1.1 Insulation materials

The used insulation material in this thesis is commercial grade XLPE for DC applications. XLPE is a semi-crystalline polymeric material with low conductivity and excellent dielectric breakdown strength [6]. In order to understand the crystalline nature of this material, it is helpful to compare the crystal structures of LDPE, HDPE and XLPE. These three materials are made from the same monomer $(CH_2=CH_2)$, and have the $-(CH_2-CH_2)_n-$ repeat units. What differs them is the way they are produced in the polymerization process, resulting in different configurations of the polymer chains.
LDPE has typically a fair amount of short side chain branches (in the range of three side branches per 100 main-chain carbon atoms [6]) originating from chain backbiting as shown in Figure 3 (A). As the growth initiation point (free radical) on the end of the polymer chain is allowed to relocate itself along the chain in the polymerization process, side branches can be formed to the main chain every time this relocation occurs.
For HDPE on the other hand, the polymerization is initiated on the surface of a Ziegler-Natta catalyst [6]. This allows for the polymerization only to occur on the surface of the catalyst, resulting in the growth of a linear chain, with very few side branches as shown in Figure 3 (B). The amount of side branches present on the polymer chain affects the degree of crystallinity in the material. When cooling from the melt, the polymer chains arrange in a manner to minimize the free energy (often by occupying as little space as possible), resulting in ordered structures as shown in Figure 3 (E). As the growth of lamellae is in the *x-y* plane, the crystal takes a spherical shape, originating from a growth point, and with the lamellae branching on outwards.

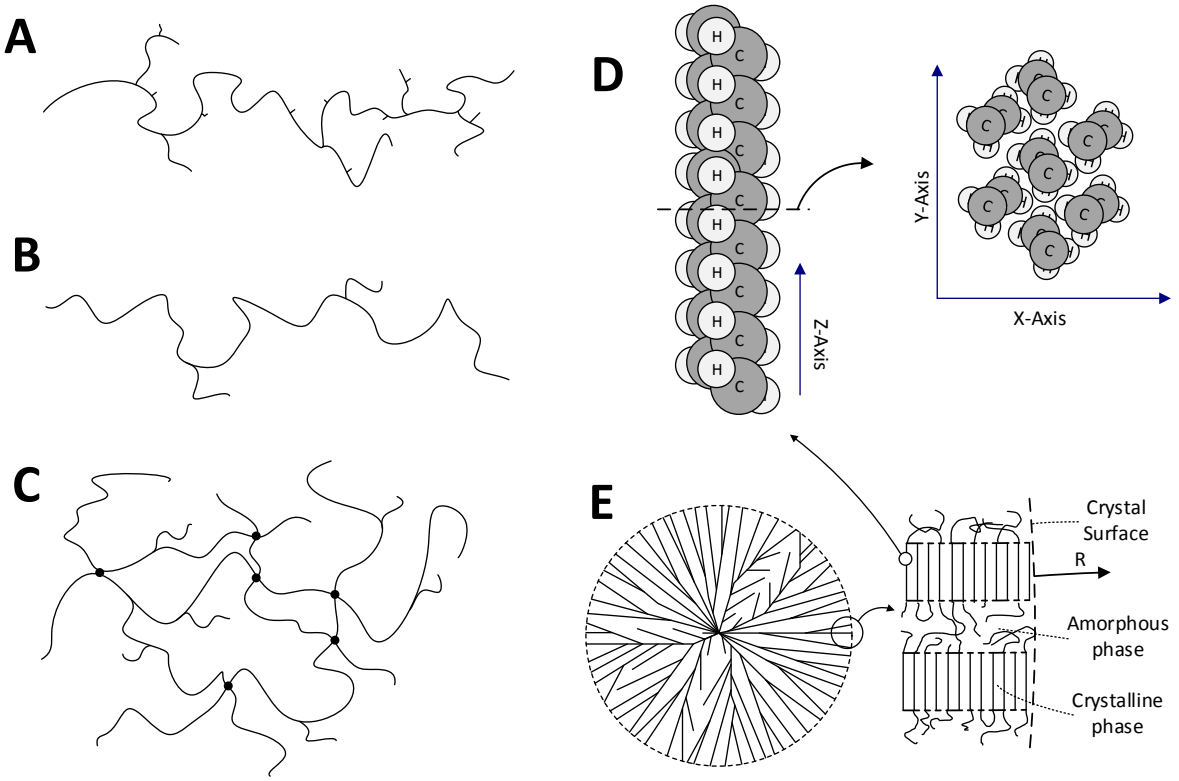

Figure 3.Molecular structure of LDPE (A), HDPE (B), XLPE (C). Conformation of polymer chain and close packing arrangement (D). Shape of spherulite crystal (E) consisting of lamellae with amorphous interstitial areas. Crystal growth radius is indicated with R.

In between the lamellae, amorphous regions are frozen in, resulting in a final spherical shape consisting of many lamellar and amorphous layers as shown in Figure 3 (E). The side branching hinders the formation of these ordered structures to some degree, resulting in different degree of crystallinity for LDPE and HDPE. This crystallization process starts when cooling below the melt temperature T_m, with the crystallization starting at T_c located slightly below T_m, and reduces with temperature until it is fully prohibited below the glass transition temperature T_g.

XLPE is shown in Figure 3 (C) and is created through a crosslinking process. One way of attaining such a crosslinked material is by utilizing LDPE with added dicumyl-peroxide (DCP). In the process the material reacts with heat causing the DCP to decompose and subtract hydrogen atoms from the molecular chains. The left vacancies (referred to as macroradicals) become points where polymer chains are able to bind in a similar fashion as in the polymerization process. The end result is a linked network with improved thermal stability at elevated temperatures, referred to as a thermoset. The drawback of the crosslinking process is that it creates byproducts. These impurities, being α-cumyl alcohol, acetophenone, α-metylstyrene, along with the water and methane, have a negative impact on dielectric performance [7], creating the need of a degassing process.

As shown in Figure 3 (D), the degree of packing can be very dense in the crystalline regions of the material, resulting in low solubility of chemical impurities in these areas. This can result in a higher impurity concentration at the spherulite surface, as these impurities are pushed outwards as the spherulite grows [8], [9], but also a different concentration levels in between the amorphous and crystalline phase within the spherulite itself. Also the conduction processes can differ between the amorphous phase, crystalline phase and crystalline boundary as both the molecular structure and impurity concentration differ in these regions. It should be noted that upon increasing the crosslink density through the use of DCP, the presence of perfect spherulites as shown in Figure 3 (E) is inhibited, causing instead the formation of axialites and les ordered lamellae stacks at higher crosslinking densities [10].

The semiconductive layers in the cable normally consist of non-polar XLPE doped with carbon black (CB) particles. The CB particles predominantly originate from furnace black or acetylene black. The choice of semiconductor materials with regards to CB loading, CB type and choice of base material is known to have an influence on space charge accumulation in the high voltage cable [11], [12].

Pre-molded cable accessories are commonly used for all types of accessories except the factory joint. Such components are usually made through an injection molding process, in order to create the complex shape required. The materials used for such components are rubbers, with ethylene propylene diene monomer (EPDM) and silicon rubber (SiR) being the most commonly used materials. Carbon black loaded materials are also used in pre-molded cable accessories to create the complex geometry required for electric field control. It is important to mention that the injection molding steps used to create these components create different morphological structures as compared to the extrusion process.

2.1.2 Interfaces in high voltage cable systems

In order to more clearly specify different cable interface types, it can be useful to separate them into two categories, chemical interfaces and physical interfaces [13]. The chemical interface is normally inseparable and consists of two materials joined together in an extrusion or injection molding process. Limiting asperities and contamination are the main consideration during

production of such interfaces. Physical interfaces on the other hand are usually created in the field, by mating two materials together without chemical bonding. The physical interface has the same requirements as the chemical interface, however any roughness on the mating surfaces can lead to air pockets. Mechanical pressure ensures contact is withheld during the lifetime of the accessory and is often created through the elastic forces from the pre-molded joint body. Physical interfaces can contain an interstitial medium such as grease or oil for improved mating and slip on of the pre-molded accessory. The most common chemical and physical interfaces present in cable accessories are listed in Table 1.

Table 1. List of interface types present in cable accessories subjected to electrical stress and the materials used in the application.

No	Accessory type	Nature of the interface	Inner material	Outer material
1	Flexible factory joint	Chemical	Joint semicon (molded XLPE with CB)	Joint insulation (molded XLPE)
2		Chemical	Cable semicon (extruded XLPE with CB)	Joint insulation (molded XLPE)
3		Chemical	Cable insulation (extruded XLPE)	Joint insulation (molded XLPE)
4	Land joint, field joint, repair joint and termination	Chemical	Accessory insulation (molded SiR or EPDM)	Accessory semicon (molded SiR or EPDM with CB)
5		Chemical	Cable semicon (extruded XLPE with CB)	Cable insulation (extruded XLPE)
6		**Physical**	Cable insulation (extruded XLPE)	Accessory insulation (molded SiR or EPDM)
7		**Physical**	Cable insulation (extruded XLPE)	Accessory semicon (molded SiR or EPDM with CB)
8	Ordinary termination	**Interface towards gas/liquid**	Cable insulation (extruded XLPE)	Insulating oil, SF_6 gas, or other dielectric fluid/gas
9	Dry-type termination	**Physical**	Accessory insulation (molded SiR or EPDM)	Spacer insulation (molded epoxy)

What most physical interfaces in Table 1 (Number 6 - 8) have in common is that they are created when the outer semicon is removed/stripped from a section of cable, resulting in a cable end as shown in Figure 2. This process can be done in different ways, as referred to in this thesis as cable preparation methods. According to [14] the need for machining and surface preparation of polymers arises when:

- Injection molding and/or extrusion is not suitable to create the sample geometry.
- High dimensional accuracy and surface finish is required, which is higher than can be created with injection molding or extrusion.

The above statements are also somewhat applicable for physical cable interfaces. The prepared cable surface requires a high-quality finish, to be made in the field, preferably avoiding any complex procedures, and should be as repeatable as possible. Also, the geometry of the preparation makes it difficult for any extrusion or injection molding procedures to be applied. For these reasons, abrasion, cutting and remolding procedures are the methods most suitable for the task. These methods create very different surface characteristics, to be investigated further in this thesis.

2.1.3 Cable surface preparation

The nature of the polymer itself may also affect the machinability to some degree. Besides the mechanical parameters such as density, modulus and strength also molecular structure can affect the surface preparation. For example, the presence of crosslinks in the material restricts the material from ductile behavior (melt flow) during any kind of machining, when locally the melt temperature is exceeded [15]. This can lead to different end results using the same preparation method on a thermoset or a thermoplastic material. Also, the glass transition temperature of the material can affect the outcome of preparation, which is around -120°C for LDPE. Any preparations carried out below this temperature (note: local temperature at tool edge) remove material through a rupture or extreme fracture process, while above this temperature, a yielding process is possible to occur [16]. The yielding of a polymer can be described through the flow model of Eyring [6]. The yielding process in this model is dependent on the temperature and log linearly on the strain rate (cutting speed) during the preparation. These parameters are thus crucial to control in the used preparation methods in order to create reproducibility in the field.

In abrasion, material removal is carried out through sharp Al_2O_3, SiC or diamond grains embedded on a substrate, which are rubbed along the polymer surface. It is common to start with a lower grit size and work down until finalizing with the highest grit size. Coolant can be used both for cooling and for more effectively removing polymeric particles from the abrasive. When the polymeric particles are pulled off from the polymer, certain peaks can be seen on the polymer surface [17]. These peaks could be evidence of the yielding process as described by Eyring's flow model. The final surface texture should resemble a matte scratched surface originating from the latest used grit size, as shown in Figure 4.

When cutting a polymeric surface, a cutting blade moves along the surface cutting of slices from the material. This process shares similarities with ordinary machining, except that the rake angle of the tool is much lower. The rake angle is known to affect the fracture mode during preparation [15], although any fracturing should not be the major form of material removal for XLPE, as the glass transition temperature is likely exceeded at the tip of the cutting blade. The final surface texture should be a striated surface originating from the cutting edge, as shown in Figure 4.

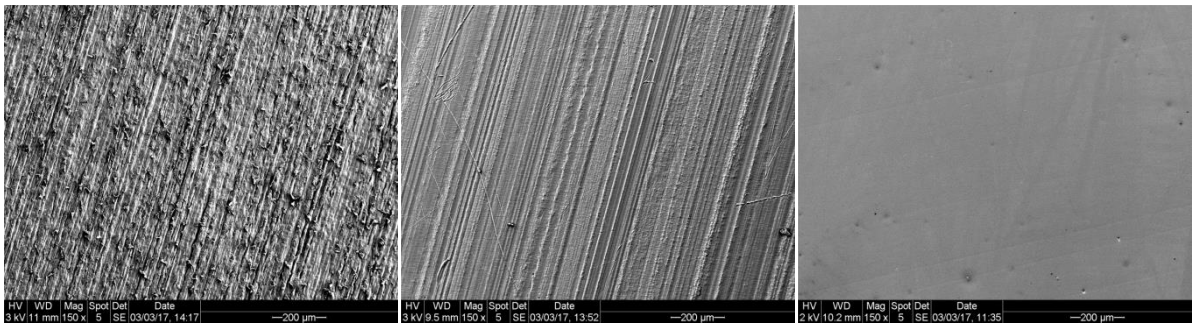

Figure 4. Texture of abraded (left), cut (centre) and remolded (right) XLPE cable surfaces.

When remolding a polymeric surface, a process similar to molding is used. The major difference is in this case that the material to be remolded has already been formed and crosslinked. If the crosslink density is sufficiently low, the two methods should result in very similar results. The remolding procedure could affect the morphology near the surface, depending on temperature and the film material used in the process [18]. The final surface texture should be a replica of the surface texture of the contacting film used during the remolding process, which is shown in

Figure 4. In this way, an extruded or molded surface texture can be introduced in the field in a very effective way.

2.1.4 Surface parameters

What characterizes the polymer surface is the roughness, texture, and the way it differs from the bulk of the material. On the polymer surface, different atomic bonds can be present than found in the bulk of the material. These bonds originate from foreign atoms introduced in the preparation stage. For example, radicals (sometimes referred to as loose or dangling bonds) created through chain cutting, can bind with atmospheric oxygen, resulting in double bonded oxygen to the main chain referred to as carbonyl groups *(C=0)*, but also alkynes *(C=C)* and other imperfect crystalline structures can be created. This is a process similar to oxidation of the base material, where the dangling bonds (free radicals) are instead introduced through chain scission initiated by a degradation process. Any foreign atoms or molecules present on the surface are referred to as surface states, as electron interaction will differ at these sites. Also foreign particles and impurities can be found on the polymer surface as a result from the preparation process, these are normally avoided as much as possible trough strict cleanliness requirements. The local density of small molecular weight chemical impurities can also be altered through the preparation process by local introduction or outgassing of chemical species. The morphology in the surface region can also be affected through the preparation method [18] as mentioned before.

When investigating the impact of surface roughness, it is very important to know which phenomena can come into play. For rough surfaces, the presence of partial discharges (PD) in the void areas created upon mating the surface are often the main initiator of the breakdown process [17], [19], [20] in joints and terminations. Partial discharge inception has been shown to be greatly dependent on void size. Due to the different material parameters in the void and in the bulk of the material, the AC inception field in the surrounding material for a normal gaseous spherical void can be as low as 19 kV/mm for a 7 µm void while for a 2 µm void an inception field strength of 150 kV/mm can be estimated [21]. For sake of clarifying which roughness range is of interest, such a scale is presented below in Figure 5.

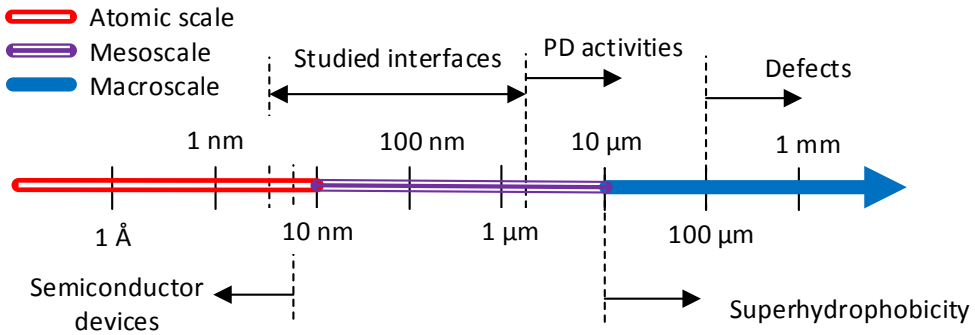

Figure 5. Logarithmic scale of surface roughness for the studied surfaces and other applications

Figure 5 introduces 3 different roughness ranges; the atomic scale, the mesoscale and the macroscale [22]. Interface roughness found in semiconductor devices such as MOSFET:s and CMUT:s [23] is most often in the nanoscale range. The impact of roughness is less studied for semiconductor devices as the roughness level is low and polishing methods are capable of creating nearly atomically smooth surfaces due to the hardness of the base material. What is lacking in literature is the impact of mesoscopic roughness levels on electrical properties in applications such as the physical HVDC accessory interfaces. The XLPE surfaces for study are

thus not ideal with regards to roughness, but free from defects and PDs when mated with a pre-molded accessory. It can also be mentioned that the scale presented in Figure 5 is also relevant for understanding at which scale certain conduction phenomena have been derived and are applicable.

2.1.5 Surface free energy

The wettability of surfaces is determined by the surface free energy (SFE). The SFE is affected by surface states and roughness of the surface, and can thus be a useful tool for assessing these surface properties. The species and bonds present on the surface interact with the liquid, pulling any droplet down onto the surface by overcoming the surface tension of the liquid. Complete wettability is thus achieved when the SFE of the surface exceeds that of the liquid, and the liquids spreads across the surface as a film.

The SFE can be estimated through contact angle experiments. Multiple methods for calculation of SFE are available, and for polymeric materials the Nuemann method (1) and determination through contact angle hysteresis (2) are most commonly used.

$$\left(\gamma_s/\gamma_l\right)^2(1-\beta_2(\gamma_l-\gamma_s)^2) = 0.5(1+\cos\theta_a) \tag{1}$$

Where θ_a is the advancing contact angle, γ_s is the SFE, γ_l is the liquids surface tension and β_2 is a predetermined parameter. Determination through contact angle hysteresis can be done according to:

$$\gamma_s = \gamma_l(\cos\theta_r - \cos\theta_a)\frac{(1+\cos\theta_a)^2}{(1+\cos\theta_r)^2-(1+\cos\theta_a)^2} \tag{2}$$

Where θ_r is the receding contact angle. Increased surface roughness is also known to improve the wettability, according to the Wenzel state, until the roughness is so high that air is present underneath the droplet, at which the wettability is reduced (as for superhydrophobic surfaces) according to the Cassie-Baxters state:

$$\cos\theta_m = rf\cos\theta_Y + (f-1) \tag{3}$$

Where θ_m is the measured advancing contact angle, θ_Y is the Young (ideal, advancing) contact angle of an infinitely smooth surface, r is the roughness ratio and f is the fraction of the droplet in contact with the surface. Setting the fraction f to one, simplifies Cassie-Baxters equation into The Wenzel equation where only the roughness ratio affects the difference between the measured and young's contact angle.

It is stated explicitly by [24] that equation (2) cannot used for SFE determination of rough, heterogenous surfaces. The local energy minima and maxima for such surfaces interact with the advancing and receding too much such that equation (1) together with (3) is the only viable option given that the surface is rough and homogeneous, and that the droplet size exceeds the roughness of the surface to some extent.

SFE can be used as a measure of the work function [25][26], and as it is also sensitive to roughness and surface states, it can thus be a helpful parameter for determining such electrical properties together with a measurement of the surface roughness.

2.2 Macroscopic models

In this section, the general field equations for electrostatics are introduced, along with the Maxwell-Wagner-Sillars (MWS) model. Macroscopic expressions for space charge and electric field are in general in good agreement with experimental results up to the threshold of significant space charge injection [27][12]. Above this threshold, which lies in the region of 5-30 kV/mm, non-linear mechanisms (non-linear conduction and injection) come into play, and purely ohmic relations are no longer valid. The reason for the wide spread in the range of this threshold is because the mechanisms are greatly dependent on many factors, such as the nature of the interface, temperature [28], material types and many other parameters.

2.2.1 Electric field equations

In order to describe the electric field within dielectrics and the impact on charge phenomena, it can be useful to start with fundamental expressions derived from Maxwell equations. By defining electrostatic potential with the aid of Maxwell-Faradays equation over an unclosed loop, it is possible to combine it with Gauss law to derive Poisson's equation:

$$\nabla^2 V = -\frac{\rho}{\varepsilon} \tag{4}$$

Where V is the electrostatic potential in Volts, ρ is the charge density in C/m^3 and ε is the relative permittivity of the dielectric in As/Vm. Poisson's equation allows for a very straightforward calculation of the voltage distribution in the absence of charge in the material $(\rho=0)$, which is usually the case for AC applications. This simplification of equation (4) is often referred to as Laplace's equation. For DC cable systems on the other hand this simplification is seldom applicable as a gradient in ε/σ often exists, resulting in space charge accumulation in the system, as shown in relation (5):

$$\nabla\left(\frac{\varepsilon}{\sigma}\right) \neq 0 \;\rightarrow\; \rho \neq 0 \tag{5}$$

Where σ is the conductivity of the material in S/m. Whenever a gradient ε/σ is present, Poisson's equation (4) cannot be simplified to Laplace's equation. What is useful with this relation is that the space charge can be estimated if the gradient ε/σ is known, given that these two material parameters and their spatial dependencies are defined [28]. Also for interfaces between two materials with different ε/σ ratios, estimation of surface charge ρ_s becomes possible. The gradient in ε/σ is often caused by the non-uniform conductivity distribution in DC XLPE materials and can be presented by equation (6), assuming an Arrhenius dependency on temperature and a similar exponential dependency on electric field.

$$\sigma(E,T) = \sigma_0 e^{\alpha T} e^{\beta E} \tag{6}$$

Here σ_0 is the zero level conductivity in S/m, α is the temperature parameter in 1/C° and β is a field parameter in mm/kV. Relation (6) can also be extended to include a known concentration of PDP, given that their impact on conductivity is known. When the temperature, electric field or impurity concentration is non-uniformly distributed in the system, the steady state electric field will differentiate from the Laplacian field and space charge will accumulate in the system. By knowing the parameters in expression (6), the steady state electric field can now be known in cable systems at zero load (cold conditions), under maximum rated load (with a temperature

gradient in the insulation) and at various levels of applied stress. The next section will focus on what will happen when the system is in a transient stage.

2.2.2 Maxwell-Wagner-Sillars interfacial polarization

Maxwell-Wagner-Sillars (MWS) polarization arises from differences in permittivity and/or conductivity on two sides of an interface. An expression can be derived for a stepwise voltage application (application of V_0 at $t=0$) in parallel-plane geometry that defines the quantity of charge accumulated in the interface:

$$\rho_s(t) = \frac{\varepsilon_a\sigma_b - \varepsilon_b\sigma_a}{b\sigma_a + a\sigma_b} V_0(1 - e^{-t/\tau}) \tag{7}$$

This equation features a time constant τ, which is expressed in equation (8) below, where ε_a and ε_b are the permittivities, σ_a and σ_b are the conductivities, and a and b are the thicknesses of the contacting materials a and b respectively, influencing the magnitude and polarity of the interfacial charge.

$$\tau = \frac{b\varepsilon_a + a\varepsilon_b}{b\sigma_a + a\sigma_b} \tag{8}$$

The time constant defines how fast the interfacial charge accumulates. It also refers to the variation of the electric field exemplified in equation (9) for the field in material a (E_a):

$$E_a(t) = V_0 \frac{\sigma_b}{b\sigma_a + a\sigma_b}\left(1 - e^{-t/\tau}\right) + V_0 \frac{\varepsilon_b}{b\varepsilon_a + a\varepsilon_b} e^{-t/\tau} \tag{9}$$

As equation (9) can be separated into capacitive and resistive parts, this allows for making the following statements that obey the interfacial polarization:

- Directly at voltage application *(t=0)* the field distribution is purely capacitive.
- When *t* approaches infinity a purely resistive field distribution will be present.
- The time constant governs the speed of transition between the types of field.

Variations of the time constant τ are often caused by changes in conductivity, which is field and temperature dependent as described in equation (6). The MWS equations are very helpful for explaining various phenomena for DC systems, and differences between different insulations types. It is normally the case that the very low conductivity of DC grade XLPE makes testing these materials very time consuming, and creates a fairly slow polarization process upon voltage application. Applying the voltage to a heated system instead speeds up the polarization process, as the overall conductivity is increased through equation (6).

What can also be done when deriving the MWS expression is to instead of assuming a stepwise voltage application, inserting a ramped DC voltage instead, as many DC breakdown tests often utilize a ramped voltage application. This only introduces a small difference in the calculation, as the expressions after Laplace transformation are quite similar:

$$\begin{cases} V_{step}(s) = \mathcal{L}\{V_0\theta(t)\} = \dfrac{V_0}{s} \\ V_{ramp}(s) = \mathcal{L}\{V_r * t\} = \dfrac{V_r}{s^2} \end{cases} \tag{10}$$

Where $\theta(t)$ is a step function, V_0 is the magnitude of the applied step and V_r is the ramp rate in *V/s*. After the derivation, expression (11) is obtained. What is useful is that this expression utilizes the same parameters and time constant as for stepwise voltage application.

$$E_a(t) = \tau\left(V_r\frac{\varepsilon_b}{b\varepsilon_a + a\varepsilon_b}\left(1 - e^{-t/\tau}\right) + V_r\frac{\sigma_b}{(b\sigma_a + a\sigma_b)}\left(\frac{t}{\tau} + e^{-t/\tau} - 1\right)\right) \quad (11)$$

This expression is slightly more problematic to evaluate, as the end result cannot be fully divided into a resistive and a conductive part with full separation of the capacitive and resistive material parameters. However, the following statements for interface polarization for ramped DC voltage apply:

- The percentage of the DC content can be calculated by dividing the resistive part of equation (11) by the full expression. When this is done, V_r cancels out, meaning that the shift towards a DC distribution is independent on the applied ramping speed (when neglecting the impact of the field dependency in the conductivity).
- The shift from an AC to a DC field distribution is still governed by the same time constant τ. As the expression has changed, the time to reach the same percentage of DC content can be affected to some degree compared to stepwise voltage application.
- For a ramped DC breakdown test, it is thus crucial to set the ramping speed so that the breakdown level is reached after the shift to a DC distribution is realized in order ensure that the impact of interfacial charge accumulation is present in the end result.

2.2.3 Extended Maxwell-Wagner-Sillars model

The MWS model can also be extended to include the impact of interfaces with finite smoothness and interstitial materials [13][29][30]. In this case, the real interface is modeled as a fictitious material with ideal interfaces towards its surroundings, as shown in Figure 6.

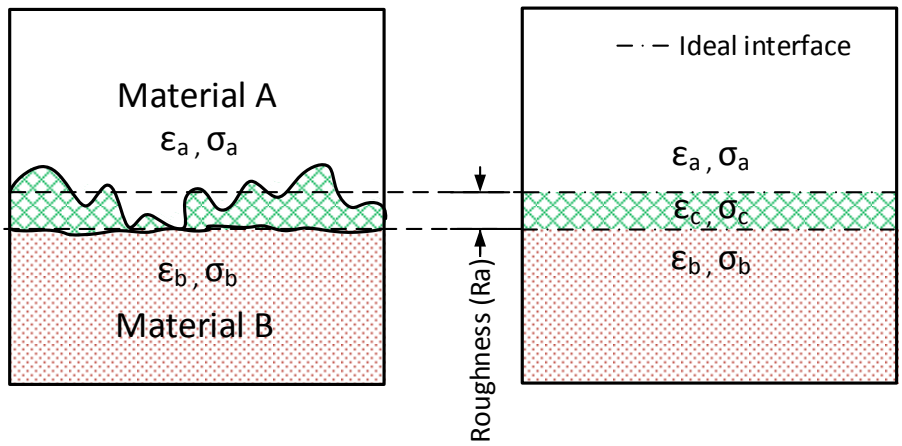

Figure 6. Simplification of a real measured interface with interstitial material into a fictitious dielectric layer according to Bodega et al [30].

The extension of the MWS model to include the interface as a separate material, allows for macroscopic field estimation given that the interface parameters are known. A viable option seems to use a measured roughness parameter (which can vary over many decades for the tested surface types) to determine the thickness of the fictitious layer, while using the interface nature (dry, oil, wet etc.) to assign the permittivity ε and conductivity σ of the interstitial layer.

Depending on the type of the interface, a different amount of materials needs to be included in the MWS model, and is shown in Table 2 below.

Table 2. Amount of materials to be used in extended MWS model depending on interface type.

Interface type	Physical interface	Chemical interface
Insulator - Electrode	2 materials	1 material
Insulator - Insulator	3 materials	2 materials

As can be seen in Table 2 this model struggles in describing different electric properties for chemical interfaces, as there are no material parameters available for the interstitial layer. This is because the introduction of surface states, work functions and field dependent effects ought to be taken into account in this fictitious layer, as these properties likely could have an impact on electric field distribution.

Montanari and Morshuis [29] agree on the limitations of the extended MWS model when it comes to microscopic charge behavior. The extended MWS model can thus sometimes be helpful tool for understanding some of the effects observed in interfaces, but fails to consider the complex nature of the charge carriers. This could cause the extended MWS model to be an approach working well for electric field levels below the threshold for significant charge injection.

The extended MWS model was also used by Zhang et. al [23] in order to explain the influence of surface roughness on surface charge trapping in their device featuring a physical interface and a chemical interface both in contact with an electrode. They claim that minimizing insulator roughness in their physical interface is important to reduce surface charge trapping, while minimizing electrode roughness (in their chemical interface) is important to reduce trans-dielectric currents and charging rate.

2.3 Microscopic models

In this section, a microscopic approach to conduction and interface physics is presented. The basis of the band gap model originates from semiconductor physics and is described in detail in the works of Kittel [31], Neamen [32] and Dissado [33].

2.3.1 Origin of the band gap model

The band gap model can be derived by using the time-independent Schrödinger Equation (SE), on an electron confined in a periodic potential of the material lattice. Such an expression is shown in equation (12) for a one dimensional system.

$$\frac{\partial^2\psi(x)}{\partial x^2}+\frac{2m}{\hbar^2}\big(E-V(x)\big)\psi(x)=0 \tag{12}$$

Where *m* is the mass of the electron, *ħ* is the modified Planck's constant, *E* is the thermodynamic energy in eV and *V(x)* is the periodic coulomb potential of the lattice in Volts. It is very important to note that it is the interactions of mobile electrons with the fixed, periodic lattice potential *V(x)* that gives rise to the forbidden energy bands (band gaps). In order to better understand the wide range of conductive properties, E-k diagrams of different material types are shown in Figure 7. The derived E-k relation can be simplified to the reduced zone scheme as shown in Figure 7 (A).

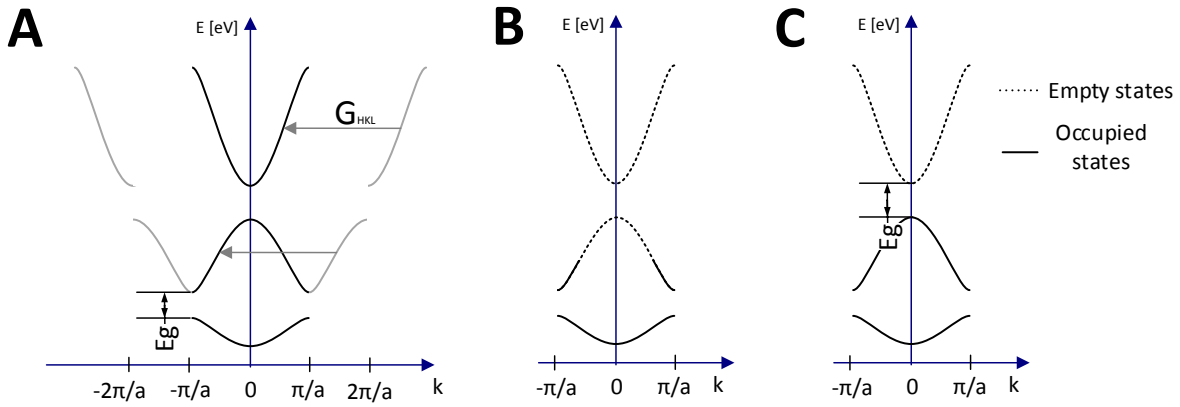

Figure 7. Reduction to reduced zone representation by addition of reciprocal lattice vector (A). E-k diagram for a metal (B). E-k diagram for a semiconductor or insulator with indicated (direct) bangap Eg (C).

For metals (Figure 7 B), empty states are available just at the Fermi level, thus little additional energy is required for allowing an electron to conduct. For semiconductors and insulators on the other hand, a band is filled and energy greater than the band gap *(Eg)* is required in order to excite an electron-hole pair. The empty band is referred to as the conduction band and the occupied band is referred to as the valence band. Holes in this case are the absence of electrons in the valence band. The Fermi level will be positioned somewhere between the conduction and valence band. The Fermi-Dirac distribution function (13), determines whether a certain state is occupied or empty given a certain temperature.

$$f(E)=\frac{1}{1+e^{(E-E_f)/kT}} \tag{13}$$

Where E is the thermodynamic energy in eV, E_f is the chemical potential, k is Boltzmann's constant and T is the temperature in K. The occupation probability for holes is the opposite of electrons. The Fermi Dirac distribution function at $T > 0\ K$ will give a probability spread around the Fermi level. The exact position of the Fermi level is dependent on impurity concentrations and the relative mass of electrons and holes respectively. The total electron concentration in the material is now given by:

$$n_0 = \int g(E)f(E)dE \tag{14}$$

Where *f(E)* is the Fermi-Dirac distribution expressed in equation (13), and *g(E)* is the density of states (DOS) which is derived in a similar fashion as E-k diagrams from Figure 7, but for a three dimensional system. The hole concentration can be derived with a similar equation as (14). For semiconductors at ambient temperature, the above relations and the fairly low magnitude of the band gap results in that a fair amount of electron-hole pairs is constantly being generated in the conduction and valence bands. These carriers will contribute to conduction in these materials in the same way as in metals according to the Drude model. For insulators, the magnitude of the band gap is far greater and thus the creation probability for charge carriers by phonon excitation is far lower. The probability density of these charge carriers (hot electrons) is so low that modeling conduction phenomena within the band gap becomes of importance.

2.3.2 The band gap of polyethylene

Similar to semiconductors, the polymeric chains also consist of covalent bonds, and the intra-chain conduction assuming a fully aligned chain is therefore also created through a periodic potential *V(x)* in the wave function expressed by equation (12), resulting in the band gap as shown in Figure 8 A, which is plotted against position *x*.

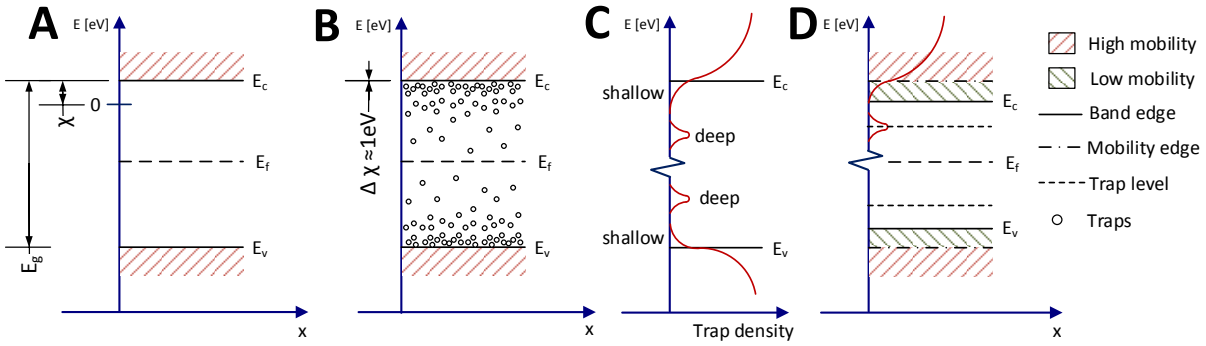

Figure 8. Schematic representation of the band gap of polyethylene. Ideal band gap (A), realistic band gap with traps and variation in the position of the band edges (B), Density of states (DOS) assuming Gaussian distribution at a single level of deep traps (C) adopted from [34]*, and mobility edge simplification with single trap level (D).*

Where χ is the electron affinity for polyethylene and is in the range of -0.65 eV to -1 eV for the crystalline phase of the material, and the band gap E_g is known to be around 6-8 eV. The ideal band gap of a polymer predicts unrealistically high electron mobility properties of the insulator. It is thus necessary, to extend the model to account for any kind of imperfection present in the material, such as the non-ideal conformations of the polymer chains, but also defects, double-bonds, vacancies (free volume) and impurities. These imperfections interrupt the periodic

potential in the wave function (12), and thus alter the band gap by creating states within the band gap as shown in Figure 8 B.

For polymers the conformation of the chain can vary, and can be highly entangled in the amorphous regions or more ordered such as in crystalline regions of the polymer, as was shown in Figure 3. The non-ideal conformation of the polymer chains affects the position of the conduction band E_c, and also introduces states close to the band edge, referred to as shallow traps [34]. In the amorphous phase the conduction band can be around 1 eV lower than in the crystalline regions of the polymer, which has a significant impact on the local conduction processes. An amorphous/crystalline barrier can prevent significant charge transport in the crystalline phase of the material. The cross-links introduced in XLPE have been determined to affect the state density very little [35], giving LDPE and XLPE similar characteristics given that the morphology is the same and PDP content is very low.

As impurities and imperfections create allowed states within the band gap, the DOS of the ideal bad gap from Figure 7 C needs to be revised in order to account for such states as shown in Figure 8 C. As the exact DOS is difficult to estimate, the trap distribution is often simplified to either a single level, an exponential or a Gaussian distribution, and this determines the conduction properties to great extent. Depending on the energy level (depth) of the trap, the energy required for detrapping differs, which impacts the carrier mobility. The introduction of shallow traps near the band edges lowers the effective mobility of the charge carrier and thus creates a realistic transport model. Accounting for shallow traps can be done by defining a mobility edge, as is done in Figure 8 D, where the area close to band edges can be assigned a separate mobility. The deep traps further away from the band edges have a lower concentration and reduce the mobility even further. However, the low concentration results in high enough separation distance between adjacent deep trap sites that conduction (hopping) in between deep traps is very unlikely. The mobility gap approach with a single deep trap level is often used [36]–[38], as shown in Figure 8 D, and is favorable to describe bulk conduction in polymers. Further impact of traps on bulk conduction processes is investigated in section 2.3.6.

2.3.3 The Schottky barrier

The behavior of contacts between metal-semiconductor and metal-insulation and the behavior with respect to thermionic emission is best described with the Schottky barrier. It is necessary to know that the ideal Schottky barrier assumes infinitely low surface roughness and the absence of any surface states. When contacting a metal to a semiconductor, Fermi levels will align in equilibrium and a barrier is formed. The alignment of Fermi levels in equilibrium only occurs for semiconductors (n or p type) as for doped semiconductors an excess carrier concentration (positive or negative) exists, and contacting with the metal will cause majority charge carriers to flow from the semiconductor into the metal, until Fermi levels are aligned. This flow leaves behind opposite charge, creating a depletion region in the semiconductor resulting in band bending. For insulators on the other hand, no significant majority charge concentration exist, thus contacting does not result in any significant band bending and alignment of Fermi levels. The barrier height for electrons is determined by the difference between the metal work function ϕ_m and the electron affinity of the insulator χ as shown in Figure 9 and equation (15).

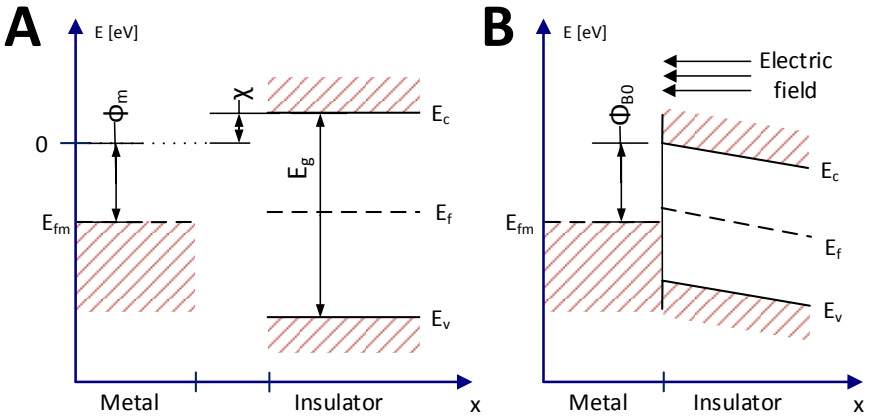

Figure 9. Schottky barrier before contact (A), and after contact with electric field in the insulator (B).

The further derivation of the Schottky barrier is based on the ideal barrier height as shown in Figure 9 A. The barrier height for charge injection will be:

$$\phi_{B0} = (\phi_m - \chi) \tag{15}$$

The electron affinity χ typically lies within 3-5 eV for ordinary semiconductors, while for crystalline polyethylene it is around -1 eV. Note that if the electron affinity is negative, it will add to the total barrier height. Typical metal work functions ϕ_m vary between 4 and 6 eV. What is shared between semiconductors and insulators is the field lowering effect of the Schottky barrier. An electron at a distance *x* from the metal will create an electric field towards the barrier, best described with an image charge at the other side of the barrier (at -*x*) as shown in Figure 10 B. This creates a force due to coulomb attraction, on the electron as described by equation (16).

$$F(x) = \frac{-e^2}{4\pi\varepsilon_o\varepsilon_r(2x)^2} = -eE \tag{16}$$

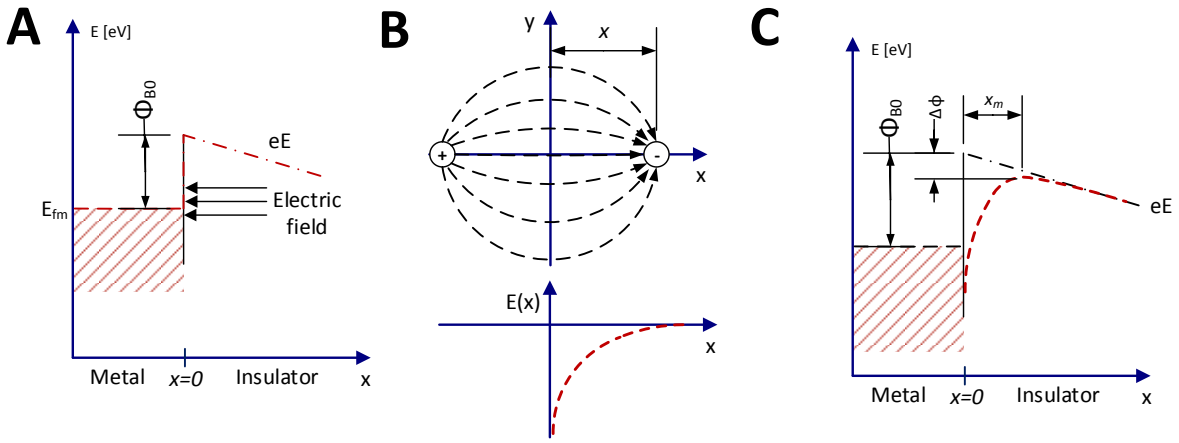

Figure 10. Field lowering effect of Schottky barrier. Barrier without field lowering effect (A), image charge effect on electric field (B) and barrier with field lowering effect as a superposition of the electric field in (A) and (B).

The modification of the potential, can be found by integrating the electric field from expression (16) over ∂x resulting in expression (17), the peak potential barrier is now lowered as shown in Figure 10 C, and this lowering is referred to as the Schottky effect.

$$-\phi(x) = \frac{-e}{16\pi\varepsilon_o\varepsilon_r x} - Ex \tag{17}$$

At the onset of electric field, the maximum barrier height can now be found by setting the derivative of the potential to zero, as this is the position of maximum potential. This derivation leads to the position of the maximal barrier (18):

$$x_m = \sqrt{\frac{e}{16\pi\varepsilon_o\varepsilon_r E}} \tag{18}$$

By combining expression (18) with the definition of electrostatic potential the following expression can be derived:

$$\Delta\phi = \sqrt{\frac{eE}{4\pi\varepsilon_o\varepsilon_r}} \tag{19}$$

For the reduction of the potential barrier $\Delta\phi$, in eV, in expression (19) to be valid, a barrier towards metal or a material of sufficient high permittivity to create a symmetric image charge effect is needed. It is thus not valid for insulator-insulator interfaces. The I-V relationship for Schottky barrier can be derived with thermionic emission theory. The derivation changes slightly for an insulator compared to a doped semiconductor, as band bending is absent for an insulator in equilibrium. The current density from the metal into the insulator is a function of the concentration of electrons, flowing in the x direction with sufficient velocity to overcome the barrier without reflection. Integration is to be done from the minimum speed v_x' required for emission into the insulator and also over the other 2 dimensions as these terms contribute towards the total electron energy. Also a reflection term R is included into the equation in order to account for the probability of backscattering at the barrier. This yields the current expression for Schottky injection as:

$$J = (1-R)A^*T^2 e^{-(\phi_{BO} - e\Delta\phi)/k_BT} \tag{20}$$

Where k_B is Boltzmann's constant, ϕ_{B0} is the barrier height in Volts and A^* is the Richardson's constant and for the insulator-metal junction is given by:

$$A^* = \frac{4\pi e m_e^* {k_B}^2}{h^3} \tag{21}$$

Expression (20) resembles very much the reverse-saturation current density for metal-semiconductor interfaces. By inserting equation (19) into (20) it becomes possible to determine the current density along the metal-insulator interface as:

$$J = (1-R)A^*T^2 e^{\frac{e}{k_BT}\left(\frac{-\phi_{B0}}{e} + \sqrt{\frac{eE}{4\pi\varepsilon_o\varepsilon_r}}\right)} \tag{22}$$

It can be noticed that there is a quadratic dependence on temperature, and that *log(J)* should vary linearly against $\sqrt{E}$. It should also be noted that the high frequency component of the permittivity must be used since the time to cross the barrier is very low. The image charge effect, as shown in Figure 10, reduces the barrier close to an electrode of higher permittivity, as the image charge effect is determined by the permittivity difference across the barrier [39], [40]. A barrier towards an electrode of similar or lower permittivity would thus not have the same field dependency as derived here. Also surface fluorination and other methods could also affect the surface permittivity [41] which in turn also could affect the image charge effect. The calculation of the image charge effect uses Laplacian field in only one dimension, meaning that the impact of space charge effects in the injection process is neglected. Taylor and Lewis [42] suggested instead an activation process to take account for space charge effects, which resulted in a different field dependency in the final equation. The Richardson's constant A^* is many orders of magnitude less for real experiments, which could be due to non-ideal metal surfaces in the barrier according to Lewis et al [43]. The impact of non-ideal surface factors is further investigated in sections 2.3.3.1 and 2.3.3.2.

The Schottky equation, derived for electron injection, is normally assumed to be valid for hole injection as well. For injected holes, the image charge effect works in the same way, giving a very similar field dependency to the equation. However, some of the barrier heights might differ as the metal work function is seldom placed symmetrically in between the conduction and valence band, as shown in Figure 9.

2.3.3.1 The impact of surface roughness

As the field dependency in Schottky equation originates from the field lowering barrier effect, the impact of electrode roughness on injected current is through enhanced electric field at the created asperities, locally increasing the electric field and reducing the barrier further as shown in Figure 11. As the field dependency in Schottky injection is non-linear, the areas with increased field (A) will see a higher degree of increased current density, then the reduced current density at the areas (B) with reduced electric field. This effect can be modeled for a small surface area section and by introducing field enhancement factors (FEF) for every point in this section, the local Schottky current densities to be found. The average injected Schottky current density can then be found by averaging the local current densities from every point in the area section, as shown in equation (23).

$$J_{avg}(E) = \frac{1}{y_{max} x_{max}} \int_0^{y_{max}} \int_0^{x_{max}} J(FEF(x,y) * E) dx dy \tag{23}$$

Where x_{max} and y_{max} are the dimensions of investigated domain respectively. The presence of localized field enhancing factors have been investigated [43] in the past by introduction of a β-parameter scaling the electric field in the exponent of equation (22), but calculation taking into account the exact mesoscopic geometry is to some degree new as finite element method (FEM) software and today's computing power is a necessary tool for such calculations. Such an approach was realized by Taleb et al [44] for a line segment, and by recreating the surface geometry from measured surface parameters. This resulted in a higher injected current density for a rough interface compared to a smooth interface.

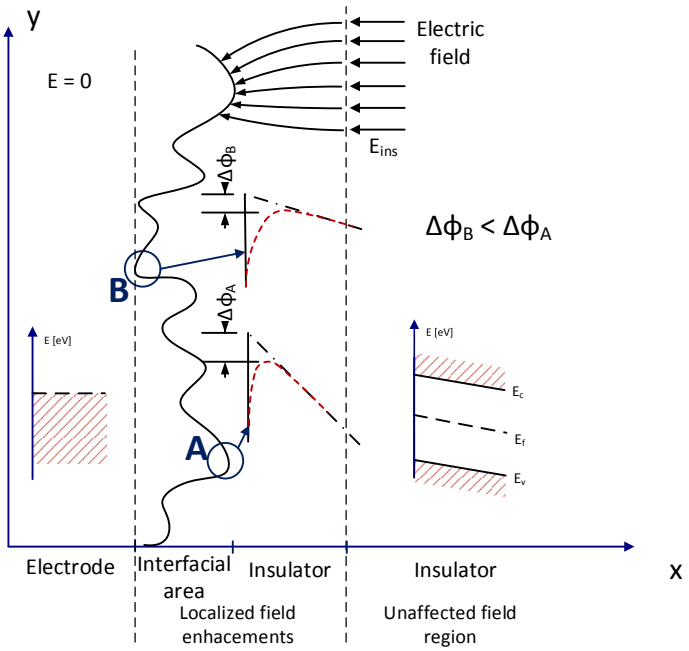

Figure 11. Local impact of surface roughness on the field barrier lowering effect

The range of the surface roughness and applied electric fields for roughness assisted injection to be theoretically viable is important. The lower range of roughness and electric field is practically not present, only that the impact is not observable. The upper range for roughness however, should be limited as discussed previously to be below the inception voltage for partial discharges in any created voids. Also for major electrode deviations/protrusions averaging the injected current is not applicable, making such an approach a purely mesoscopic phenomenon limited to around a few μm in roughness.

For higher levels of electric field, the highest electric field found at the asperities could reduce the barrier width that much that other injection phenomena start dominating. For example Koeningsfeld et al [45] found that surface roughness had a significant impact on Fowler-Nordheim injection from a polycrystalline diamond surface. This could result in a transition field range where the dominating current from the peaks (area A in Figure 11) is from Fowler-Nordheim injection, while at the other areas Schottky injection is dominating. The impact of roughness on charge injection affects both injection types.

2.3.3.2 The impact of surface states

Figure 12 shows a possible impact of surface states. Such surface states can originate from [46]:

1. Intrinsic surface states created by the discontinuity of the lattice potential *V(x)* as used in SE (12). These are created by broken or terminated (“dangling”) bonds when the surface is created.
2. Metal-induced states due to the metal wave function extending into the insulator.
3. Extrinsic surface states occurring in the bulk of the material which will also occur on the surface.
4. Extrinsic states specific to the surface due to the preparation method used, such as oxidation etc.

The trap density distribution towards the surface could be of importance, and is shown with a very narrow spread in Figure 12 A.

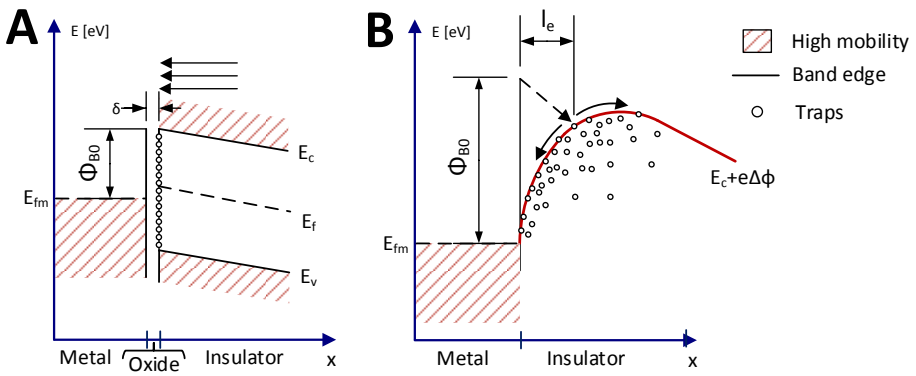

Figure 12. Schottky barrier with surface states and oxide/dipole layer of thickness δ (A) and impact of lattice collision and thermalization before reaching the potential maximum (B).

For some semiconductor materials, an oxide or dipole layer of a few Ångström is usually considered to separate the surface states (originating from intrinsic or metal induced states) from the electrode, as shown in Figure 12 A. This separation causes the Fermi level to become "pinned" at the surface and eliminates the impact of the metal work function for semiconductors [46]. This pinning effect has also been modeled by Chen et. al. [47] for metal – polyethylene interfaces, claiming that the interface dipole layer is responsible for the weak influence of metal work function on injected current density into polymers. Baldo and Forrest [48] also theorize upon the interface dipole effect, and conclude that this effect is able to lower the injection barrier as much as by 1 eV, and make the injection process dependent on local energetic disorder (morphology). Their approach is that charge injection occurs as a hopping process out of interfacial molecular sites, making it similar to the approaches described in section 2.3.4.1.

Apart from the interface dipole, also other deviations from Schottky law have been theorized, such as scattering events in the injection process [49], [50]. These events are likely when the electron mean free path l_e (which can be in the range of 1 nm in organic solids [49]) is shorter than the distance to the maximum of the barrier height x_m as defined in equation (18). In such a case, a scattering is likely to occur, causing the electron to lose its speed and energy (referred to as thermalization), as shown with the dashed arrow in Figure 12 B. The thermalized electron then has to overcome the image charge potential, and has a certain probability for forward diffusion and backwards diffusion. The impact of diffusion within the injection process will depend on electron mobility [51]. When traps are introduced, the injection process becomes a hopping process in the image charge potential [52], which will be further addressed in section 2.3.4.1.

2.3.4 Fowler-Nordheim injection

Two types of tunneling are known: (ordinary) tunneling and Fowler-Nordheim injection (or cold field emission). Ordinary tunneling occurs through the entire material or layer in question, and is normally only considered for extremely thin atomic devices. Tunneling occurs because of the non-infinite height of the encountered potential barrier, resulting in an exponential decay of the wave equation. This gives a small probability for electrons, behaving both as a particle and a wave due the particle-wave duality principle, to enter the insulating material. For sufficiently thin barriers, there is a small probability for the electron to travel into and through the barrier. For Fowler-Nordheim injection, the electron tunnels from the electrode into the conduction band of the insulator [53], [54]. This effect becomes significant if the electric field is high enough and thus the barrier sufficiently thin. Fowler-Nordheim injection, as illustrated

in Figure 13, occurs when electrons around and below Fermi level in the metal are directly injected into the solid without being thermally activated, making this a cold type of field emission, able to inject carriers also at extremely low temperatures.

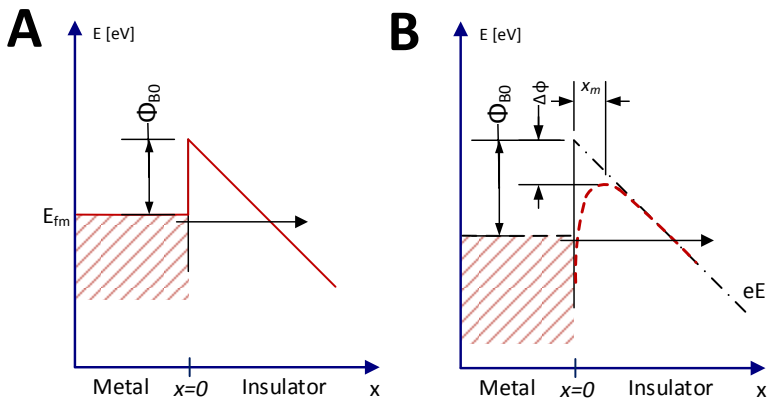

Figure 13. Fowler-Nordheim emission derived with triangular potential shape (A) and the impact of Field lowering effect (B).

Within the electrode, the potential energy range of electrons which are prone for tunneling is assumed to be somewhat below and up to the Fermi level. The electric field is assumed to be neglectable inside the metal as it would be neutralized by any available free charges. Outside the electrode the electric field is oriented perpendicular to the electrode surface [54]. This results in the potential equation displayed below and visualized in Figure 13 A.

$$\begin{cases} V(x) = -e\phi_{B0} & for\ x < 0 \\ V(x) = -eEx - \dfrac{e^2}{4x} & for\ x > 0 \end{cases} \tag{24}$$

The term $e^2/4x$ is the energy on the electron due to the image charge effect attracting the electron to the electrode, also shown in Figure 13 B. The image charge effect and the barrier height, are thus shared with Schottky injection model, and have a certain impact on the end result. By excluding the impact of the image charge effect from equation (24), the potential equation can be used in the one-dimensional time invariant SE (12), in order to derive an expression for this tunneling current. Contrary to Schottky equation, to find the total current integration is done from -∞ up to the Fermi level, as the temperature dependency is low. The equation for the injected current density originally derived by Fowler and Nordheim without the barrier lowering effect is as following:

$$J = \frac{e^3 E^2}{8\pi h \phi_{B0}} e^{\left(-\frac{4}{3}\sqrt{\left(\frac{2m}{\hbar^2}\right)}\frac{\phi_{B0}{}^{3/2}}{eE}\right)} \tag{25}$$

Where ϕ_{B0} is the barrier height in eV, e is the elementary charge, E is the electric field in V/m, h and $\hbar$ are Planck's ordinary and modified constants respectively and m is the electron mass. What is interesting is that this relation has a quadratic dependency on electric field, with an additional negative inverse exponential dependency. The pre-exponential part is stated to be difficult to notice in experiments. When fitting the above equation to experiments mainly on metallic tips in vacuum, the measured current density was higher. To some degree this was attributed to electrode roughness, but the lack of the barrier lowering effect was also a cause of

this deviation. As expression (25) is without the barrier lowering effect, it is interesting to also derive an expression with the barrier lowering effect, as it is seen in Figure 13B, that this effect reduces the thickness of the tunneling barrier to some degree. An approach has been made by Good and Muller [54], where the field lowering effect was introduced into the potential equation (24), with the following end result:

$$J = \frac{1}{t(\Delta\phi/\phi_{B0})^2}\frac{e^3E^2}{8\pi h\phi_{B0}}e^{\left(-\frac{4}{3}\sqrt{\left(\frac{2m}{\hbar^2}\right)}\frac{\phi_{B0}^{3/2}}{eE}v(\frac{\Delta\phi}{\phi_{B0}})\right)} \tag{26}$$

Where ϕ_{B0} is the barrier height in V, e is the elementary charge, E is the electric field in V/m, h and $\hbar$ are Planck's ordinary and modified constants respectively and finally $t(\Delta\phi/\phi_{B0})$ and $v(\Delta\phi/\phi_{B0})$ are functions varying between 0 and 1.2 depending on the effective barrier height as shown in Figure 14 below.

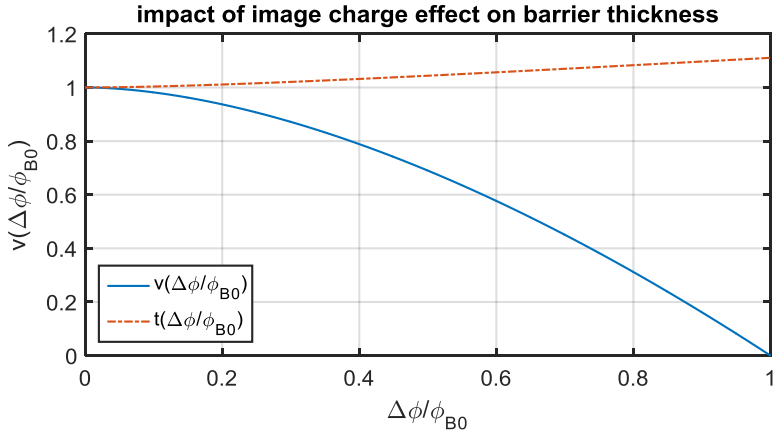

Figure 14. Plots of functions v and t used for calculating impact of image charge effect in equation (26).

The pre-exponential term $t(\Delta\phi/\phi_{B0})$ is thought to affect the total current density very little. However, the term introduced in the exponential affects the total current density significantly. This allows the expression to better match measurement results which previously had been explained by some degree of surface roughness, making the impact of surface roughness separable from impact of the image charge effect. Good and Muller [54] also derived an expression for the temperature dependency of Fowler-Nordheim injection. This affects the Fermi-Dirac distribution function as expressed in equation (13) in the metal, and for some electrons now at higher thermodynamic energy the barrier encountered will be slightly thinner, resulting in the following expression:

$$J(T) = J_0 A_T \frac{f_T(E)T}{\sin(f_T(E)T)} \tag{27}$$

Where A_T is a constant equal to $2{,}77x10^4$, J_0 is the current density at 0 K as expressed in equation (28), T is the temperature in K and $f_T(E)$ is a field dependent function as expressed below:

$$f_T(E) = t(\frac{\Delta\phi}{\phi_{B0}})\frac{\sqrt{\phi_{B0}}}{E} \tag{28}$$

Where $t(\Delta\phi/\phi_{B0})$ varies as shown in Figure 14, ϕ_{B0} is the barrier height in V, and E is the electric field in V/m. As expression (27) now includes the (weak) impact of temperature in the tunneling process, the injected current density can be estimated with a temperature and field dependency.

It should be noted that the expression for Fowler-Nordheim injection is derived from wave properties of electrons. Tunneling is a phenomenon valid for both electrons and holes, and as holes are commonly treated in solid state physics as particles with positive relive mass m_h^*, the derived expression should prevail given that the relative mass of the two particles is equal.

2.3.4.1 Impact of roughness and surface states

The impact of surface roughness on Fowler-Nordheim injection is a known subject, and originates from localized field enhancements in the same manner as for Schottky injection. Tunneling into vacuum is for this reason measurable in experiments already at electric fields exceeding 100 kV/mm when just a little roughness is considered [18]. Also others [45], [55] have discovered a clear impact of surface roughness in the magnitude of the field dependency of Fowler-Nordheim injection into vacuum. The impact of local asperities on the barrier height is shown in Figure 11 and the difference between Schottky injection and Fowler-Nordheim injection is that the latter one already exhibits a strong field dependency without any impact of the image charge effect, as expressed in (25), while the field dependency of Schottky injection solely depends on this phenomenon.

When it comes to the role of surface states, with their origin as presented in section 2.3.3.2, in the Fowler-Nordheim injection process, it is important to consider the entire barrier, the applied electric field and the energetic and space distribution of these states, as shown in Figure 15.

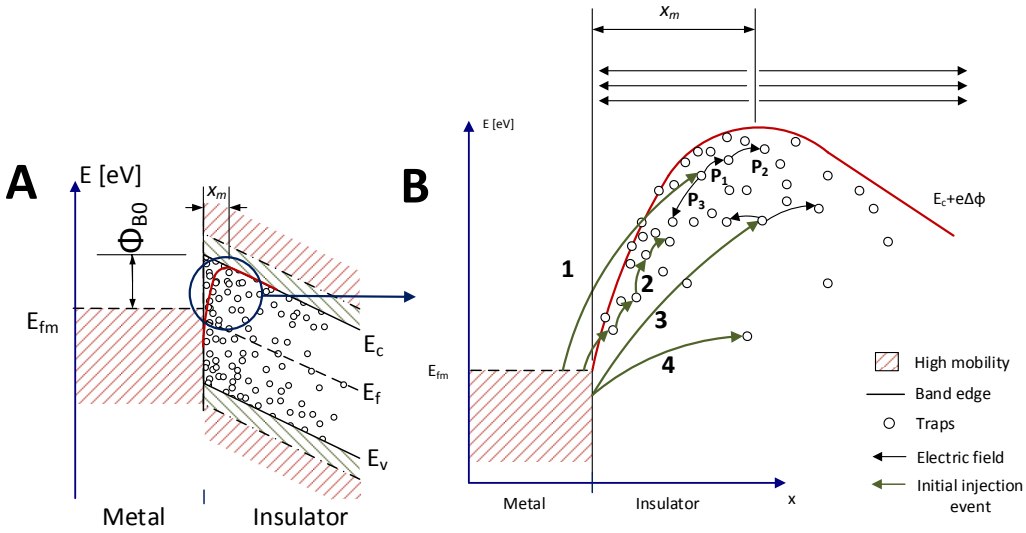

Figure 15. Tunneling phenomenon with presence of traps - view of the electron barrier (A), and close-up view of various tunneling (or hopping) events between trap sites in the interface barrier (B).

When first considering tunneling without thermal activation, the presence of surface states should not modify the expression significantly, other than the use of a slightly lower barrier height if the injected electrons are considered to end up in the mobility band instead of the conduction band, as shown in Figure 15 A. However, if thermal activation is considered in the

tunneling process (hopping), different scenarios can be considered (as shown by green arrows in Figure 15 B):

1) Schottky injection with thermalization (or hopping) into a state before x_m.
2) Subsequent hopping through the surface states.
3) Hopping into shallower traps beyond x_m.
4) Hopping into deep traps, beyond x_m.

All these events may occur with a certain probability and thus give a high or low contribution to the total injected current density. For electrons injected into states before the maximum barrier position (1), there will be a certain probability for the next hopping event to be away or towards the electrode, and this probability should have a certain dependency on the local electric field, decreasing the probability of the former one and increasing the latter one, due to the image charge potential. For subsequent hopping through the barrier (2) every hopping event away from the electrode is reduced in probability due to the image charge effect. For an electron injected beyond the maximum barrier position x_m (3) and (4), further conduction away from the electrode is likely though the depth of the trap it is injected into might limit how much this injection event will contribute to the total current density. Scenario (2) can be separated from the others in that the first hopping event does not overcome a significant amount of the total barrier height, while for the other scenarios, a certain part of the total injected current density is governed by a high number of electrons constantly being thermally activated within the adjacent metal and attempting to enter the material. Which scenario is dominating is dependent on the impact of the image charge potential. Without this force constantly pulling back the electrons, scenario (2) could be the dominating one, as modelled by Taleb et al [56] and Baldo et al [48], but with this effect taken into account, scenarios (1) and (3) will likely dominate the injection process as theorized by Arkhipov et al [49], Blossey [50], Scott and Malliaras [52] and Conwell et al [57]. The difficult part of these theories is that detailed knowledge about the trap distribution towards the surface is required to derive a relevant expression for the injected current density, and the impact of traps can both result in a lowering of the overall potential barrier, or the introduction of an additional field dependent effect in the injected current density [58].

To conclude, considering the trap distribution and energetic disorder (morphology) in the interface can explain the weak dependency of electrode materials and metal work function, giving the injection process a dependency on the surface properties of the insulation material. With the impact of the image charge effect taken into account, Schottky and Fowler-Nordheim models should still have a certain validity in that they constitute for a certain part of the injection process for low and high electric fields respectively. Their contribution is shown in Figure 16.

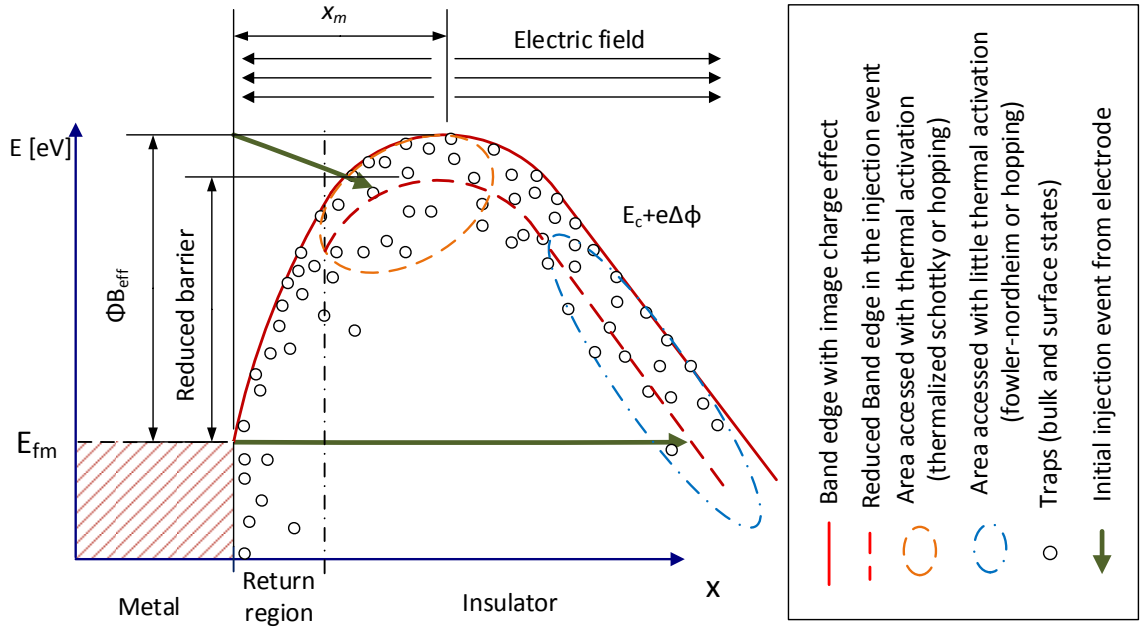

Figure 16. Additional barrier lowering due to traps/states within the band gap. The barrier lowering could affect both Schottky and Fowler-Nordheim injection to some degree. The return region is the area where injected charge carriers quickly return to the electrode due to the image charge effect.

Without detailed knowledge about trap distributions in the interface, using these injection laws with reduced barrier heights should be justified, with the knowledge that the field and temperature dependencies introduced could be inaccurate, especially when the amount of surface states introduced is significant. The amount of barrier lowering that can be applied can to some degree be related to the trap depth and density, as the reduced barrier drawn in Figure 16 should be somewhere within the depth of the traps that are contributing towards the conduction process. Whether only shallow traps contribute, or if some of the deeper traps also contribute is unclear. The magnitude of the reduced barrier should therefore be evaluated with care. For electric fields exceeding 100 kV/mm, the trap dependent injection expression derived by Arkhipov et al [49] predicts a very similar current densities as the equation derived by Fowler and Nordheim [53], this shows the validity of using equation (27) for predicting high field behavior of the charge injection process.

2.3.5 Charge extraction

Charge extraction and the formation of extraction barriers is a phenomenon frequently covered in semiconductor physics. For semiconductors, the formation of extraction barriers arises from the creation of a depletion region caused by thermally activated charge carriers moving to the adjacent metal. As thermally activated charge carrier pairs are uncommon in wide band gap insulators, the formation of this depletion layer is not applicable when a low degree of impurities is present. For XLPE, as mention earlier, there could be a significant presence of PDP if the material is poorly degassed. Given that the PDP concentration is high enough, these species could be ionized upon field application, with the possibility of creating an extraction barrier towards an electrode due to the blocking of ionic charge carriers [34], and/or due to leaving behind ionized molecules close to the interface creating this extraction barrier similar to the depletion region in semiconductors. An extraction barrier of 0.8 eV was employed by Fukuma et al [38], to investigate the impact of PDP in a bipolar charge model. Delpino et al [59] also claim that PDP can create an extraction barrier and try to simulate an extraction barrier

artificially by the use of a fluorinated ethylene propylene (FEP) film in their sample configuration. At 60 kV/mm injected charge managed to cross their 0.25 mm thick film within several seconds upon field application, creating a heterocharge accumulation towards the artificial extraction barrier, greater in magnitude as could be explained by MWS interfacial polarization. Extraction barriers are thus closely linked to heterocharge formation, which due to electric field enhancement at the interface link directly to premature breakdown.

The image charge effect could to some degree counteract the formation of an extraction barrier [40], as it aids with the escape of carriers close to the electrode-insulator interface. To which degree the image charge effect and to which degree interface dipoles [48] exist in the interface could impact the magnitude of a formed extraction barrier. Physical interfaces could to some degree lack from the beneficial properties of image charge effect, when the interstitial material used has similar permittivity as the insulating material and the roughness significantly decouples the insulator from the electrode. Also, the insulator surface states could be separated more from the electrode due to the roughness, moving them away from the image charges and thus making them influence the injection and extraction properties. Comparing the injection properties of the same rough polymer surface used as a chemical and a physical interface is thus crucial to assess the impact of surface roughness.

2.3.6 Bulk conduction processes

This section describes the conduction properties in the bulk of the material.

2.3.6.1 Hopping conduction

As previously mentioned, hopping conduction is a combination of thermally activated transfer and tunneling of charge carriers between localized states in the material. Inter-chain conduction through the weak Van-der-Waals bonds in between the polymer chains is referred to as the hopping mode of electron transport [60], using the shallow traps in the material. Assuming an electronic carrier located close to the local Fermi level, at a certain distance from the band edge, pure thermal activation all the way up to the band edge is unlikely to occur as the required thermodynamic energy would be too high. Also pure tunneling would be difficult as the distance between trap sites of equal energy level would be too large, as tunneling features an exponential decay of the probability density of the electron. Adding a thermal activation to the electron can give it an identical energy level to a much closer adjacent trap site, allowing it to tunnel to this site. This greatly increases the probability of charge transfer between traps and is defined as hopping. The distance to different neighboring traps and their energy level thus dictate the probability that hopping can occur. An expression for the resulting current density for hopping conduction is:

$$J = A_0 \sinh(^{eE\lambda}/_{2k_BT}) \tag{29}$$

Where A_0 is a constant of proportionality, e is the elementary charge, E is the electric field in V/m, λ is the spacing in between vacancies (for ions) or traps (electrons and holes), k_B is Boltzmann's constant and T is the temperature in K. Hopping is thus a form of thermally-assisted tunneling, without the electron ever being in the conduction band.

2.3.6.2 Poole-Frenkel effect

Poole-Frenkel effect for bulk conduction is very similar to the image charge barrier lowering effect derived for Schottky injection, where a certain field dependency is created through the

superposition of the electric field of the charge carrier towards the barrier and the background electric field. For the Poole-Frenkel effect, the ionized donor or acceptor (for holes) site is instead the driving force for the barrier lowering. An illustration of Poole-Frenkel effect is shown below in Figure 17 for low and high electric fields.

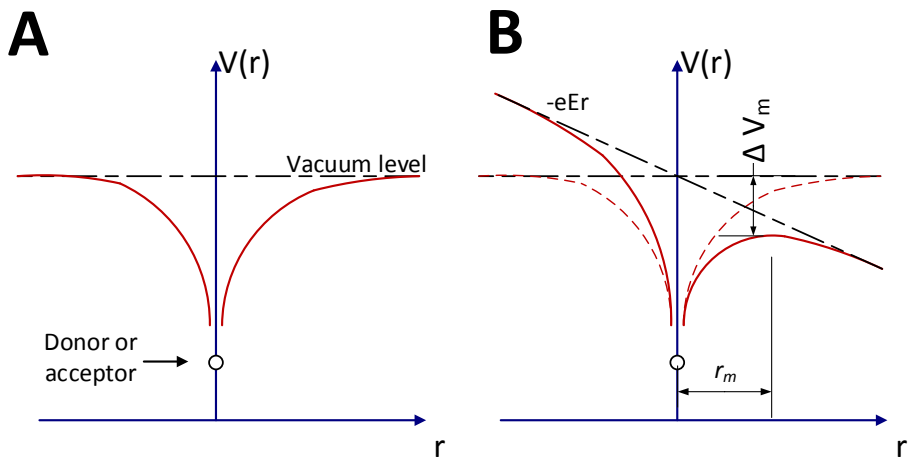

Figure 17. Coulomb electric potential near ionized donor site at low electric field (A) and high electric field (B)

As the energy required for activating the donor or acceptor in polyethylene is large, the donors or acceptors do not contribute to doping of the material, as is the case for semiconductors. Instead any excitation of charge carrier from a donor state will result in the excited carrier to be captured again by a neighboring state. The donor states are thus traps, and the related conduction process through the traps in the material becomes field dependent due to the interaction of the charge carrier with the ionized donor state. This interaction results in the following impact on the conductivity of the material:

$$\sigma = A_0' e^{-(\Delta E_D/2k_BT)} e^{\sqrt{e^3E/4\pi\varepsilon_0\varepsilon_r}/k_BT} \tag{30}$$

Where A_0' is as expressed in equation (31), ΔE_D is the required thermodynamic energy required for detrapping, k_B is Boltzmann's constant, T is the temperature in K, e is the elementary charge, E is the electric field in V/m and ε_0 and ε_r are the vacuum and relative permittivity respectively.

$$A_0' = e\mu\sqrt{N_D N_{eff}} \tag{31}$$

Here e is the elementary charge, μ is the mobility, N_D is the density of donor states and N_{eff} is the effective density of states in m^{-3}. The exponential field dependency of Poole-Frenkel effect is originating from the barrier lowering effect shown in Figure 17. As the expression (30) is derived in one dimension, the actual barrier lowering effect in three dimensions, sometimes referred to as the Hartke's equation [61], is known to be somewhat lower than the one-dimensional case.

2.3.6.3 Space charge limited conduction

The impact of the density of electronic carriers on bulk conduction processes (drift), and the impact of traps can be described through space charge limited conduction (SCLC). SCLC describes often the conduction phenomenon for thin polymeric films, as for thin films any field

inversion capabilities might be low as space charge is less non-uniformly distributed. In SCLC theory only electrons are accounted for and steady state is assumed. Three regions can be identified as shown in Figure 18; the ohmic region, the trap limited region and the trap free region. In the ohmic region, the conduction in the material is by drift of the electrons, and the injected charge concentration is too small to affect the electric field significantly. When the injected charge concentration is big enough, also diffusion can become locally significant, but this is neglected in this theory, instead a uniform space charge concentration is assumed in the entire material. The increased charge density does locally affect the drift, increasing the field dependency of the conduction. This creates the following expression for the current density:

$$J = n_0 e\mu \frac{V}{d} + \theta_0 \frac{9\varepsilon\mu e V^2}{8d^3} \tag{32}$$

Where n_0 is the charge density, μ is the free carrier mobility, V is the applied Voltage, d is the electrode spacing and θ_0 is the ratio of free charge density compared to the total charge density. The first part in this equation represents the ordinary drift (ohmic transport), while the second part stands for concentration assisted drift, which is thus space charge limited. The regions are marked in Figure 18. Traps will limit the conduction process in both cases, but at a certain threshold, the charge concentration will exceed trap concentration. This creates the trap free region, as the free charge density increases through θ_0. As all traps are gradually filled, charge mobility increases significantly. For a single level of traps, this will make distinctive threshold, but in reality, there is a spread in trap energy level, favoring a smoothened transition as drawn with the dotted line in Figure 18.

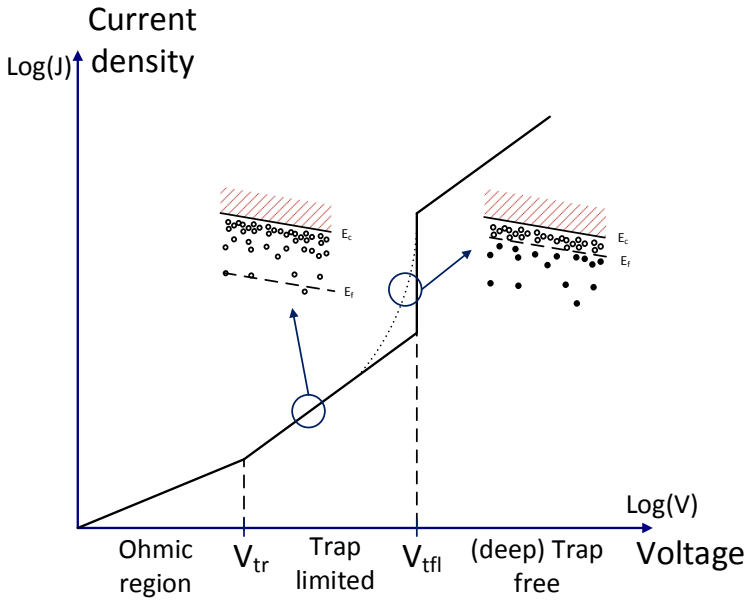

Figure 18. Space charge limited conduction with traps

When all traps are filled, any additional electrons will be hot electrons in the conduction band with significantly higher mobility. The higher mobility, will in turn allow the electrons to gather higher speed, and conduct according to the Drude model, increasing the probability of ionizing collisions with the lattice. The presence of charge concentrations exceeding the trap concentration could thus be harmful to the material. While the SCLC neglected the impact of barrier lowering effects on the injection, such an effect should only lower the voltage thresholds on to which the different transitions are reached. The diffusion of charge species is neglected,

by assuming a uniform charge distribution. The J-V relationship from SCLC is therefore seldom scalable to the total current density found in thicker specimens, but the different transitions could occur locally in the material, for example close to an electrode.

The SCLC model can be extended in order to take the Poole-Frenkel effect into account [62]. This can predict a higher current density for higher electric fields, when the barrier reduction in the Poole-Frenkel effect becomes significant. Murgatroyd [62] managed to derive the following expression:

$$J = \theta_0 \frac{9\varepsilon\mu e V^2}{8d^3} e^{\left(\frac{0{,}891}{kT}\sqrt{\left(\frac{e^3 E}{\pi\varepsilon_0\varepsilon_r}\right)}\right)} \tag{33}$$

where the added-on parameters are the same as expressed previously for the Poole-Frenkel effect in equation (30). What can be learnt here is that an additional, yet slower transition in current density depending on electric field is added to the expression. The shift in current density can thus be difficult to observe experimentally both due to the variations in trap depth and the impact of the barrier lowering effect. Assessing the trap density through SCLC measurements can therefore be a difficult task.

If additional electrons can be added after filling up of the states in the material (nearby local asperities of an electrode), such electrons could cause local damage to the material, as any of these electrons would be hot and have far higher mobility than in the mobility gap. According to the Drude model this would also increase their maximum velocity, increasing the probability that the impact with the polymer lattice could be ionizing, leading to degradation in such areas. A created space charge cloud also move, enhanced by own electric field and diffusion, which sometimes is referred to as charge packets.

2.3.6.4 Ionic transport

The free volume in the bulk, at crystalline interfaces in the material, allows for the presence of polar species (such as PDP), which can be ionized under electric field application. As the motion of ionized species can influence the leakage current, and since introduced polar species can create local states, it is desirable to keep polymeric high voltage materials as clean and dry as possible. Also chemical impurities can originate from press films materials [63], and can lead to non-monotonic leakage currents.

2.3.7 Summary of conduction phenomena and non-ideal effects

To conclude, the impact of surface roughness can be assessed by simple means and introduced through localized FEFs, and is a factor which influences the field dependency of injected current densities. The impact of surface states and surface morphology can be more difficult to assess, as they affect the encountered barrier height. On the other hand, bulk conduction effects, such as Poole-Frenkel effect, the field dependency of hopping conduction, and localized charge accumulation may reduce the severity of localized field enhancements at electrodes. Depending on the average height of the injection barrier, when taking into account the non-ideal barrier properties, the overall behavior of the electric transport can be injection-limited or bulk-limited [49], [48]. What this means is that if the averaged barrier is sufficiently low, the externally measured current density will no longer be governed by the interface, but rather by bulk space charge effects. For bulk-limited systems such as SCLC there will be an influence of sample thickness on the external current density, while for injection limited ones there should be no

influence off sample thickness. The conduction phenomena described in this theory section are summarized in Table 3.

Table 3. Field dependency of conduction phenomena and possible impacts of surface roughness, surface states and surface morphology. Here parameter β is a constant.

	Surface phenomenon	**Field dependency**	**Surface Roughness**	**Surface states**	**Surface morphology**
A	Schottky injection	$J \propto e^{\beta\sqrt{E}}$	Local asperities increase current density [44].	Hopping model needed [52], [50].	Affects barrier height [35], [47].
B	Fowler-Nordheim injection	$J \propto E^2 e^{-\beta\frac{1}{E}}$	Local asperities significantly increase current density [45].	State to state hopping through the barrier with [49] or without image charge effect [48].	Affects energetic disorder in hopping process [48].
C	Charge extraction	Extraction barrier results in heterocharge formation.	Absence of image charge effect towards interstitial material [39], or interface dipoles [48] create extraction barrier.	Extraction barrier formation with high PDP concentration [38], [59].	Extraction barrier only possible if significant surface crystallinity is present [18].
	Bulk phenomena	**Field dependency**	**Surface Roughness**	**Trap density**	**Morphology**
D	Poole-Frenkel effect	$\sigma \propto e^{\beta\sqrt{E}}$	Could reduce FEF:s depending on size of asperities.	-	Band gap difference between crystalline and amorphous regions [34], [35].
E	Hopping	$\sigma \propto \sinh(\beta E)$	Could reduce FEF:s depending on size of asperities.	Mobility affected by shallow and deep trap density.	Band gap difference between crystalline and amorphous regions [34], [35].
F	Recombination	N/A	-	Mobile charge carriers can recombine with mobile or trapped opposite carriers.	Band gap difference between crystalline and amorphous regions [34], [35].
G	Trapping/Detrapping	N/A	-	-	-
H	SCLC	$J \propto E^2$	Hot electrons can degrade the material, most likely close to asperities.	Higher (deep) trap density reduces the probability of hot electrons.	Band gap difference between crystalline and amorphous regions [34], [35].

The conduction phenomena listed in Table 3 are also visualized in Figure 19 for a sample with a chemical and a physical interface. The impact of morphology and differences between crystalline and amorphous regions is not shown in the figure.

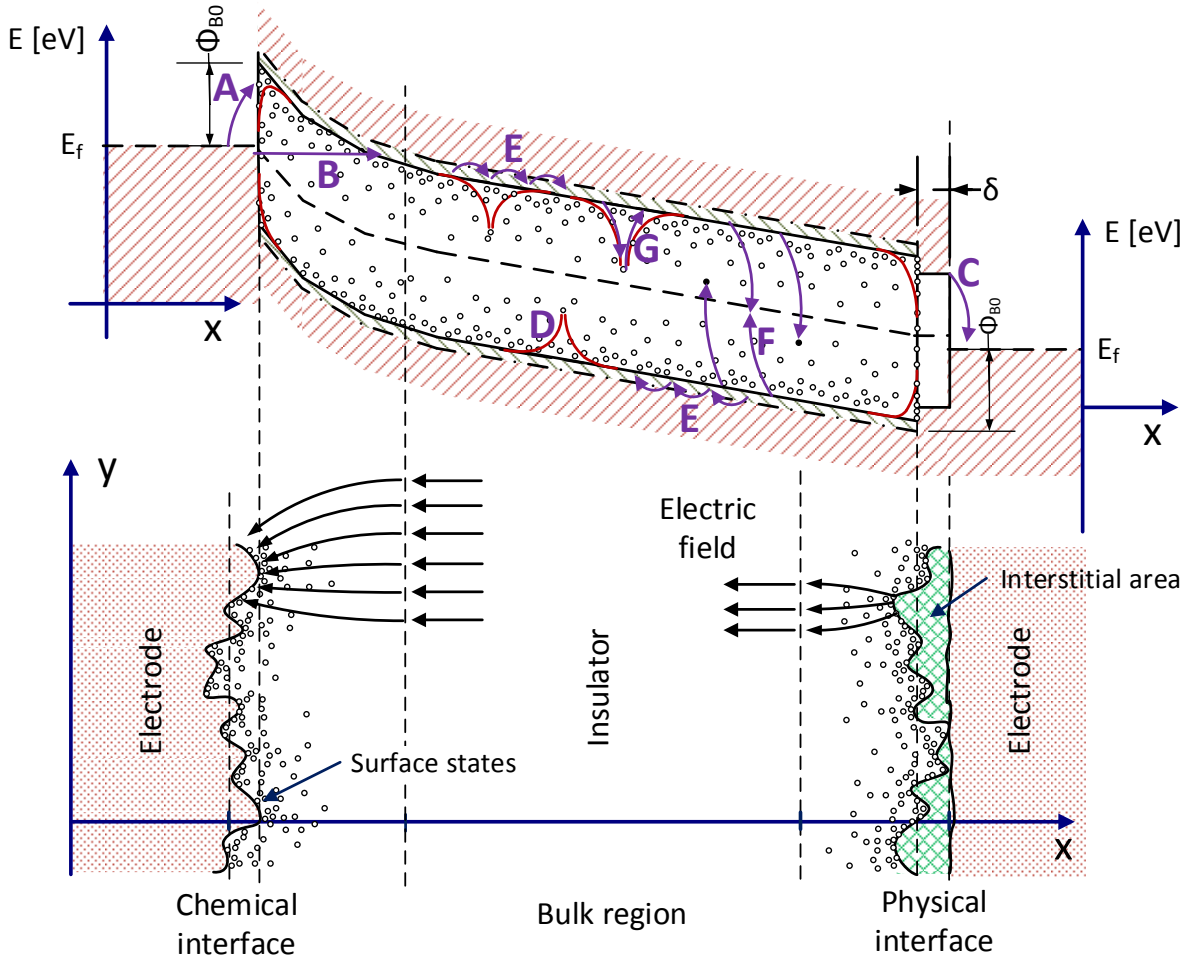

Figure 19. Band gap model highlighting conduction phenomena listed in Table 3 (top) along the x-axis shown in the bottom figure that illustrates a full x-y map highlighting non-ideal interface effects. A rough chemical interface and a rough physical interface are shown. Note: certain effects shown are exaggerated and the band bending is due to the enhanced field near asperities.

As shown in Figure 19, the way the interstitial area interacts with the insulator is of great importance for understanding behavior of a physical interface. Such areas are present in many HVDC accessories. They can be dry, greased, oiled etc. A simplified approach, treating this area as part of the electrode can be adopted if:

- The carrier concentration and mobility in the interstitial area exceeds that in the insulation by many orders of magnitude, such that the injection barrier from this interface into the insulator remains seemingly unaffected.
- This also results in the resistivity and electric field of the interstitial area being many orders of magnitude lower than in the insulator.

Such a simplification will eliminate the impact MWS polarization on this interface, and reduce the impact of the surface states of this physical interface. What will be left is the impact of the surface roughness of the prepared polymeric surface, and any electrical effects will be mostly governed by the insulation material alone. If such a simplification cannot be done, various effects can affect the performance of the physical interface, including an impact on what interstitial material is used (grease, air, oil etc.).
The model shown in Figure 19 can be adopted to model HVDC cable accessories at locations where the outer semiconductive layer terminates and the prepared insulation surface is mated

with the semiconductive part of pre-molded accessory body. In such an application, the chemical interface in Figure 19 is the extruded interface, likely of very low roughness and a low amount of surface states, while the physical interface is created through the cable preparation method. In addition, such an application features cylindrical geometry, and a temperature gradient upon transferring significant power in the cable.

2.4 Hypotheses

The purpose of formulating the hypotheses in this thesis is to construct a theoretical framework capable of explaining the significant differences in DC breakdown voltages found during tests on cables, which end interfaces were prepared by different means. As illustrated in Figure 20, also shapes of the breakdown channels differed in such tests. These results are closer described in Chapter 4.

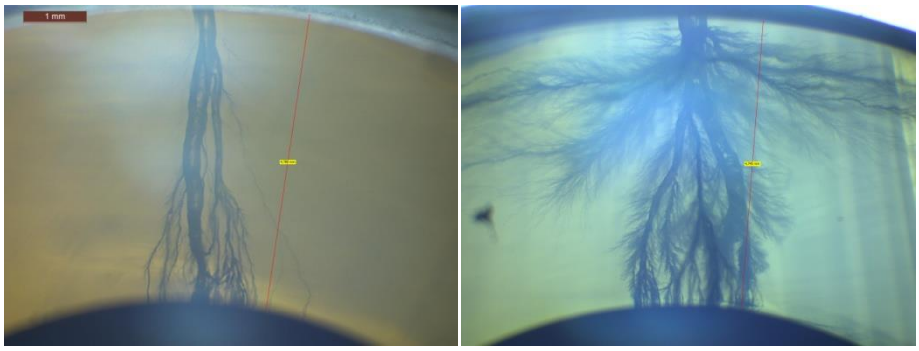

Figure 20. DC breakdown voltage patterns observed on MV-size cables where an abraded surface (left) led to a breakdown at low electric field, while a cut surface (right) led to a breakdown at high electric fields.

2.4.1 Hypothesis A – Roughness enhanced injection

Roughness and surface states influence the injected current density into the tested material, predominantly controlled by Schottky and/or Fowler-Nordheim injection mechanisms. The degree of surface roughness is believed to affect the current density, especially at asperities, to a point where there may locally exist very high current densities. Also the total averaged current density at the interface may be affected by presence of surface states, which lower the barrier for carrier injection and shift the injection effects towards lower electric fields.
This phenomenon can ultimately lead to a breakdown in two ways:

A-1. At the asperities, all the traps within the band gap will be filled up due to the increase in charge carrier density. The trap free conduction regime will be reached (following SCLC mechanism) and the additionally injected charge carriers will start degrading the material, yielding the onset of a void, followed by treeing and thereafter breakdown. It should be noted that for this failure mode to occur, a very high local space charge concentration is required as the local trap density could exceed 10^{22} m^{-3} if shallow traps are considered, or 10^{20} m^{-3} if only deep traps are considered in the bulk of the material [34].

A-2. The average injected current of the rough electrode becomes so high that the injected charge begins to propagate towards the other electrode as charge packets. At some point this will affect the field distribution in the insulation bulk in such a way that a breakdown will occur.

These hypotheses are visualized in Figure 21.

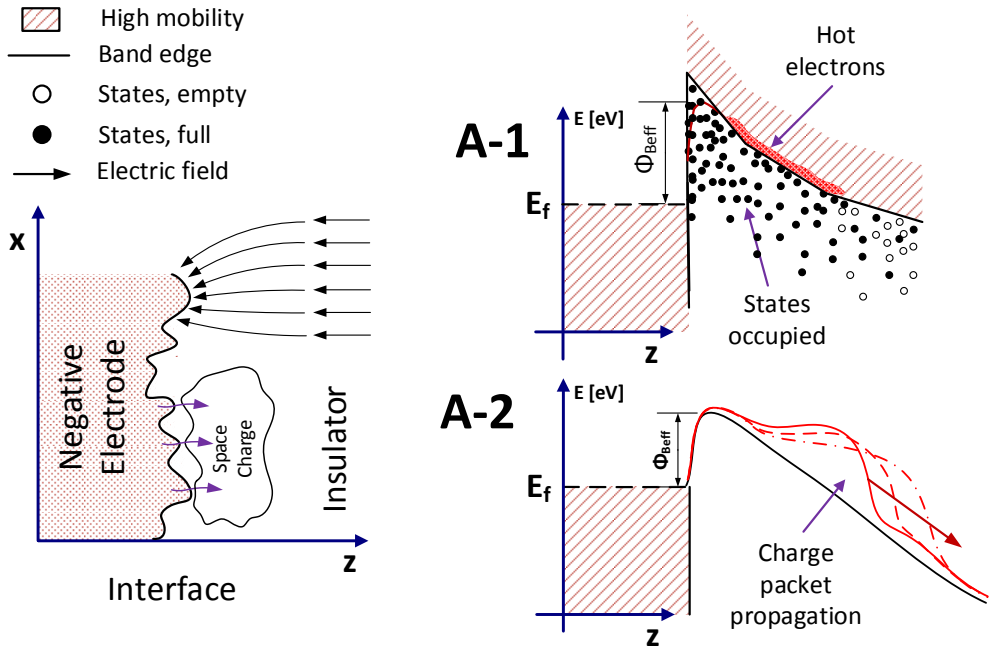

Figure 21. Presence of hot electrons according to hypothesis A-1 or charge packet propagation according to hypothesis A-2.

For such a mechanism to be viable for a physical interface, the interstitial material needs to be assumed to be a part of the electrode. While both phenomena can result in a scaling effect between full scale samples and small scale samples, such as plates, the origin of such a scaling effect could differ. For hypothesis A-2 a significant field inversion is required, which should be less prominent for thinner samples. For hypothesis A-1 a significant local charge accumulation is required, which might be less prominent for thinner samples, caused by a higher recombination rate due to a lower carrier transit time across a thinner sample. These theories should make the phenomenon reproducible on plate samples, without any exact replication of both interface types found in the application (such as the grease layer between the accessory and the cable), apart from the polymer surface. It shall be noted that these two theories could explain the shape of the breakdown channels shown in Figure 20.

2.4.2 Hypothesis B – Formation of extraction barrier

The physical interface and interstitial material (with its thickness depending on surface roughness) locally decouples surface states of the insulator from the electrode. Such an effect could affect accumulated charge in the interface, or eliminate the image charge effect, changing the extraction properties of the interface. This would be related to formation of heterocharge, and predict a breakdown from the physical interface, as shown in Figure 20. The decoupling of surface states and image charge effect is shown in Figure 22.

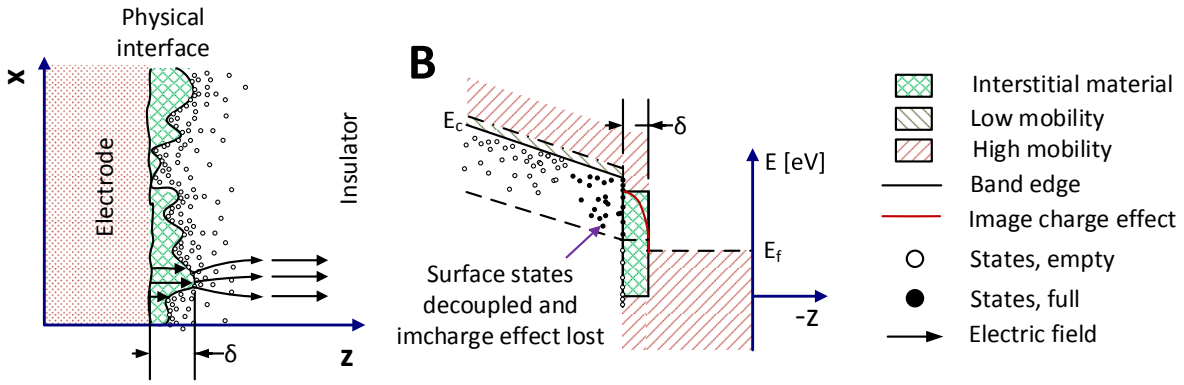

Figure 22. Formation of extraction barrier due to decoupled surface states and loss of image charge effect according to hypothesis B. The extraction barrier is not drawn, but the formation of such a barrier is counteracted to some degree by the image charge effect.

Even though this theory might be rather complex, it would make the breakdown process dependable on the used interstitial material, and predict different behavior of the chemical and physical interfaces, such that it can be separated from hypothesis A. On the physical interface, a reduction in charge decay times should be found in SPD measurements.

2.4.3 Hypothesis C – Treeing initiation due to field enhancements

Treeing initiation is affected by the irregularities on the surface. Two possible ways could be:

C-1. The asperities locally enhance the electric field in the insulator, leading to degradation and tree formation without the impact of charge injection (hypothesis A-1), but rather due to the local field enhancement.

C-2. Treeing initiation process is caused by electron acceleration in the interstitial material. The surface roughness could introduce regions were hot electron bombardment will be enhanced, causing the initiation of the first void for electrical treeing in such a region.

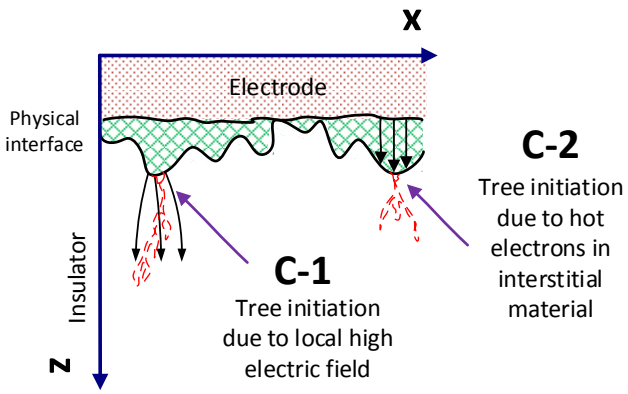

Figure 23. Treeing initiation du to electron acceleration according to hypotheses C-1 and C-2.

If the physical interface is recreated on small scale samples, the breakdown levels obtained on larger samples should be somewhat scalable. For hypothesis C-2 the low breakdown level should not be observable on chemical interfaces. While hypothesis C-1 could also give low breakdown level for chemical interfaces, the breakdown level should be in direct relation to the FEF, such that roughly abraded surfaces can give significantly lower breakdown levels.

2.4.4 Hypothesis D – MWS charge due to electrode decoupling

The roughness affects significantly the charge accumulation in the interface through the extended MWS mechanism. This charge accumulation in the interface could be caused by discrepancies in electrical parameters on both sides of the interface through equation (7) and also other factors influencing the conductivity in the materials. The accumulated charge could most likely lead to a premature failure if the electrical field is enhanced in the interstitial material, through heterocharge formation.

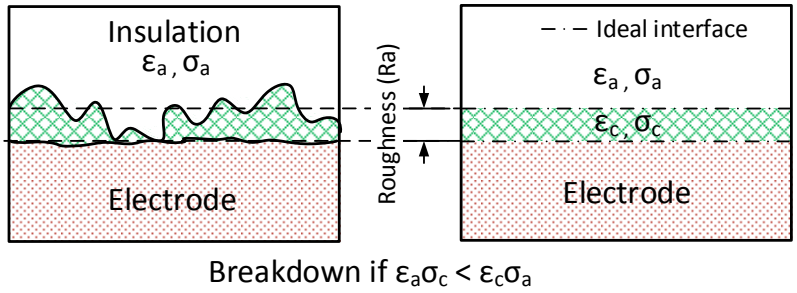

Figure 24. MWS mechanism of physical electrode-insulator interface

This theory predicts that there should be an influence of the used interstitial material and also on the ramping speed through the magnitude of the time constant τ. The extended MWS model is not applicable for chemical interfaces, so the breakdown phenomenon should not be found in these. Also, there should be an explanation for a significant reduction of conductivity in the interfacial layer for this theory to predict a breakdown.

2.4.5 Final remarks

Additional complexity to prove validity of these hypotheses will be encountered if two (or more) of the phenomena are involved in the breakdown process. Also other phenomena which are not mentioned here could affect this process.

Chapter 3

Experimental procedures

This chapter introduces the experimental procedures used in the thesis. First the sample manufacturing methods are described, followed by the physical and chemical characterizations carried out in the thesis. At last the used electrical characterizations are presented.

3.1 Sample manufacturing

The surface preparations referred to as "abraded" "cut" and "remolded" were made on a full-scale DC grade XLPE cable end. These are procedures feasible for making real joints and terminations, and little to no adaption were made to these procedures within this thesis. These procedures include a cleaning step eliminating most of the small particle contamination. The cable had been priory degassed and screened according to normal industrial procedures. After making the surface preparation, the cable peelings were cut from the surface layer of the insulation, using a specially designed rotational cutting tool, as shown below in Figure 25.

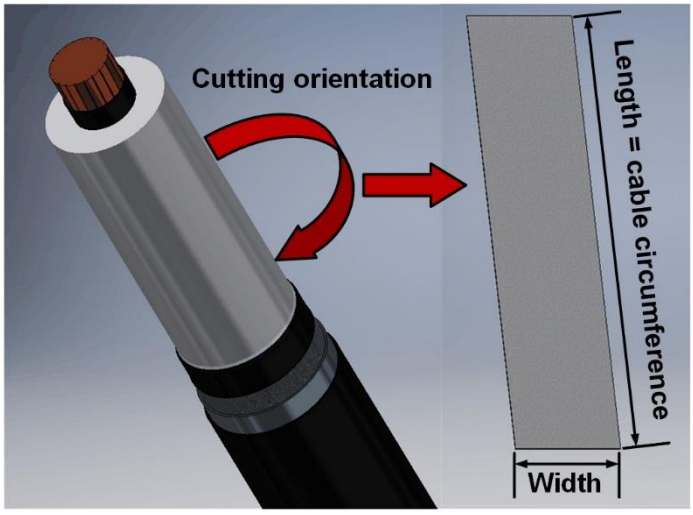

Figure 25. The manufacturing process of a cable peeling

The dimensions of the cable peelings that can be made with this method were:

- Width: 30-100 mm.
- Length: around 300 mm depending on cable dimensions.
- Thickness: 0.1-1 mm.

Since only the surface layer was used and the tool was manually operated, the major difficulty was coping with non-ideal cable dimensions such as ovality and straightness, which in turn affected the thickness variation within each cable peeling. Due to the high variations in thickness many of the electrical tests performed in this thesis have been adapted to make sure that this variation has been taken into account. Accurate thickness measurement of the sample was always done after the electrical tests, as this measurement very easily affects the surface structure of the sample.
The cable peeling process as shown in Figure 25, also introduces a new surface type referred to in this thesis as "backside" originating from cutting motion in the peeling process. The backside

is thus different from the other surfaces in that it cannot be found and replicated in real accessories, and that each cable peeling has such a surface on one of the sides, unless stated otherwise.

The use of cable peelings as test object is not novel, as others [64][65][66] have also used this method in different ways. On one side, the sample size can be reduced, by using a microtoming process [66], with the benefits of more accurate sample dimension control, with the drawback of no longer cutting in the angular orientation of the cable. On the other side, bigger samples could be machined in a lathe, with the drawback of heat development in the manufacturing process and difficulties to machine samples with a thickness lower than 1mm. The present method used in this thesis has thus its advantages in that it suffers from neither of these limitations.

Cleaning of the surface with 100% polypropylene wipes and technical alcohol was also performed when needed, with the outmost care not to scratch the surface during this process. After manufacturing, the cable peelings were stored in an incubator at around 10-12 % RH to eliminate the influence of moisture on the measured properties.

For the DC breakdown tests performed on medium voltage cables within this thesis, the surface preparations were made on a smaller size cable end. Minor changes were made to the preparation methods due to the smaller diameter of this cable, but the overall manufacturing method and principles remained the same.

3.2 Chemical and physical surface characterization

This section focuses on the non-electrical characterization carried out on the cable surface. Small sections of the cable peelings were used as these samples have identical surface characteristics as the cable surfaces, and allowed for easy implementation in these measurement methods.

3.2.1 SEM

For scanning electron microscope observations (SEM), one minute of gold sputtering was applied to the sample surface using an S150b Edwards sputter coater. The SEM was performed using secondary electrons (SE).

3.2.2 Optical profilometry

Three-dimensional roughness parameters as well as the surface texture, were assessed on all surfaces by means of optical profilometry. A Wyko RST plus interferometer was used using white light interferometry. The surfaces were sputter coated with gold for 3 minutes to improve the reflective capability of the surfaces, as the opaque white appearance of some of the surfaces needed to be enhanced in order to increase the amount of valid data points obtained with the scan. The obtained data points, (a plane with X, Y and Z coordinates) where post-processed for the removal of global profiles by using a third polynomial plane removal. For each surface the roughness parameters were assessed by taking the average 5 measurements of each surface type. The most typical measured surface of each sample type was selected for further data processing and calculation of field enhancement factors.

3.2.3 Contact angle measurements

Sessile drop measurements using deionized water were used for assessing the advancing and receding contact angles of the surface types. These contact angles were observed across and along the surface texture. From the obtained contact angles, the SFE was calculated using formulas (1), and (2). A correction for the surface roughness was made through equation (3). For the roughest surface, also air pockets present underneath the droplet was accounted affecting the area fraction in equation (3). This air presence was only found for the abraded surface, and for this surface, the droplet was observed from above in a microscope, after which the image was postprocessed in Matlab where an illumination threshold could separate light pixels with possible air presence from darker pixels, and contact fraction of 75 % could be estimated. The calculated SFE was compared with a DYNE test set, which was able to determine the surface energy with increments of 2 mN/m. In the DYNE test, the lowest possible liquid was found which fully wetted the surface ($\theta_m=0$).

3.2.4 HPLC measurements

High-performance liquid chromatography (HPLC) was performed at the technical material center in Halden. In this method, polymer samples are taken at different positions, after which they are solved in a mixture using a solvent. The mixture is then passed through a column, and the difference in flow rates through the column allows for separation and identification of different components from the original sample. The used equipment was an HPLC system with UV detector (Agilent 1260 HPLC).

3.2.5 FTIR-ATR measurements

Fourier transform infrared spectroscopy with attenuated total reflection used as sampling technique (FTIR-ATR) was performed at the technical material center in Halden. The measurements were carried out with two different crystals for a variation of the penetration depth. The used crystals were Diamond (Dia) and Germanium (Ge) with the penetration depth at 45° being 1,66 μm and 0,65 μm respectively. The background spectrum was filtered out to avoid changes in the ambient air during the measurements. For each sample, a minimum of three separate scans were obtained on each side of the sample.

3.3 Electrical characterization

The electrical characterization in this thesis consists of surface charge decay measurements and DC breakdown tests. While charge decay measurement was on only carried out on cable peelings, the DC breakdown tests were carried out both on cable peelings and medium voltage sized DC cables.

3.3.1 Surface charge decay measurement

Charge decay measurements or commonly referred to as surface potential decay measurements (SPD) were performed to determine electrical surface properties. This measurement is performed by placing a sample on a grounded electrode, and exposing the top surface to corona charging, to deposit surface charge on the sample. A Kelvin probe connected to an electrostatic voltmeter (Trek model 347B) was used to capture the voltage decay, and the sample plate was mounted on a robotic translation fixture allowing it to move in the x-axis, as shown in Figure 26. This motion allowed for capturing line scans against time, and allowed the resting position of the sample to be away from the probe and corona needle. The ground electrode used applied

a slight stretch in the cable peeling, with a spring-loaded system, for the peeling to rest flat on the electrode. This system was built inside a closed container as constructed by S. Alam et al [67], capable of varying the pressure through a vacuum pump, and featuring a dehumidified environment using a CaCl solution bringing the relative humidity below 12% during the tests. Charging voltages of -5 and -10 kV where used with 2 or 1 minutes of charging duration. After charging, the sample was moved away from the charging needle prior to grounding, for avoiding back discharges towards the grounded needle.

The SPD characteristic can on low conductive materials, such as LDPE at room temperature, be affected by a multitude of electrical phenomena, as listed below.

A) Charge injection from ground electrode, thermally activated.
B) Charge injection from ground electrode with low thermal activation.
C) Charge detrapping from the charged surface layer.
D) Bulk conduction effects.
E) Surface conduction along the charged surface of the film.
F) Charge recombination to ambient air.

While effects A-D (shown below in Figure 26) could not be eliminated from measurements, efforts were made to avoid effects E and F as much as possible.

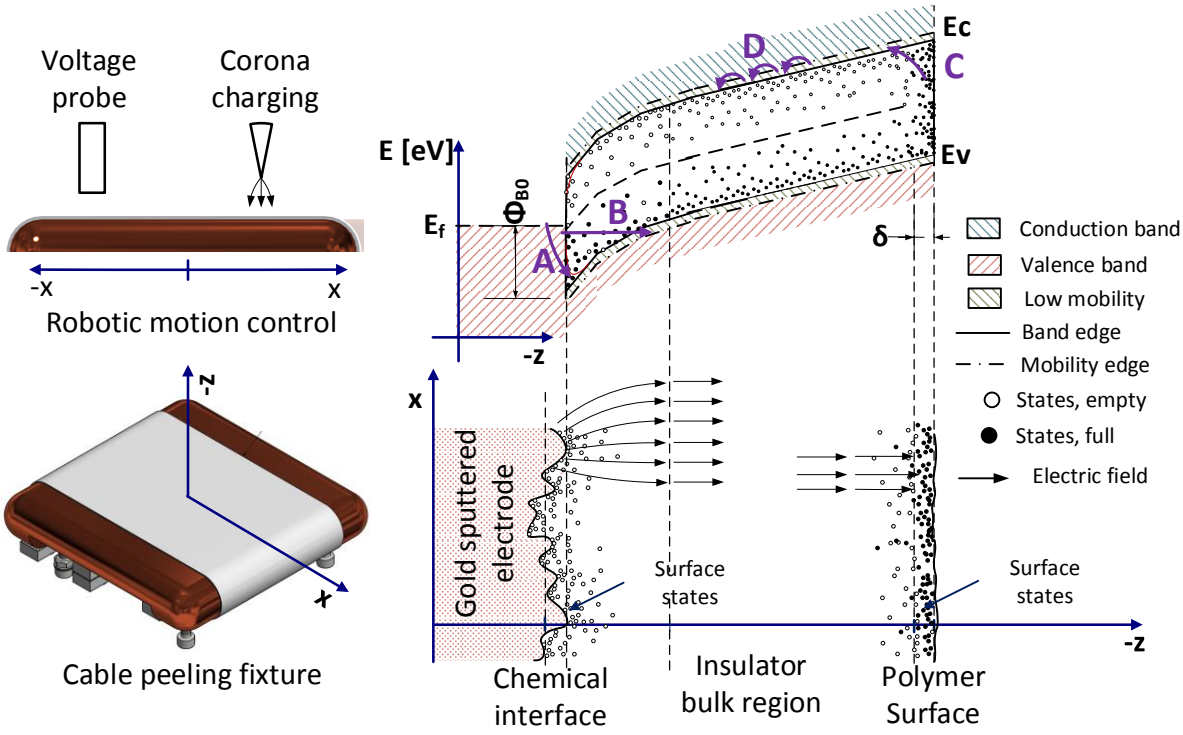

Figure 26. Setup for SPD measurement on cable peelings and illustration of interfaces and related band gap during the decay process. The band gap is shown at a position of field enhancement at the ground electrode, caused by using a rough surface.

The implemented dehumidification reduced the possibility of having any adsorbed polar layers (such as moisture or other liquids), which can influence the surface conduction properties [60]. The line scans obtained against time did allow for monitoring that each measurement was without significant surface conduction along the surface. The use of reduced pressure within the tests cell was not implemented as a measurement showed that this resulted in significant

surface discharging in the regions with surface field greater than the breakdown level of the ambient air, which was lowered by the pressure reduction according to the Paschen's law. The absence of ambient recombination was confirmed by the variation of sample thickness in the measurements.

Since the measured SPD was a combination of the remaining electrical effects A-D highlighted in Figure 26, the samples were tested with both the prepared surface types towards the charging source, and with the surface types towards ground plate. With the test surface oriented towards the ground electrode, the presence of opposite charge injection can be investigated, as it has been shown to significantly influence the SPD above a certain field, as modelled by D. Min et al [37], but also confirmed experimentally by Zhuang et al [68], [69]. The measurement of injection properties with the test surface oriented towards the charging needle surface could be more difficult, as the initial charge distribution within the polymer surface could consist of charged ions remaining on the surface, or already injected in a surface region with unknown penetration depth δ, as illustrated in Figure 26. The ground electrode was gold sputtered for 6 min to ensure good electrical contact between the sample and the ground plane, but also to get an electrode with well-defined work function of 5.1 eV during the measurements.

The conductivity was determined by using equation (34), which is a combination of Ohm's law and the continuity equation for electric currents.

$$\frac{\partial V}{V \partial t} = -\frac{\sigma}{\varepsilon} \tag{34}$$

Here V is the surface potential obtained in the measurement, σ is the conductivity and ε is the permittivity of the sample. The decay characteristics were analyzed in Schottky and Poole-Frenkel plots, where the characteristics where plotted against √E as equation (22) and equation (30) have such a field dependency.

3.3.2 DC breakdown studies

DC breakdown was carried out on two sample geometries; MV-sized cable ends and cable peelings. The MV-sized cable end geometry was chosen for its similarities to the full-size cable application, while cable peeling tests were utilized to develop a cost-efficient method capable of testing cable surfaces on both purposely made samples but also samples cut out from cable systems in operation.

3.3.2.1 MV sized cables

For the ramped DC breakdown tests, the sample geometry was used as reported in [70], and the exposed cable ends were connected to a DC generator. A general illustration (not to scale) of the tested cable end is shown in Figure 27.

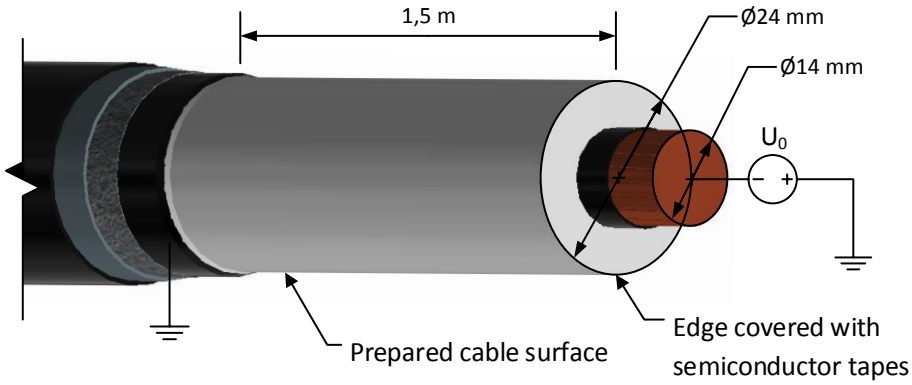

Figure 27. Geometry of MV-sized cable end (not to scale) for DC breakdown testing.

No accessories or components were placed onto the cable surface, creating a surface towards ambient air. The test cell was dehumidified to reduce the risk of flashovers during the tests. After the tests, microscopic observations were used to investigate the breakdown characteristics and to determine the sample thickness at the breakdown position. The latter was used to calculate the average electric field during the test.

3.3.2.2 cable peelings

For performing breakdown tests on the cable peelings, a specialized test cell was manufactured. The test cell is illustrated in Figure 28.

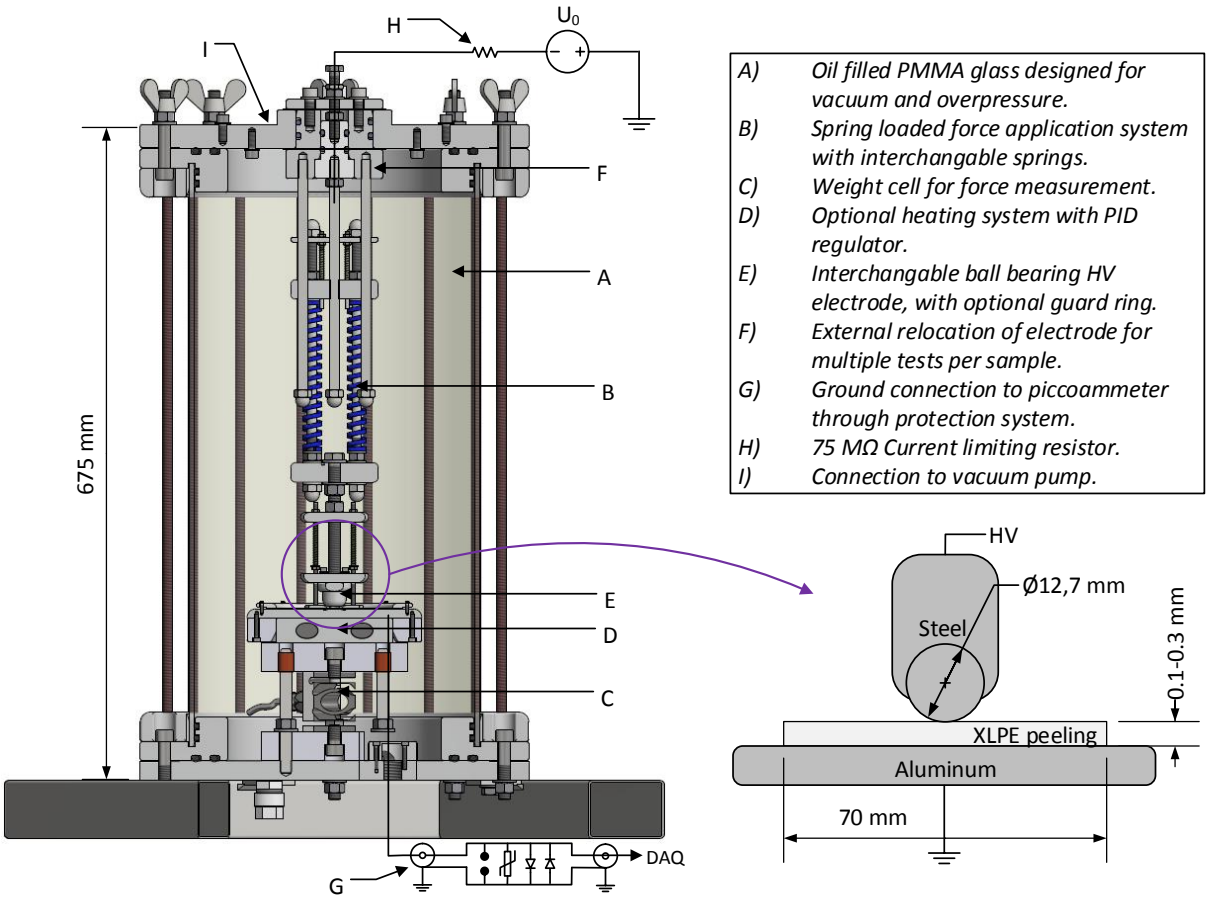

Figure 28. Design of the DCBD test cell and illustration of the used sphere-plane geometry electrode.

The test cell was filled with a specific transformer oil suitable for DC voltage and with breakdown strength exceeding 30 kV/mm. The used mineral oil also had good properties for moisture tolerance in comparison to conventional silicon oils. The sample was inserted from the top, after which a vacuum treatment was performed, effectively eliminating air pockets trapped between the sample and the ground plate, and elsewhere in the system. The spring-loaded system was only used very lightly, as the ball bearing electrode easily creates high mechanical stress at the tip. The resulting imprint of this electrode was consistently below 1.5 mm in diameter. The observed leakage current was below 1 μA for all tests, giving a maximal voltage drop over the current limiting resistor of 75 volts. Since an automatic ramping and triggering system was implemented, low ramping voltages and long test durations were possible, with remote supervision of the tests. The settings of maximal output current from the voltage source was kept low to limit the power dissipation during the breakdown to be below 300μW, excluding discharge of the capacitance within the test cell. For each test, the applied voltage, current profile, transient currents during the breakdown, breakdown magnitude, location and sample thickness at breakdown location were recorded.

As shown in Figure 28, the used geometry was sphere-plane with a steel bearing ball and an aluminum ground plane both of which had been polished to a high degree of smoothness. As the system was submerged in oil, the ground electrode featured a physical interface with interstitial material of mineral oil. In some tests the ground electrode side of the sample was gold sputtered for 6 minutes to change the nature of this interface type.

3.3.2.3 Weibull statistics

The averaged breakdown field was obtained by dividing the breakdown voltage over the thickness at the sample position, and was investigated with the aid of the two-parameter Weibull distribution to estimate the failure probability given by equation (35).

$$P(E) = 1 - e^{-\left(\frac{E}{E_c}\right)^{\beta}} \tag{35}$$

Here E_c is the characteristic breakdown stress and β is the shape parameter of the distribution. The validity of the inverse power law calculating the breakdown time is also useful to consider an is given by:

$$t = KE^{-n} \tag{36}$$

Here K and n are parameters relating the breakdown field to time-to-failure. For different test series to be comparable, the field magnitude and application duration is thus of importance, which can be challenging if there is significant variation in the sample thickness due to the peeling manufacturing process. For this reason, also averaged breakdown field against sample thickness was investigated to see if any trends were visible within the possible thickness range. The inverse power law also predicts a scaling effect between the thin cable peelings and the MV cable breakdown test. The exact characteristics of the parameters of the inverse power law were not investigated, as it is known that space charge effects within the tests significantly affect the applicability of the inverse power law [71].

Chapter 4

Results

This chapter presents the results obtained in the thesis. First the chemical and physical characterizations are presented, to show the non-electrical characteristics of the created cable peelings. These are followed by a section presenting the results of the electrical tests, i.e. electrical breakdown tests and SPD measurements.

4.1 Chemical and physical surface characterization

This sections presents the results of SEM, optical profilometry, contact angle measurements, HPLC and FTIR-ATR measurements.

4.1.1 SEM

SEM analysis was performed to investigate the surface texture and topography of the created surfaces. The results are shown in Figure 29 below.

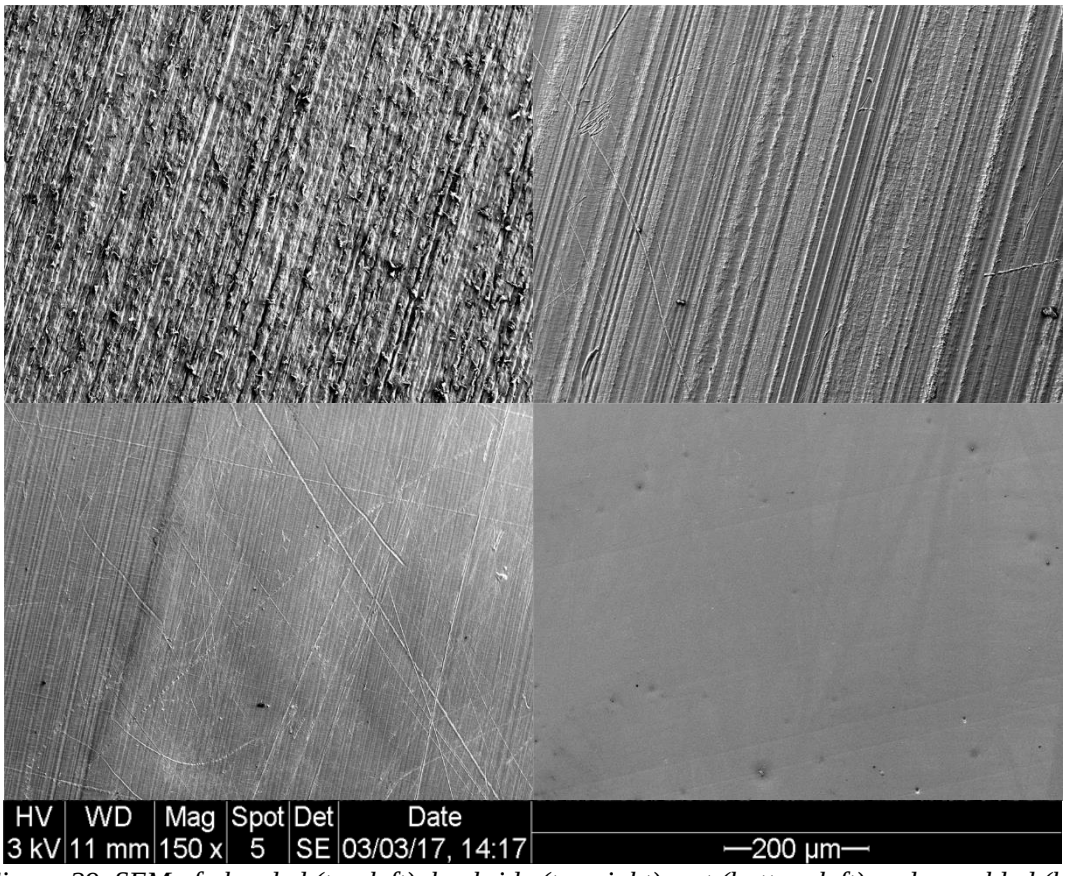

Figure 29. SEM of abraded (top left), backside (top right), cut (bottom left) and remolded (bottom right) surface types at 150 times magnification.

Minor scratches and non-embedded contaminants (dust etc.) are present on the surfaces, with most of them likely originating from the sample handling and the cleaning process, and can be

seen in Figure 29. Determining what scratches were created during sample handling can be done by checking the angular orientation of these scratches, and if they show any irregular surface texture. The surface texture shows also more regular patterns originating from the preparation method, which were further investigated with higher magnification as shown in Figure 30 below.

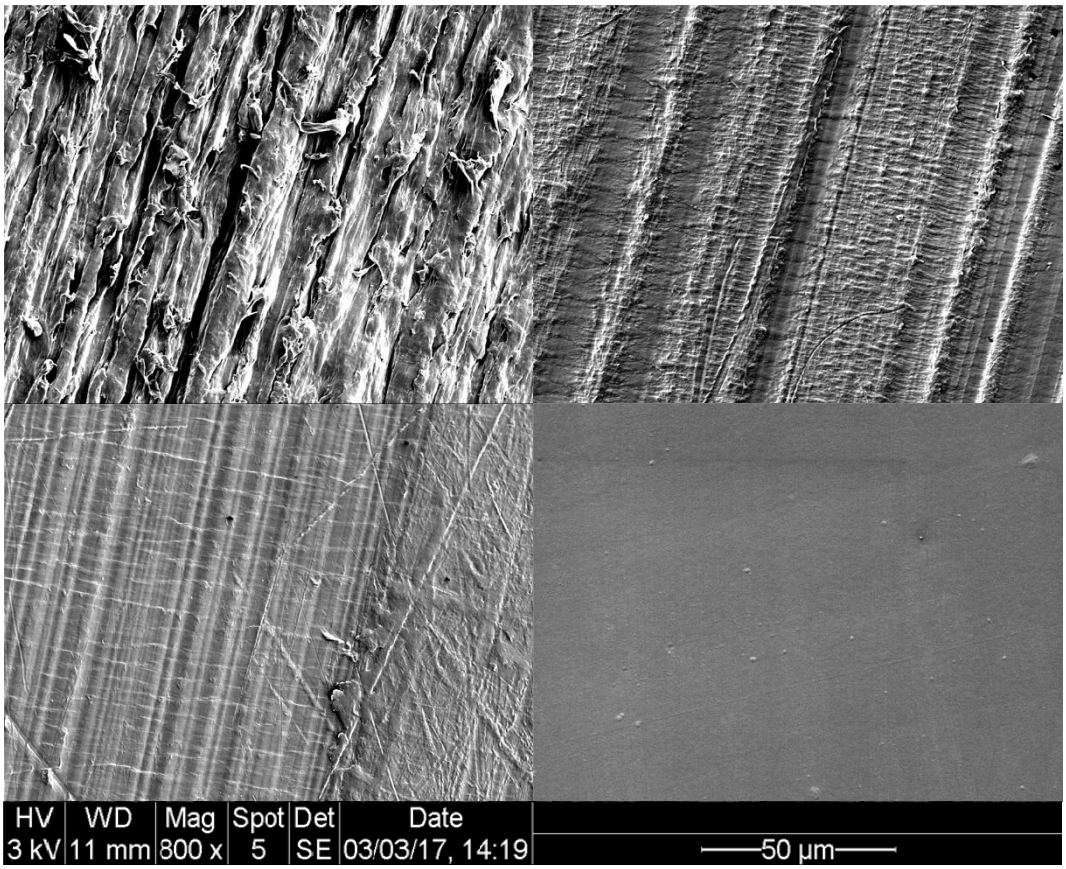

Figure 30. SEM of abraded (top left), backside (top right), cut (bottom left) and remolded (bottom right) surface types at 800 times magnification.

As observed in Figure 30, the abraded surface texture shows scratches in the abrasion direction as well as small folded peaks, also reported earlier by Hasheminezhad et al [19]. The scratches originate from the grains of the abrasion paper rubbing along the surface and pulling off polymeric particles. It is likely that the peaks originate from a yielding process, occurring when polymeric particles are pulled off from the surface. The backside and cut samples in Figure 30 show striations of different magnitude in the cutting direction. These striations likely originate from imperfections on the cutting knife edge. Lines parallel to the orientation of cutting edge (near horizontal lines in Figure 30) are also observed, which could be caused by fracture mode of material removal during the cutting operation. These lines do not resemble any severe knife chatter traces; as such traces would be indicated by lines with a repeating profile, and knife chatter should also introduce a higher degree of roughness to the texture as was observed here. The remolded surface is smooth and the texture becomes a replication of the polymeric contact film used in this preparation method. The abraded surface was also observed with different magnifications creating the same domain as used in the optical profilometry as shown in Figure 31.

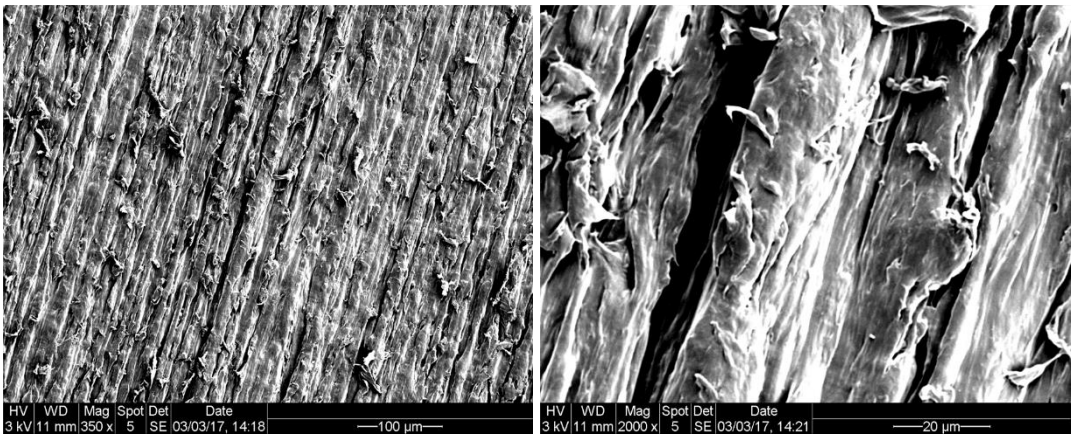

Figure 31. SEM of abraded with nearly the same domain size as optical profilometry (left) and the FEF calculations (right).

The measurement domain for optical profilometry was 612 x 460 µm, which seems to catch the full characteristics of the surface, as seen in Figure 31. For the domain used for FEF calculation as further described in Chapter 5, the size was around 100 x 80 µm and is at the minimal limit. Further reduction of the domain could result in loosing repeatability, as the texture size would exceed the domain size.

4.1.2 Optical profilometry

The three-dimensional roughness parameters of the polymer surface were calculated from the obtained data of the optical profilometry measurement and are shown in Figure 32 below. Two new surfaces of higher surface roughness, referred to as rough abraded and roughest abraded, were also introduced as it was desired to see the impact of surface roughness amongst the abraded samples.

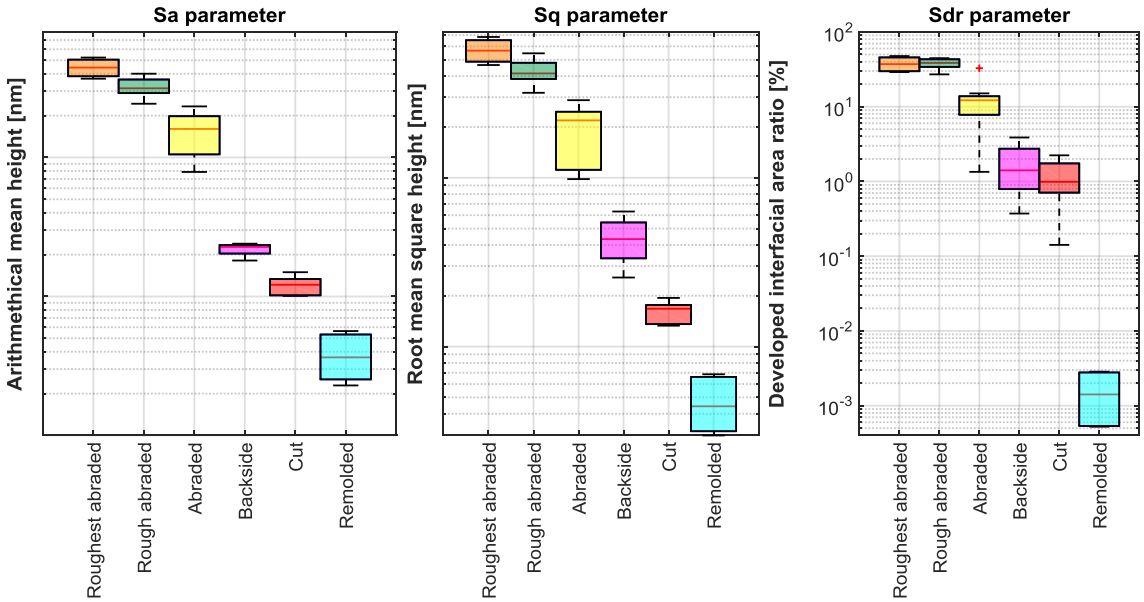

Figure 32. Height parameters Sa and Sq and hybrid parameter Sdr for the tested surfaces.

The arithmetical mean height (Sa) and the root mean square height (Sq) shown in Figure 32 consistently show the difference in surface roughness originating from the type of preparation method, with the abraded surfaces being the roughest and the remolded surface approaching

roughness levels found in semiconductor devices. The abraded surface shows a slightly higher standard deviation, originating from taking data from many different test series on surfaces produced at different occasions. The deviation is thus likely originating from variations in how the preparation method was performed. As the biggest variation in roughness, spanning over several orders of magnitude, is mainly dependent on preparation method, this data can be treated as the assigned roughness for each surface type. Individual roughness measurement of each batch or each individual sample could thus be avoided. The developed interfacial area ratio (Sdr), describing the increase of surface area due to the surface texture, shown in Figure 32 was further used for SFE calculation through the Cassie-Baxter equation as performed in section 4.1.3. The developed interfacial area ratio could also be related to a higher surface trap density, as the increased surface area could have place for more terminated polymer chains, but as there seems to be significant variation in this parameter in-between different batches, this should result in the same variation in electrical properties in between batches of the abraded, backside or cut surface types. Three-dimensional surface parameters describing the maximum valley (Sv), maximum peak (Sp) and the difference between these two parameters (Sz) found in each measurement was also analyzed and is shown in Figure 33 below.

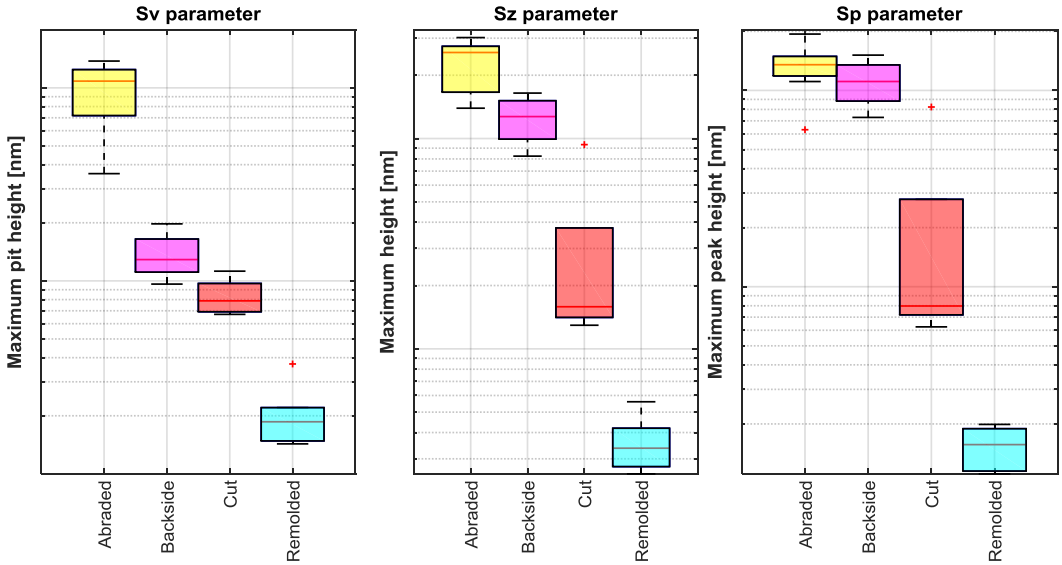

Figure 33. Height parameters Sv, Sz and Sp for the tested surfaces

As the Sp, Sv and Sz parameters are related to single points in the measurement, and as these are often not very repeatable between measurements, this resulted in bigger standard deviations. The Sv parameter is suitable to estimate the biggest possible void that could be created when the surface is used in a physical interface with air as an interstitial material. As the maximum pit height repeatedly shows to be below the magnitude of surface roughness required for PD activities, as illustrated in Figure 5, this electrical phenomenon could be eliminated from further evaluations. Rougher abraded surfaces could be above this threshold, so the use of the rougher abraded surfaces in dry physical interfaces was avoided in this thesis. The data obtained with optical profilometry is also presented in a histogram shown in Figure 34.

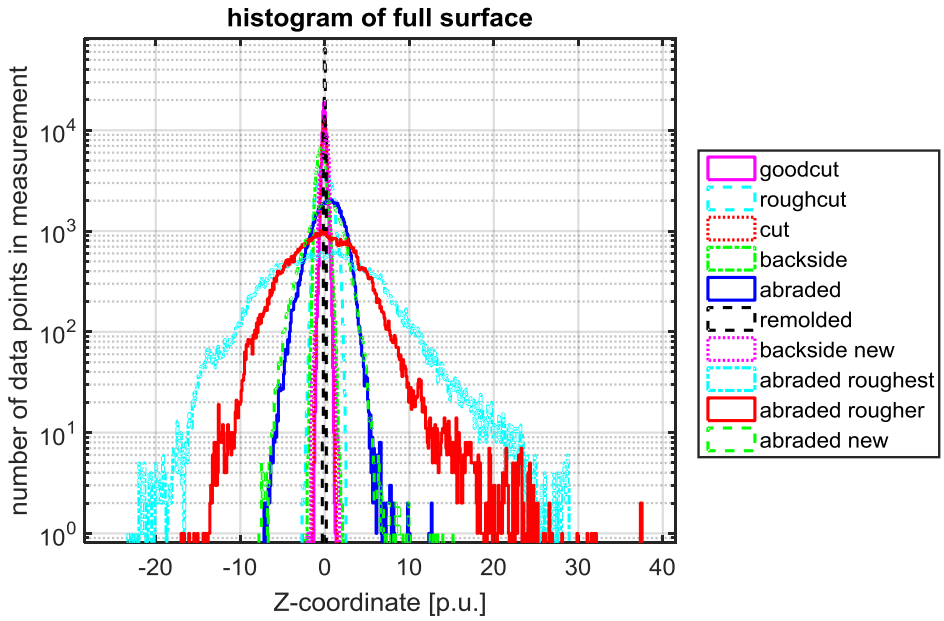

Figure 34. Histogram over the height population amongst the data points for the most typical measurement of each surface type.

It shows that all the surfaces in general follow a normal distribution, thus indicating that comparing various properties against the arithmetical mean height (Sa) seems to be a good choice.

4.1.3 Contact angle measurements

Measured contact angles using deionized water with surface tension of 72.5 mN/mm are shown in Figure 35 below, for the observation directions along and across the surface texture on the tested surface. Besides the four typical surface textures, an additional series of measurements was made on backside and oxidized backside surfaces, for testing the repeatability and oxidation sensitivity of the method. The oxidation was performed by subjecting the sample to hot air until substantial color change was noticed.

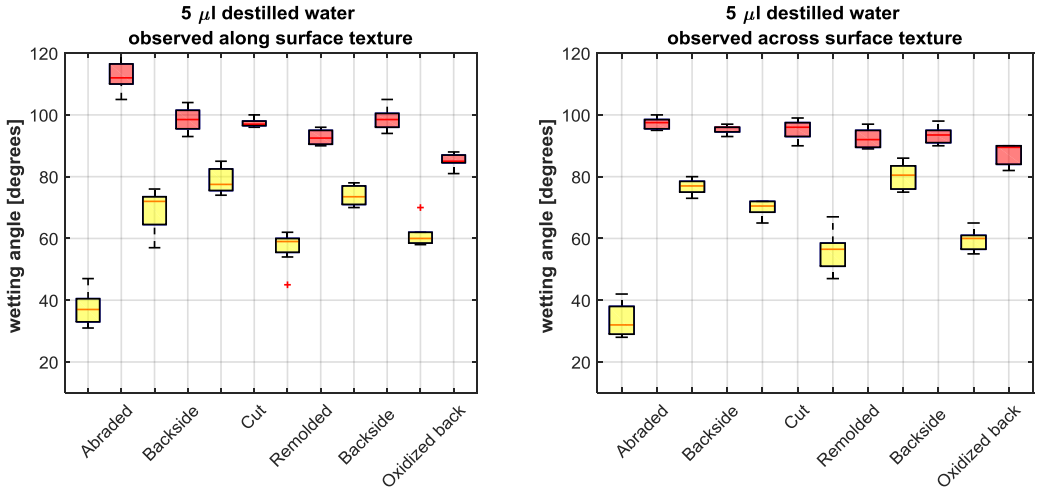

Figure 35. Observed advancing (red) and receding contact angles (yellow) of the surfaces when the observation is made along (left) or against (right) the surface texture.

The low standard deviations found in the measurements shows good homogeneity over the sample surfaces, and the contact angle seemed repeatable and sensitive to surface oxidation. Heterogeneity was found depending on the observation direction, which reflects the influence of the surface texture on the measurement, and the magnitude of heterogeneity was the largest for the roughest surfaces.

With results shown in Figure 36, three different methods were used to calculate the surface free energy (SFE) from the contact angles observed along and across the surface texture. The use of the Neumann method as per equation (1) yielded similar results as when using contact angle hysteresis as per equation (2). However both methods suffer from not including the effect of surface roughness according to the Cassie-Baxters state described by equation (3). By calculating the Young's contact angles using the previously determined developed interfacial area ratio, and using the area fraction of 75% for abraded, while the other surfaces had an area fraction of 100%. The results of calculating the SFE with the Neumann method from the Young's contact angles is shown to the right in Figure 36.

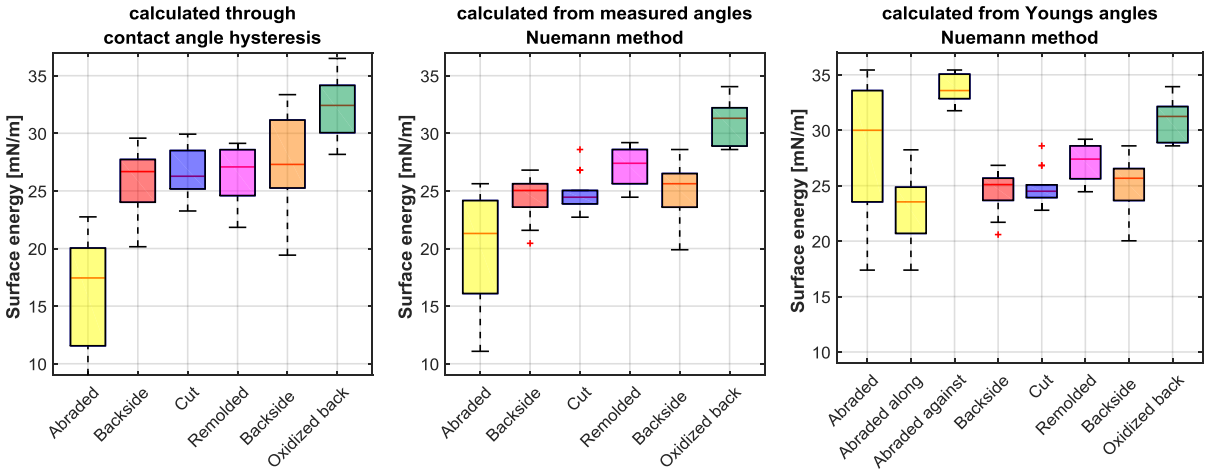

Figure 36. Calculated surface energies using the contact angle hysteresis (left), the Neumann method (middle) and the Neumann method correcting for roughness using the Cassie-Baxter formula (right).

The roughness correction observed by comparing the middle and right graphs in Figure 36 does not influence the results significantly for all surfaces except for the abraded surface. The remolded and oxidized backside surfaces show a slight increase in SFE which could be related to the introduction of carbonyl groups, as heat is used in these processes and oxygen atoms should attract the droplet more to the surface. A large standard deviation is observed for the abraded samples, which is coming to the differences in contact angles depending on observation direction. As a non-directional roughness parameter is used for the roughness correction, the deviation is not reduced by the roughness correction. In the roughness corrected SFE in Figure 36 separate boxplots were added for the SFE of abraded surfaces for the contact angles observed along and across the texture. These two observation directions should represent the minimal and maximal SFE which can be obtained depending on observation direction, indicating that the average SFE of this surface should lay somewhere around 30 mN/mm. Also, the analysis of the air pockets underneath the water droplet for the abraded surface could introduce a certain degree of uncertainty, and without this effect taken into account the average SFE of the abraded surface was around 23 mN/mm. The calculated SFE from Figure 36 can be compared against the results from the DYNE test shown in Table 4.

Table 4. SFE obtained from the DYNE test with and without roughness correction.

Sample	Abraded	Backside	Cut	Remolded	Backside	Backside Oxidized
SFE from DYNE test [mN/mm]	36	29	27	27	29	32
Roughness corrected SFE [mN/mm]	32.5	28.5	26.7	27	28.5	31.3

For the DYNE test, no air can be present under the liquid as the liquid wets, so only the developed interfacial area ratio of the surface was used for SFE determination, which slightly reduced the SFE. The observation direction does not create any issues in the DYNE test, besides the fact that the fully wetting droplets had an oval shape on the abraded surface, compared to a circular shape on the other surfaces. The results presented in Table 4 somewhat match the SFE results calculated by means of the roughness corrected Neumann method shown previously in Figure 36.

The SFE determined in this section shows some interesting trends for the remolded and oxidized surfaces but these observations need additional confirmation from different measurement methods as the accuracy in the contact angle determination is relatively low. The texture of the abraded surface lowered the degree of wetting and created uncertainty in the calculations. The lowering of wetting of this surface was expected as it was shown Figure 5 that increasing the surface roughness further will ultimately result in a superhydrophobic state.

4.1.4 HPLC measurements

The results of the HPLC measurement on differently prepared cable ends are shown in Figure 37 below.

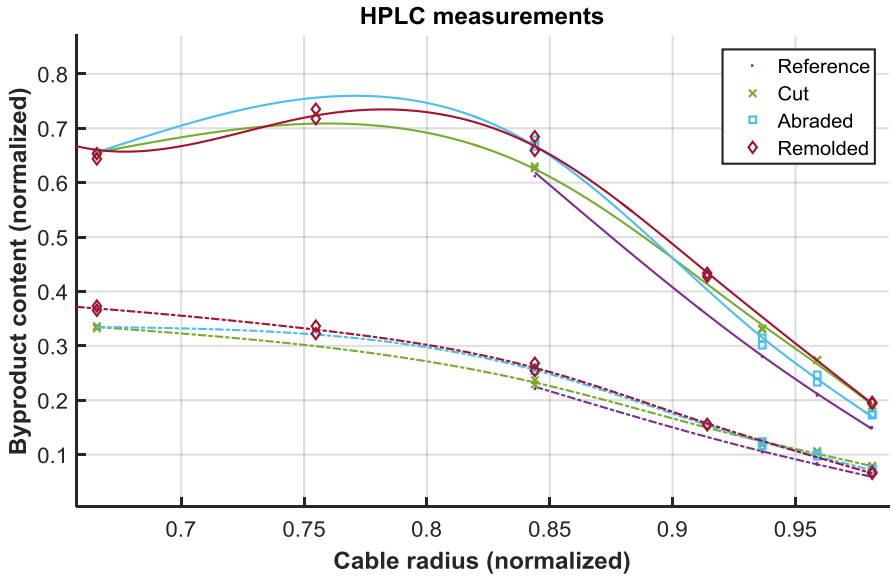

Figure 37. Byproduct content of cable sections with differently prepared surfaces. The quantities are for cumyl alcohol (solid curves) and acetophenone (dashed curves).

Besides the byproducts shown in Figure 37, the contents of alfa-methyl styrene, dicumyl peroxide or methane were below the detection level. No significant impact on the byproduct distribution in the cable end was found depending on preparation method. Also, the additional points taken towards the surface (shown to the right in Figure 37) showed no significant deviations, hence it can be assumed that the impact from the preparation method on the

byproduct distribution is minimal. The byproduct content found in the cable peelings after 3 months of storage in the incubator was also tested and is shown in Table 5 below.

Table 5. HPLC measurement on stored cable peeling

	Before peeling, in surface area	After 3 months' storage, 0.7 mm sample	After 3 months' storage, 0.4 mm sample
Cumyl alcohol [ppm]	585±4	180±7	138.5±3.5
Acetophenone [ppm]	198.5±2.5	43.5±4.5	26±1

The results on cable peelings, indicate an outgassing of the byproducts during storage. Besides the byproducts shown, the contents of alfa-methyl styrene, dicumyl peroxide or methane were again below the detection level. The low contents in the cable were caused by cable degassing following normal industrial procedures prior to the manufacturing of cable peelings. As most specimens used in this work were below 0.3 mm in thickness, and were stored for 1-5 months the influence of byproducts in the electrical measurements should be insignificant.

4.1.5 FTIR-ATR measurements

The results of infrared spectroscopy investigations on the cut sample are shown in Figure 38 below.

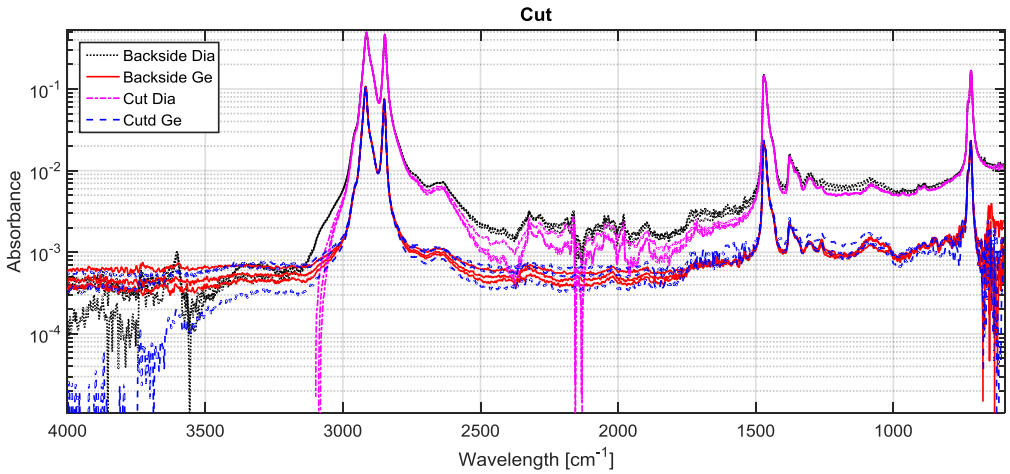

Figure 38. FTIR-ATR scan of a cut sample and its backside obtained with two different crystals.

The cut and backside surfaces show the typical spectrum for polyethylene and no significant changes can be noticed in the spectra, indicating that both the samples create chemically unchanged surfaces, with no significant signs of oxidation, introduction of foreign species or morphological changes. Next the abraded surface was tested, as shown in Figure 39.

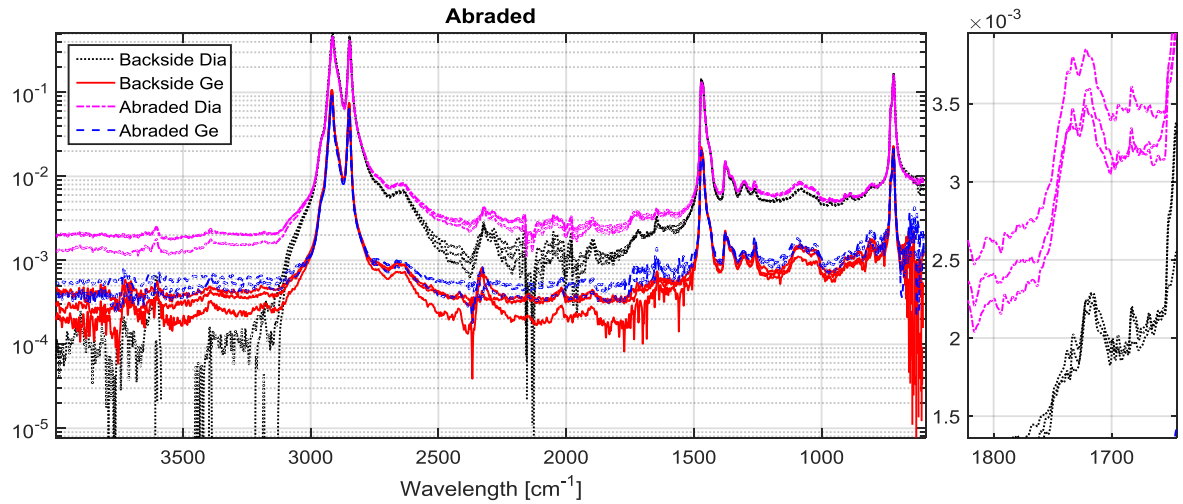

Figure 39. FTIR-ATR scan of an abraded sample and its backside obtained with two different crystals (left). Magnification of the 1700-1800 cm^{-1} wavelengths showing a small change in the spectrum between the samples (right).

Also here the abrasion does not introduce any significant changes in the spectra. Upon closer investigation however, a small broadening of the double peak at 1733-1755 cm^{-1} can be noticed, which could be indicative of a slight increase of C=0 bonds (carbonyl groups) on the surface of the abraded sample. This oxidation process could be related to heat development on the surface during the preparation. Next, the remolded surface was investigated with the results shown in Figure 40 below.

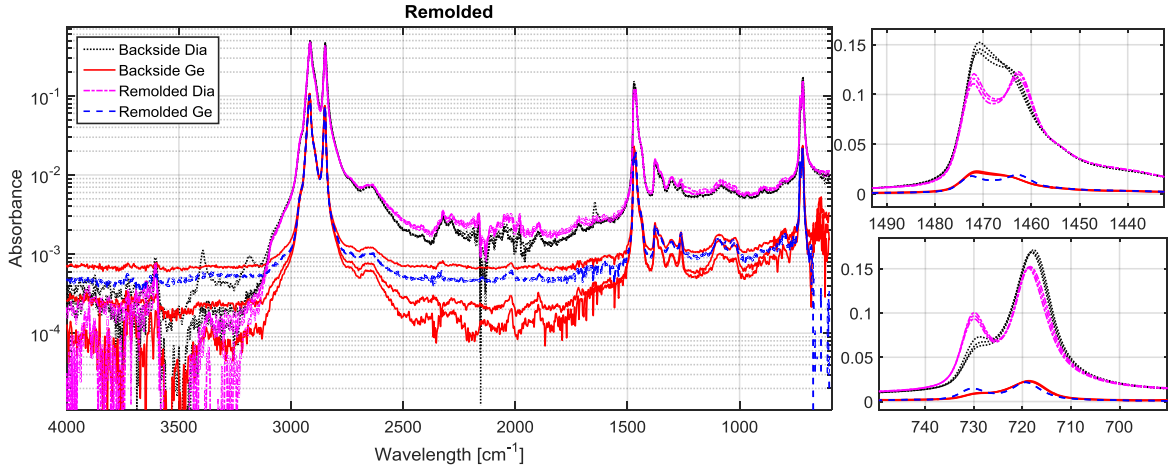

Figure 40. FTIR-ATR scan of a remolded sample and its backside obtained with two different crystals (left). Magnification of the 1440-1490 cm^{-1} and 700-740 cm^{-1}wavelengths showing a significant change indicating an impact on the degree of crystallinity.

The ATR scan in Figure 40 shows no signs of the introduction of foreign species, but there are changes in the shape of the peaks at 720-730 cm^{-1} and at 1460-1470 cm^{-1}. The development of these double-peaks shows a modification of the C-H stretch vibration, and the splitting of these two bands could be attributed to an increase in crystallinity and a higher degree of regularity of the backbone structure [72]. The development of these double-peaks are visible in both the germanium and diamond spectra, indicating that this morphological change is present at least in the outer micrometer thick layer of the sample. As the total sample thickness was around 0.5 mm, and the backside surface, as shown in Figure 40, remains unchanged, it is likely that the morphological change does not penetrate deep into the sample.

4.2 Electrical characterizations

In this section we introduce the electrical tests performed within the project, namely the DC breakdown tests and SPD measurements.

4.2.1 DC breakdown studies

This section introduces the results of investigations on the MV sized cable ends as well as the tests on cable peelings

4.2.1.1 MV-sized cables

The results of breakdown tests on MV cable ends prepared as illustrated in Figure 27 are shown in Figure 41 below.

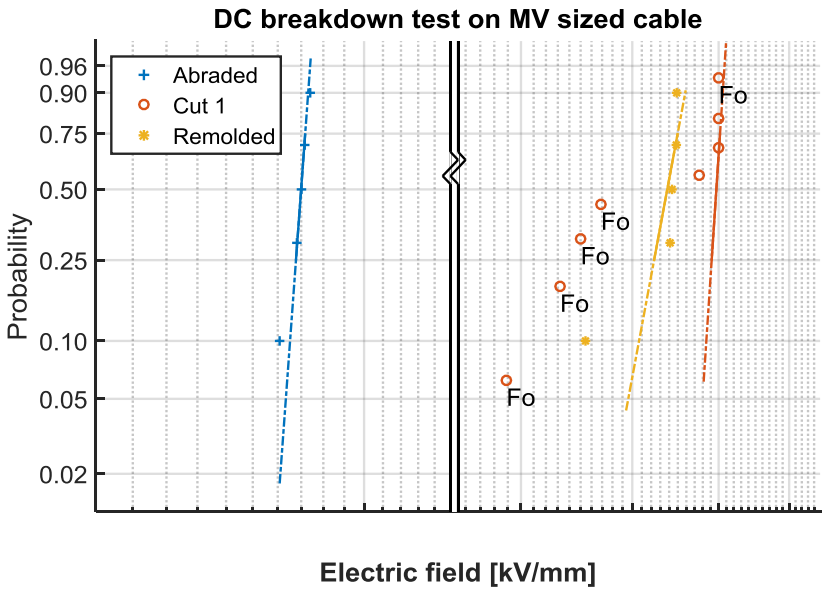

Figure 41. Weibull plot of DC breakdown test. Flashovers are indicated as "Fo" and are censored in the analyses.

No significant differences in insulation thickness at the breakdown positions were noticed. As the shape parameters of the Weibull distributions presented in Figure 41 are low, the results indicate that the surface preparation method resulted in a repeatable breakdown phenomenon. The abraded surface triggered breakdowns at significantly lower electric field level, slightly above the onset of space charge injection into DC cables [73]. The cables with surfaces of lower roughness broke down at significantly higher fields, which also resulted in a different shape of the breakdown channels as shown in Figure 42. One additional observation is that if the breakdown trend is fully linked to the roughness of the prepared cable surface, as shown in Figure 32, then the breakdown strength of the remolded surface should have become higher than the breakdown strength of the cut surface, which is not the case.

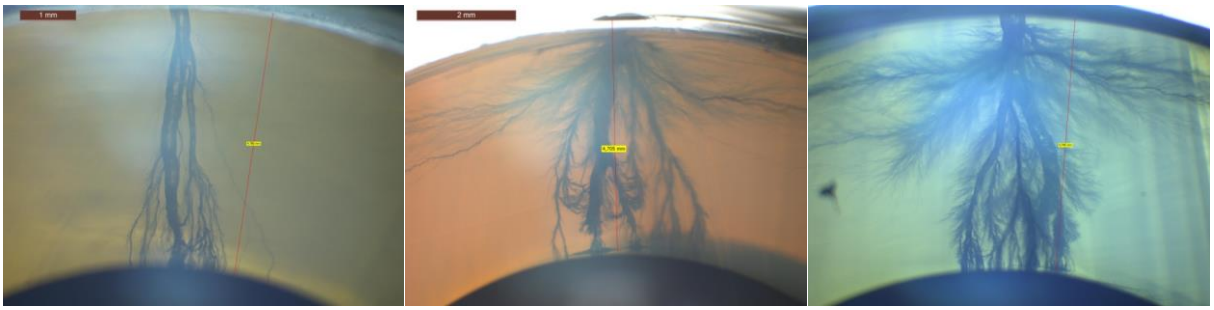

Figure 42. Breakdown channels of cable ends with abraded (left), remolded (middle) and cut (right) surfaces.

For the abraded surface, breaking down at relatively low electric field, the breakdown channel propagates from the outer surface towards the inner semiconductive layer of the cable. Some channels close to the inner semiconductive layer show inward bending towards the main channel for all the surface types, which is indicative of that tree propagation occurred prior to the feedback and streamer development in the main breakdown channel. For the remolded and cut surfaces, in addition to the main breakdown channel, also tangential and axial channels were found propagating in a layer 0.2-0.5 mm below the surface of the cable. In addition to the shape observation, also the location of the breakdown seems to be influenced. For the abraded surface the breakdown occurs statistically within a few mm from the SC break, while for the other surfaces, the distance between the breakdown channel and SC break has significantly greater variation. When the breakdown channels for cut and remolded surfaces were observed from above, the tangential and axial channels show a star-like shape centered on the main channel, as shown in Figure 43 below.

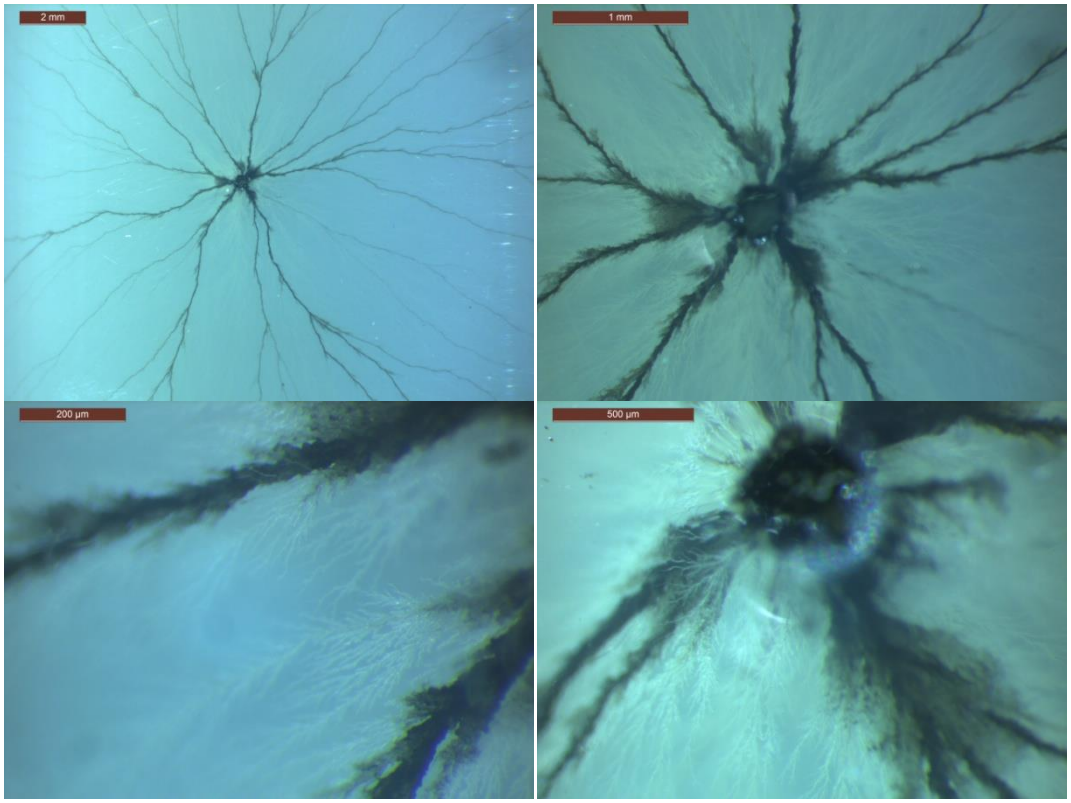

Figure 43. Breakdown channels viewed from above for a breakdown on a remolded cable end at different magnifications.

The star-shaped breakdown channel observed in Figure 43 has black carbonized deposit in the bigger channels, but also smaller whitish discharge traces, lacking the carbon deposits, can be detected in between these branches. The smaller white channels are not visible in Figure 42 due to the refraction of the light when looking through a thicker specimen. The star-shaped breakdown channels are indicative of a highly stressed material, with an additional driving force for channel propagation in a cylindrical shell towards the main channel. The origin of this driving force could be a significant space-charge build up in this layer.

4.2.1.2 Cable peelings

Initial tests, when using the test setup with guard ring, showed appearance of flash-overs at a voltage level of around -45 kV independent of the surface type. This corresponded to a tangential field strength of around 4.5 kV/mm, which was far lower than the breakdown strength of the oil. It is known that at interfaces strength is weakened, but such low values were not anticipated. After a removal of the guard ring, the problem did not occur. Breakdown channels and sample edges located more than 20-30 mm away from the test area, did not trigger any flashovers and seemed to have had little to no statistical impact on the breakdown levels. This could be indicative of space-charge buildup in the system, with the ability to shield off geometric defects for tests without guard ring. The adopted leakage current measurement system was unable to detect any current during the test, as the noise level was too high. The system did however work well for triggering an automated shutdown of the applied voltage when flashovers or breakdowns occurred in the test cell.

The results of the breakdown test on cable peelings are shown in the 2-parameter Weibull plot in Figure 44.

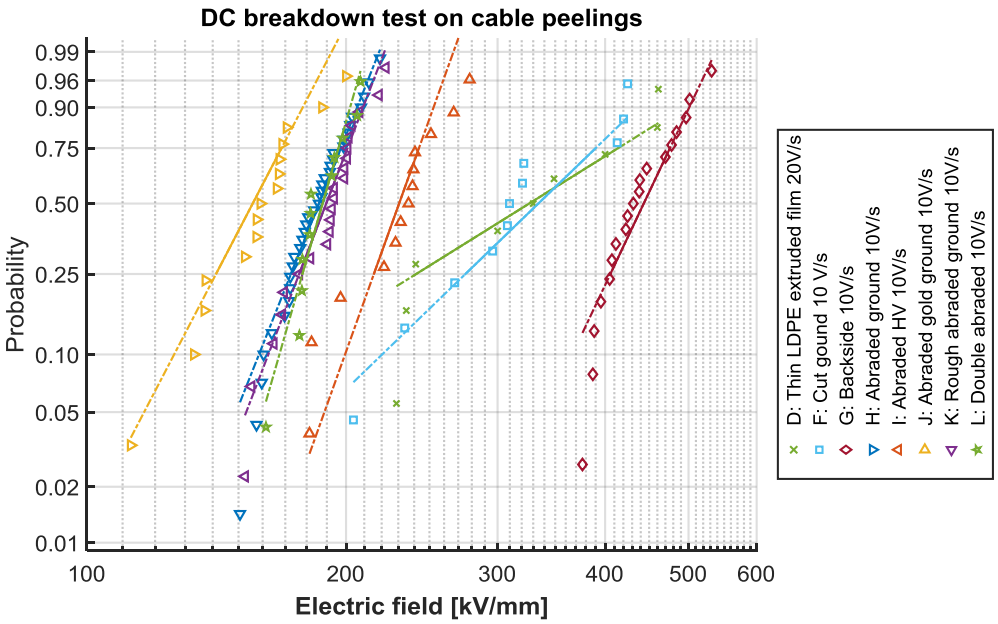

Figure 44. Weibull plot of the DC breakdown test performed on cable peelings at room temperature and negative polarity. Any flashovers or withstands are excluded from the statistics

The Weibull plot shows a significant impact on breakdown level depending on surface and sample type. The same trends between the different surfaces observed on the MV cable are also present in the cable peeling tests. There is also a scaling effect between the average breakdown field when comparing the peeling tests to the MV cable tests, and the geometric scaling is known to affect space charge properties due to different bulk to surface ratios. To make the

right conclusions from the Weibull plot, the thickness variation in the samples must also be accounted for, as shown in Figure 45 below.

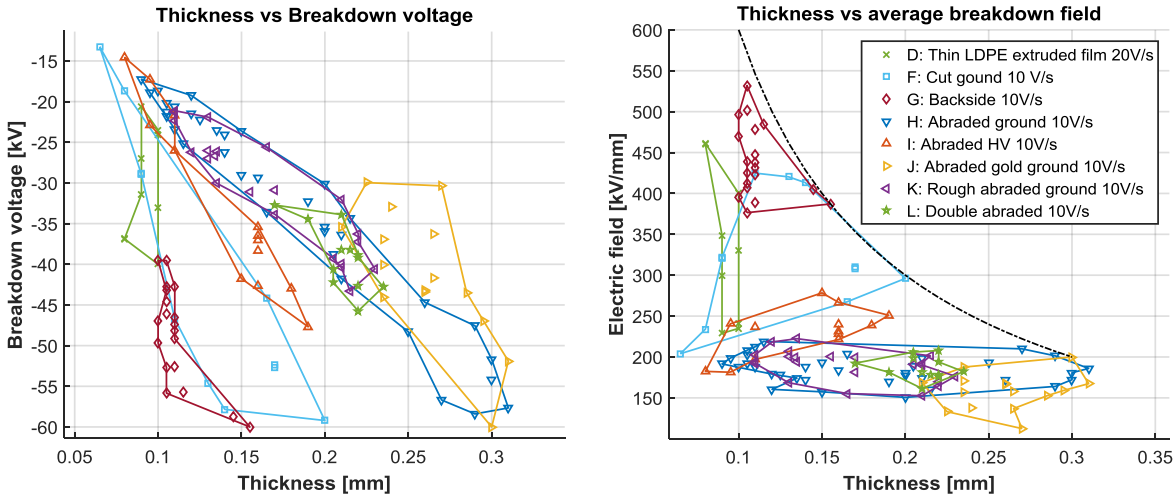

Figure 45. Impact of specimen thickness at the breakdown location on breakdown voltage (left) and breakdown field (right). The black dashed line in the right figure indicates the limit of the voltage source of -60 kV.

The results presented in Figure 44 and Figure 45 show that the backside sample (series G) can be used as the reference, as it has low surface roughness and low thickness variations within the sample, and the breakdown level is comparable to plate tests on this material [74]. The LDPE film (series D), suffered from a high shape parameter even though the sample had low thickness variations, which could indicate that there were imperfections present in this film. The Cut samples (series F) on the other hand, did have significant variations in thickness in the sample, which explains the high shape parameter in the Weibull distribution to some degree, as some of thinnest sections of these peelings could have been influenced by the pressure from the bearing ball.

All abraded surfaces (series H, I, J, K and L) also show significant thickness variations in the peelings, but this was done on purpose by selecting peelings of different thicknesses, as the breakdown field level showed repeatable and a low shape parameter in the Weibull plot in Figure 44. This purposely chosen variation of sample thickness was only possible for the abraded samples, as the breakdown level was low enough to test slightly thicker samples without reaching the limit of the voltage source (shown with dashed curve in Figure 45). For the abraded surfaces, the following observations can be made:

- Having the abraded surface towards ground (series H) gave an average breakdown stress level E_c of around 205 kV/mm. There is no impact of sample thickness within the samples indicating that an injection limited phenomenon is involved [49].
- Flipping the abraded surface towards the HV electrode (series I) increased the breakdown level, and a slight dependency on sample thickness was observed.
- Sputtering the abraded surface with gold (series J) lowered the breakdown level. (thin samples were not available).
- The rough abraded surface (series K) showed identical breakdown level to the abraded surface.
- Abrading both sides of the sample (series L) did not affect the BD voltage significantly. More flashovers were observed in this test series.

Besides the observations of breakdown level, also some trends were observed in the location of the breakdown channel, as summarized in Table 6 below.

Table 6. Amount of failures occurring away from the ball bearing electrode.

Test series	F: Cut	G: Backside	H: Abraded ground	I: Abraded HV	J: Abraded gold ground	K: Rough abraded ground	L: Double abraded
% away from ball electrode	25	36.4	100	85.7	100	100	100

All failures observed on abraded surfaces turned towards the ground electrode, occurred away from the HV electrode. This result was obtained through both subsequent voltage application after the breakdown and by observing the breakdown location in a microscope after the test. To check if the observed effect was related to the sample surface or the sample dimensions, the distance between the bearing ball (taken its central axis) and the breakdown location was analyzed, as shown in Figure 46.

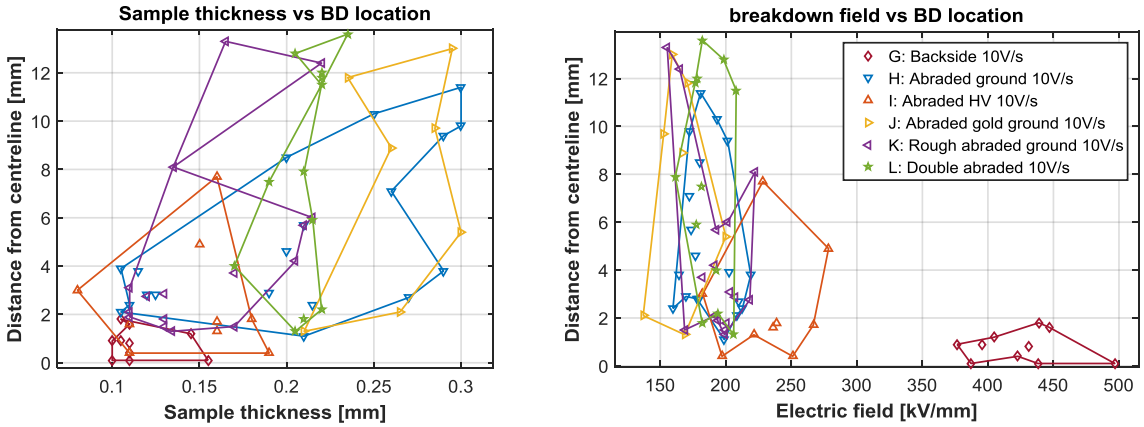

Figure 46. Position dependency of observed breakdowns showing sample thickness versus breakdown position (left), and electric breakdown field versus breakdown position (right). The method used for obtaining the breakdown position is shown in Figure 47.

As it was not possible to find the imprint from the HV electrode for each test, the statistics shown in Figure 46 are limited. All results closer than 1 mm from the central axis of the electrode were defined as being below the bearing ball. The top left picture in Figure 47 also shows that the surface texture remained underneath the bearing ball, and since the breakdowns are located further away as the radius of the imprint, it can be concluded that this effect is not related to local deformation underneath the bearing ball electrode. The results also show that failures occurring away from the HV electrode had no significant correlation against sample thickness. Also, no indications were found that the breakdown occurred at the thinnest point in the peeling. The upper limit to the spreading seems to show a slight relation against electric field, in that breakdowns at higher electric field show less spread over the surface. This could to some degree be related to field dependent bulk conduction processes. When the electric field in the sample is high enough, the conductivity could be in the same range as the oil conductivity, after which the spreading effect is limited as the field will not spread out through the sample anymore. These trends in failure position were therefore anticipated to some degree by the calculations performed in section 5.1, but the polarization properties calculated there do not predict the repeatable failure away from the bearing ball for abraded ground samples. Compared to the breakdown position trends observed on MV sized cables, the spreading effect observed

here seems to be the opposite, with the abraded surface causing a repeatable breakdown further away from the ball electrode compared to a repeatable breakdown within a few mm from the semiconductor end. The origin of this effect is further reflected upon in section 6.3. Next some of the found BD channels are shown in Figure 47 below to investigate if any additional observations can be made.

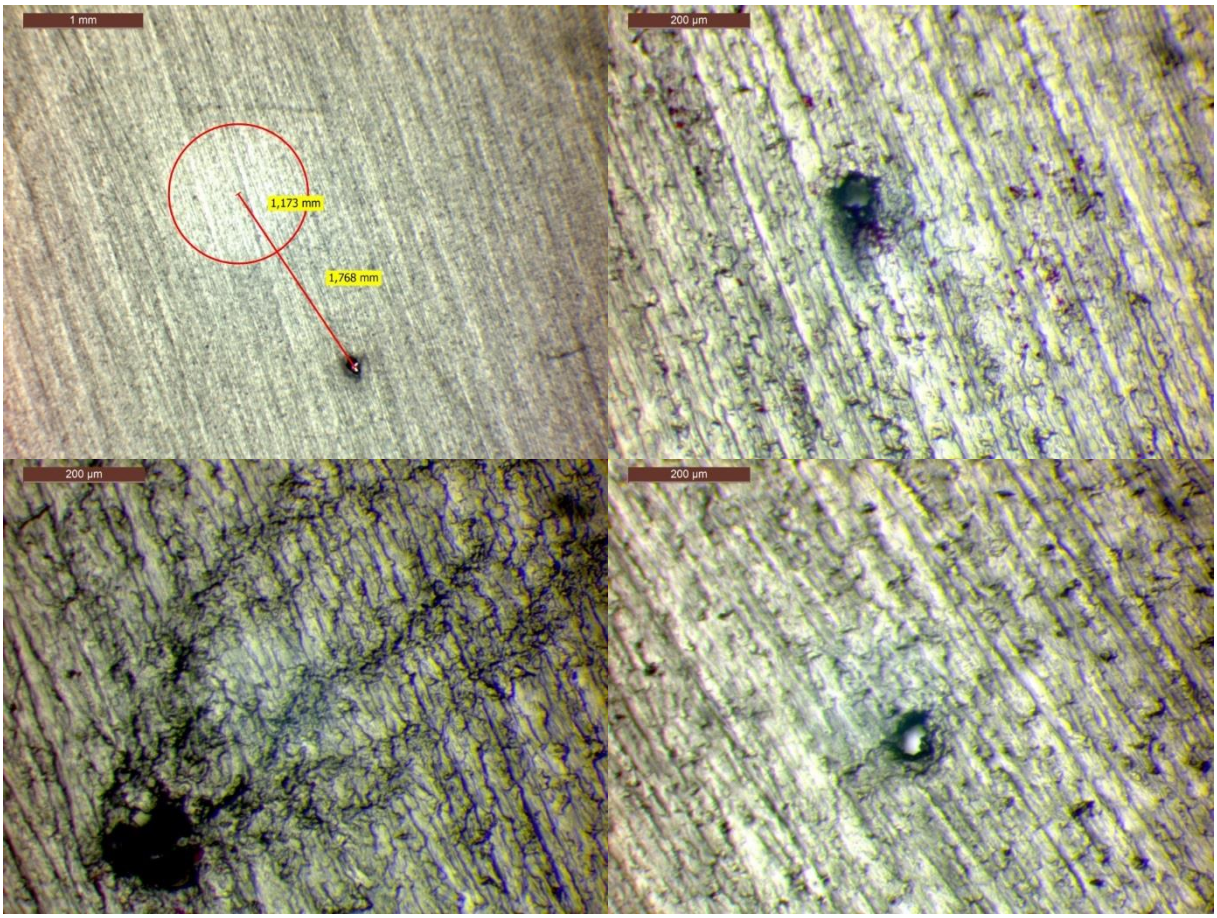

Figure 47. BD analysis of the DCBD test. Estimation of the distance to the BD channel (top left), Abraded breakdown channels (top right and bottom right) and abraded BD channel showing FO tracks towards the HV electrode (bottom left).

As shown in Figure 47, it was not possible to determine if the breakdown channel occurred on any specific feature of the surface texture, as these channels were around 50 µm in diameter which is larger than the features themselves.

4.2.2 Surface charge decay measurement

As using the ground electrode for measurement of the surface properties in the SPD measurement was counterintuitive, many tests were performed prior to discovering this possibility. For this reason, there is a significant amount of results for samples with the tested surface towards the needle and voltage probe, as well as results where the tested surfaces were oriented towards the ground surface (referred to as upside down). The obtained line scans for an abraded surface with thickness of 0.1 – 0.2 mm in the measurement area are shown in Figure 48.

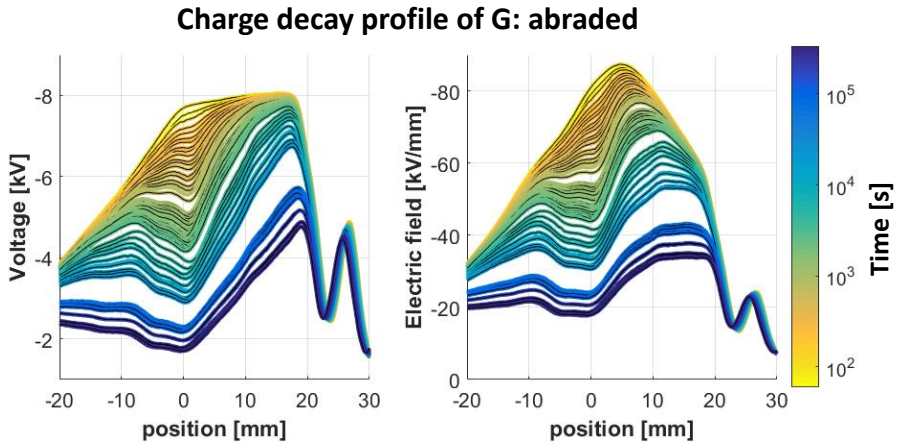

Figure 48. Charge decay profile of sample G, with the abraded surface towards needle and voltage probe.

The figure shows variations in the voltage and field profiles which originated from non-uniform thickness of the sample. The profiles indicate negligible or no surface conduction, which would have resulted in a widening of the initial profiles. As thickness correction was necessary, and the produced cable peelings also had a wide variation of average thickness, this was used as an advantage by purposely choosing samples of different thicknesses within a test series to investigate the conductive properties over a wide area of applied poling fields. When investigating these properties, it is important to consider that the measured surface potential relates to the total net quantity of charge in the sample, but since both negative and positive charge carriers can be present in the sample, two samples can show the same surface potential despite having different charge distributions. The field decay at the center point, as well as calculated conductivity and current density are shown in Figure 49 below for -5kV of the charging voltage.

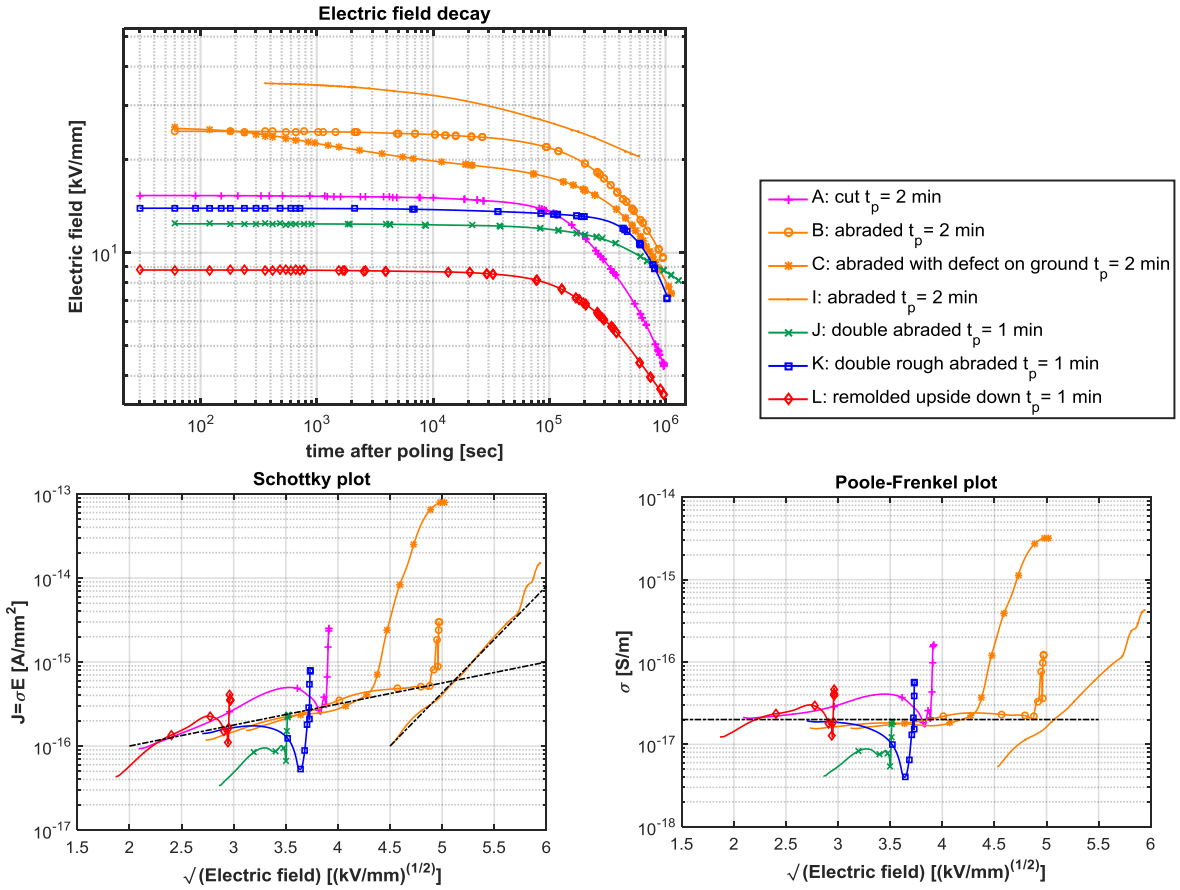

Figure 49. Obtained decay characteristics for the SPD measurement with -5kV poling for 1 and 2 minutes.

A shown in the Schottky and Poole-Frenkel plot al samples have a higher decay rate for the first few hours ($t<10^4$ sec) after which the decay rate decreases and follow mostly the dashed trendline, as the decay occurs from the right to the left in the figures. This initial decay process was observed in all measurements and is believed to be caused by an initial stabilization of the space charge profile in the sample. As any observations made during the stabilization time could be very sensitive to the many test parameters, this section of the decay process is indicative only. The consistency of the stabilization time is related to the relatively long charging time of 1 or 2 minutes used in the tests. The samples in Figure 49 also show a difference in decay rate between 1 and 2 minutes of poling time, which could be related to the different quantity and distribution of the initial negative charge from the needle and positive charge from the ground electrode accumulated in the bulk of the insulator during the charging process [37]. Sample C showed a longer and more significant stabilization, which could relate to a stop in the peeling, which created a significant defect line in the ground electrode of this sample. Samples J and K had abraded surfaces on both sides, and did not show any impact on the decay. Sample I showed a faster decay indicating a threshold in the Schottky and Poole-Frenkel plot at around 25 kV/mm, which likely corresponds to the transition between the ohmic and the field-dependent region. The results for -10 kV charging voltage with 2 minutes of charging duration are shown in Figure 50.

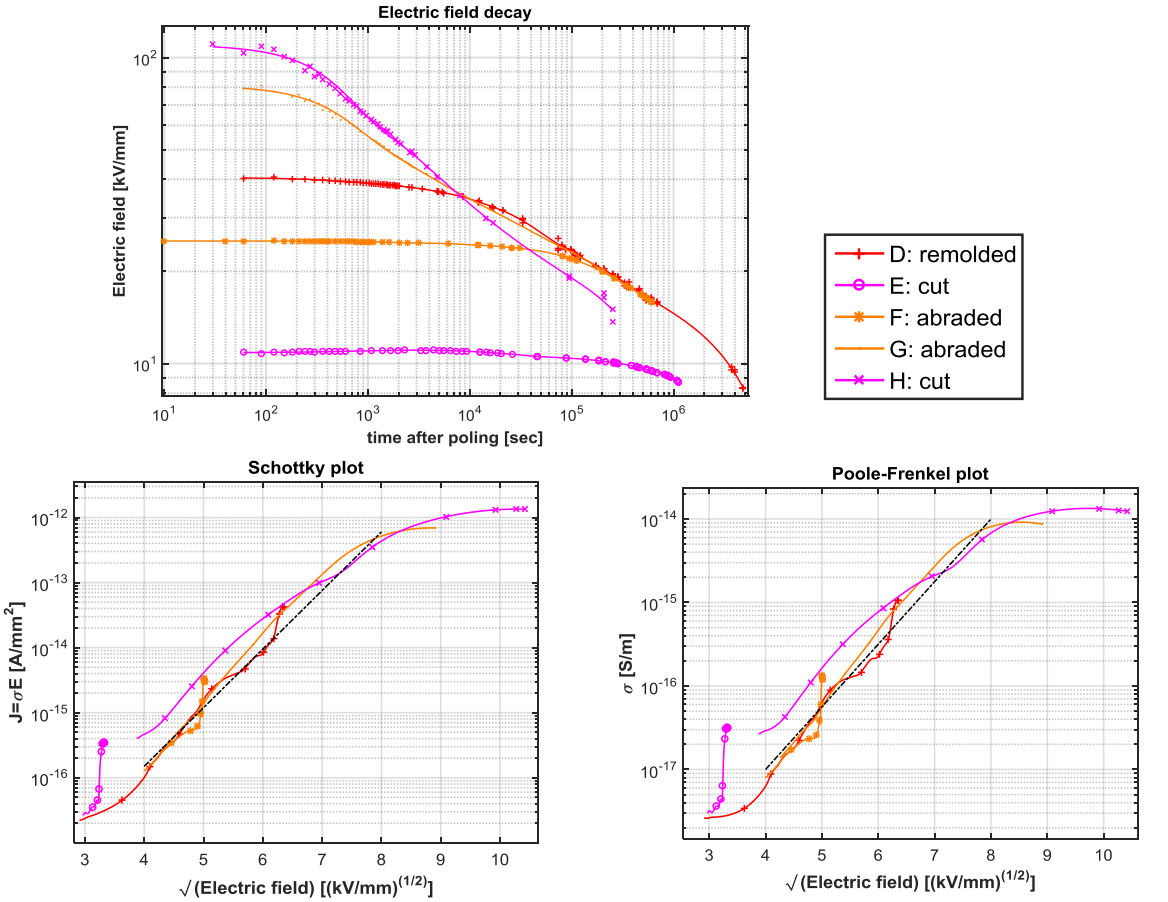

Figure 50. Obtained decay characteristics for the SPD measurement with -10kV poling for 2 minutes with surface type towards the needle and voltage probe.

As shown in the figure, most of the results were in the field-dependent region as thinner samples had been used. A crossover is observed in the field decay figure, which is an effect created by the non-linear dependency of conductivity. The results obtained at electric fields above 50 kV/mm (beyond 7 $(kV/mm)^{1/2}$ in the Schottky plot) are less stable and sensitive to the test conditions. Therefore, it is not practical to investigate any effects that occur above this level, such as the roughness assisted injection effects for smoother samples. No impact on the conductive properties was observed in the abraded samples F and G, indicating that any change in injection properties is not measurable with this configuration. Sample H was 0.8 mm thick, which is a lot thicker than all other tested samples and showed an initial increase in surface potential during the first few hours. Its decay current did also not match the ohmic region visible in Figure 49. The results for -10kV charging for 1 minute are shown in Figure 51.

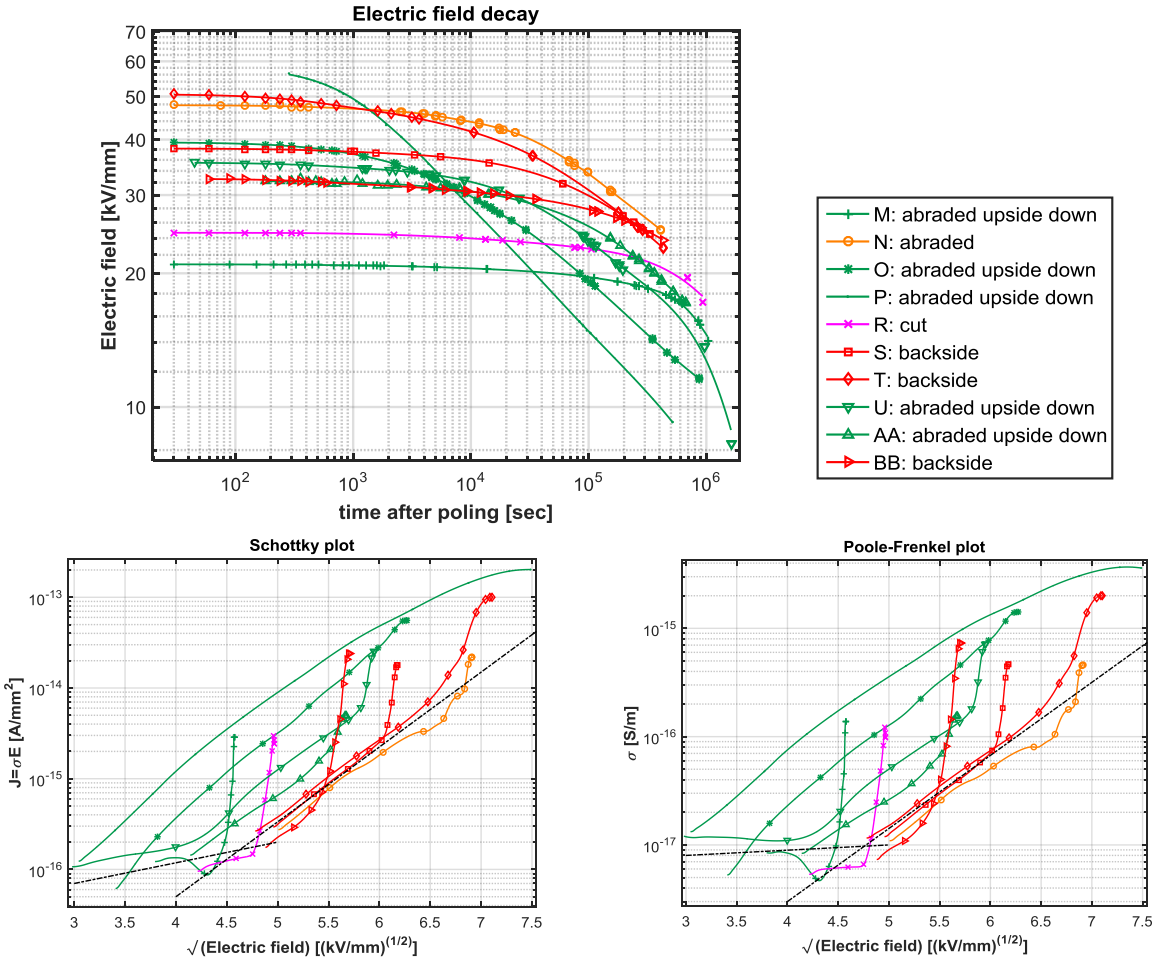

Figure 51. Obtained decay characteristics for the SPD measurement with -10kV poling for 1 minutes with surface type towards the ground electrode.

The figure shows a field-dependent region and an ohmic region indicated with dashed curves with a similar transition field as observed in Figure 49. The cut and backside samples (samples R, S, T and BB) can be treated as the reference as these surfaces were considered as ideal with regards to surface roughness. Crossover is again found in the electric field curves for these surfaces indicating presence of charge injection and field dependent conduction effects. The decay rate is lower than that observed for 2 minutes poling time, which is related to a different initial charge distribution [37]. The abraded surface (sample N) shows a small trend towards slower decay, which could indicate that the initial charge layer spans over a wider thickness δ or a higher density of deep traps on this surface. However this effect is inconsistent with the previous observations in this section. The most significant observations are seen in the abraded ground curves (samples M, O, P, U and AA), which show faster decay rates and an earlier field crossover. This is indicative of possible charge injection from the ground electrode [69]. Increased decay rate is not noticed at 21 kV/mm (sample P), meaning that the injection process has a field threshold in the region of 21-35 kV/mm. As various conduction modes are involved here in the decay process, it is not possible to assume any dominating mechanism apart from the level of field threshold. It is also not possible to determine if the charge injection process from the ground electrode is of Schottky or Fowler-Nordheim type. To investigate the impact of roughness magnitude, rough abraded and roughest abraded samples were tested in the same test configuration and the results are shown in Figure 52.

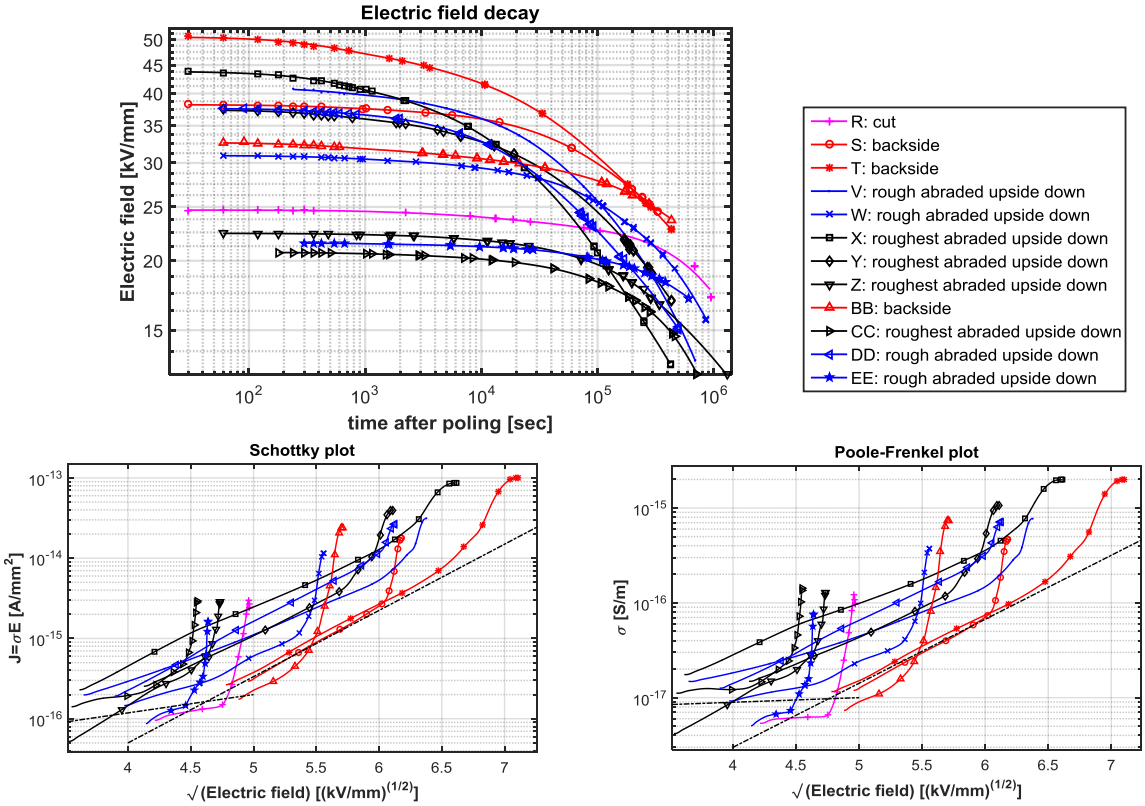

Figure 52. Obtained decay characteristics for the SPD measurement with -10kV poling for 1 minutes with surface type towards the ground electrode.

The rough and roughest abraded surfaces shown in the figure had an increased decay rate, similar to the abraded surface, and showed crossover in the electric field curves. The rough abraded surface behaved nearly identical as the abraded one. The surface potential on sample DD decayed faster than on sample V, which may be caused by a shift in the needle-sample spacing in the setup. The roughest abraded samples show a low threshold, below 20 kV/mm, but the increase in current density over the reference (samples R, S, T and BB) is noticed first above a field level of 30 kV/mm. This could be caused by the impact of field dependent bulk conductivity on the local field distribution towards the surface. When increasing the poling field from 20 to 35 kV/mm, the tail in the local FEF distribution is lowered while the overall field is increased. This effect keeps the increase in decay rate limited at intermediate fields. At high field, the reduction in the tail of the FEF distribution was no longer significant, as shown in Figure 65, allowing for the decay rate to increase significantly.

To compare all results from Figure 51 and Figure 52 in the region after stabilization, the calculated decay current at 10^4 seconds after poling is plotted against the initial poling field in Figure 53.

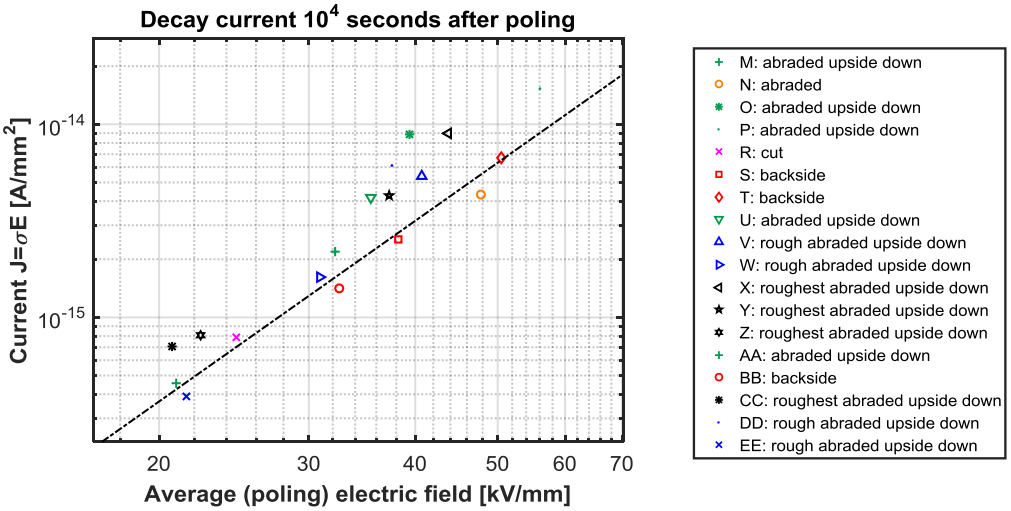

Figure 53. Estimated conductivity after approximately 3 hours, versus poling field.

The difference between the abraded-ground and the smooth-ground samples shown in Figure 53 is smaller than the differences in the Schottky and Poole-Frenkel plots, because the conductivity is plotted here against the initial poling field in the sample, and not the estimated electric field after the stabilization period. As the time it takes for a somewhat stable charge distribution is shorter the more charge is present in the sample, taking the exact same time for each measurement makes the observed differences a bit less pronounced. The results in this section allowed for an estimation of the threshold field, E_{th} for the rough-ground samples, which could be estimated to be as follows:

- Abraded: $21 < E_{th} < 32$ kV/mm, likely around 30 kV/mm
- Rough abraded $21.5 < E_{th} < 31$ kV/mm, likely around 29 kV/mm
- Roughest abraded $E_{th} < 21$ kV/mm

Chapter 5

Simulation and Calculation

This chapter summarizes the simulations and calculations performed within the thesis work. At first, specific calculations were made that aim at defining test parameters and assessing the electric field distribution in the DC breakdown tests. Next, the previously obtained roughness data was used to calculate their hypothetical influence on space charge injection into the insulation material. At last, the distribution of field enhancement factors (FEF) for a localized defect was analyzed.

5.1 Estimation of polarization properties in DC breakdown experiments

The time dependent MWS interfacial polarization properties were calculated for an oil-XLPE interface, using equation (9) for stepwise voltage application and equation (11) for ramped voltage application. The used parameters are described below in Table 7.

Table 7. Used parameters for MWS calculation.

Parameter	Value for dielectric A	Parameter	Value for dielectric B
Relative permittivity	2.3	Relative permittivity	2.3
Thickness	0.1 mm	Thickness	0.1 mm
conductivity	1e-14 S/m	conductivity	1e-17 S/m
Voltage ramp speed	10 V/s		
Step voltage	100 V		

The conductivity value for dielectric A was chosen to be 1e-14 S/m, which is lower than oil conductivity, the latter to be in the range of 1e-12 S/m. This was done to ensure that a DC field distribution was stabilized, before breakdown occurred in the DC test. The extended MWS model as shown in Figure 6 introduces an interstitial material, as can happen in the DC test of a physical interface, the lowest possible conductivity was therefore taken for which a DC distribution could be reached within realistically obtainable test durations. The results of the calculations are shown in Figure 54.

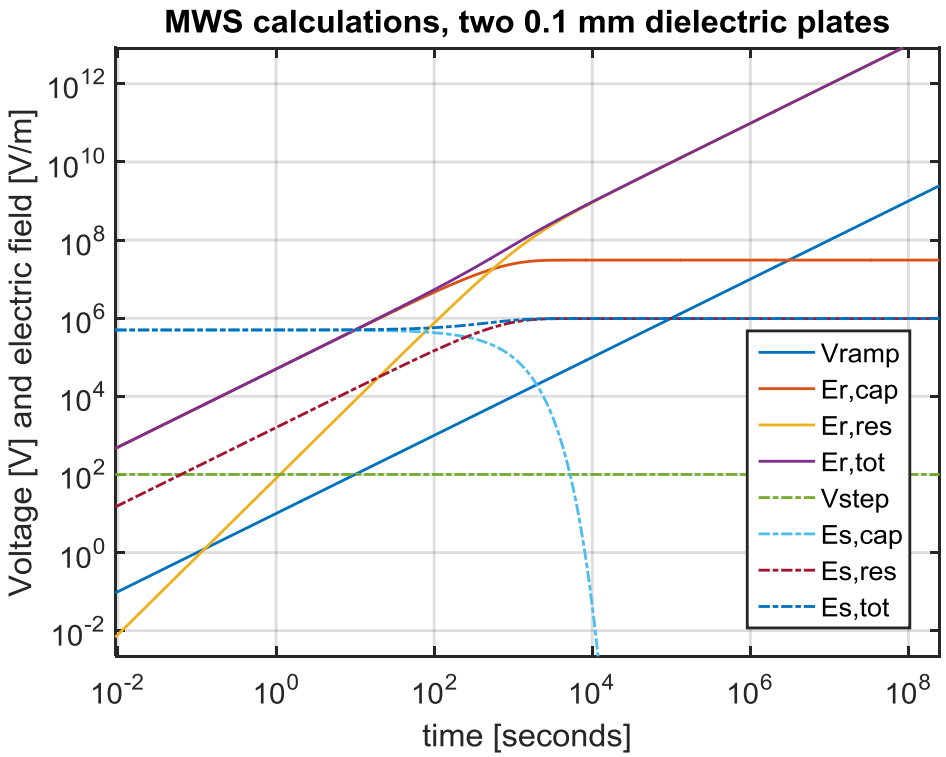

Figure 54. Calculation of electric field in dielectric B according to MWS interfacial polarization for ramped DC voltage from equation (11) (solid lines) and for stepped voltage from equation (9) (dashed lines). The figure includes the voltage, the capacitive (cap), the resistive (res) and the total electric field distribution for the two cases.

It is observed in Figure 54 that the shift to a DC field distribution occurs after one hour for a ramped DC voltage and 30 minutes for a stepped Voltage. The transition time is independent on the magnitude of the applied voltage step and independent on the ramping rate. In the calculation, the capacitive electric field in material B for ramped voltage becomes stagnant at around 100kV/mm (for a 0.1mm sample) while the resistive electric field continues to increase after one hour. The transition time is governed by the material parameters, and since $\sigma_a >> \sigma_b$, the shift-time is mostly dependent on the material with higher conductivity, σ_a. As the conductivity is temperature and field dependent, as expressed in equation (6), there could be a reduction of the transition time if this affects the conductivity in material A.

The ball bearing electrode shown in Figure 28 was also simulated in Comsol, using the electric current modulus and axial symmetry, for investigating the impact of the guard ring in the system and the field shift depending on sample conductivity. The results of the simulation are shown in Figure 55 for applying 100kV in the setup.

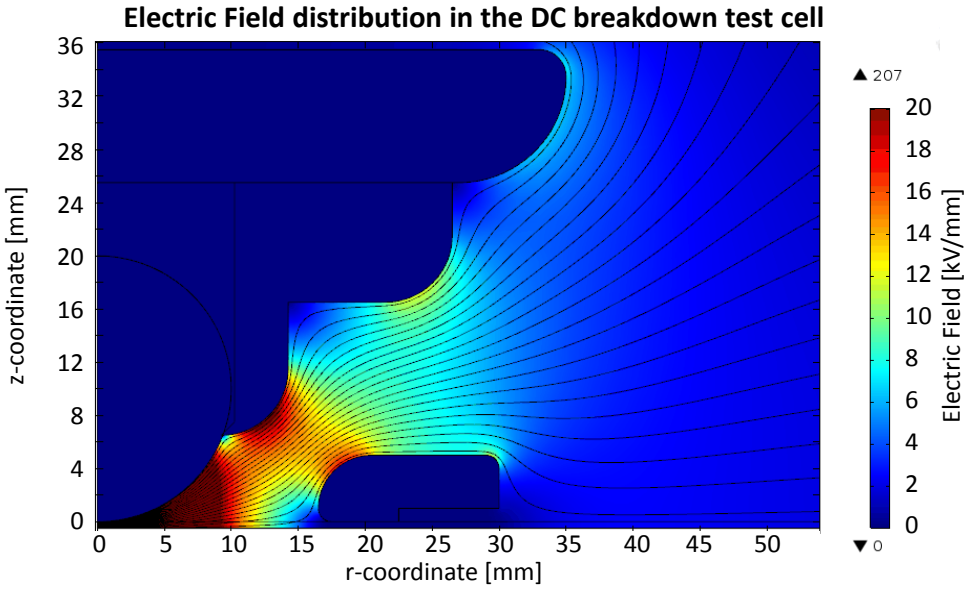

Figure 55. Electric field calculation for a 20mm ball bearing electrode and a 1mm sample. Oil conductivity is 1e-12 S/m and XLPE conductivity is 1e-12 S/m. Color indicates electric field in kV/mm and lines represent the equipotential lines.

As seen in Figure 55 the clamping ring creates a field enhancement in the oil, but still the maximal electric field is below 25kV/mm. When the material parameters are the same in the sample and the oil, the electric field is highest underneath the bearing ball. However, as the XLPE conductivity was anticipated to be significantly lower than the oil conductivity, another simulation was made as shown in Figure 56.

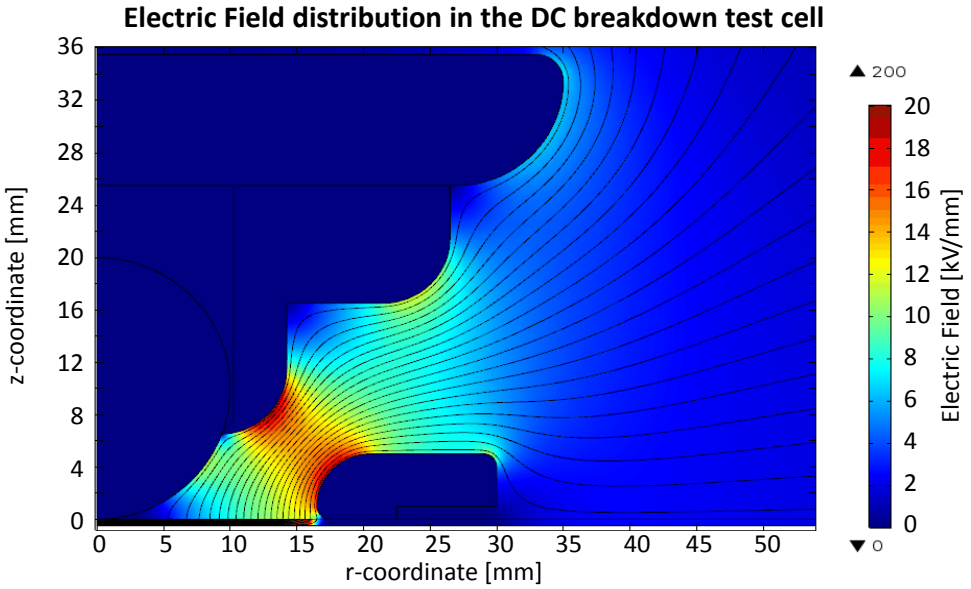

Figure 56. Electric field calculation of a 20mm ball bearing electrode and a 1mm sample. Oil conductivity is 1e-12 S/m and XLPE conductivity is 1e-17 S/m. Color indicates electric field in kV/mm and lines represent the equipotential lines.

The lowered conductivity results in the electric field spreading across a larger area of the sample and the guard ring protects the sample edge. It was thus initially anticipated that tests without guard ring would yield flashovers originating either from the sample edge, or from nearby located breakdown channels from prior tests.

Next the tangential electric field along the sample was simulated when the sample conductivity was changed from 1e-12 S/m to 1e-17 S/m as shown in Figure 57 below.

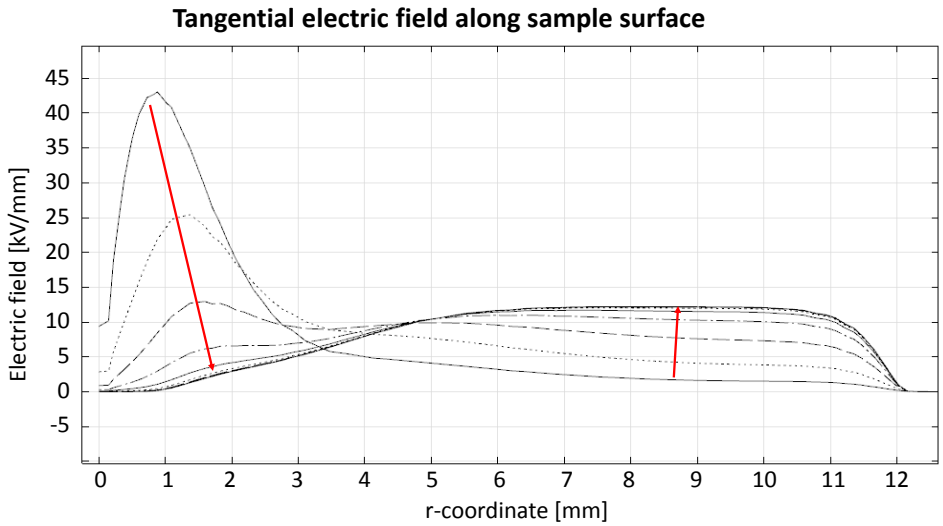

Figure 57. Tangential electric field in DC breakdown test with sample conductivity sweep from 1e-12 S/m to 1e-17 S/m. Arrows indicate effect of the lowering the sample conductivity. The guard ring is located at 12 mm.

The same phenomenon as observed when comparing the electric field distributions in Figure 55 and Figure 56 is seen in Figure 57, where the lowering of sample conductivity results in the electric field gradually spreading out along the sample. To see the effect of guard ring removal, the results of is shown in Figure 58 below.

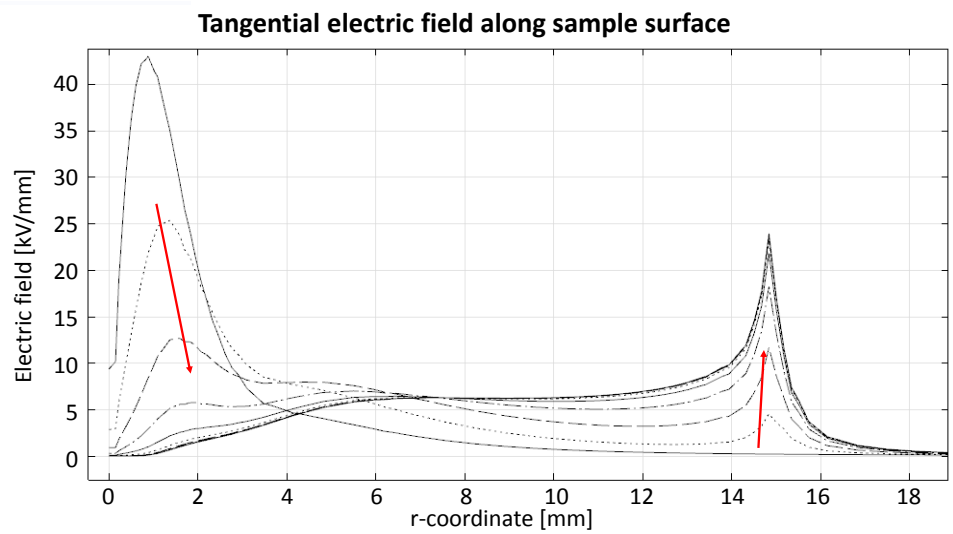

Figure 58. Tangential electric field in DC breakdown test with sample conductivity sweep from 1e-12 S/m to 1e-17 S/m. Arrows indicate effect of lowering the sample conductivity. The sample edge is located at 15mm.

Figure 58 shows the development of an increased electric field at the sample edge at 15 mm away from the bearing ball. The field dependency of the XLPE conductivity, as expressed by equation (6), could lead to a decrease of the field enhancement at the sample edge. The figures also show that the magnitude of the tangential field in the system can be to some degree proportional to the distance towards the sample edge, guard ring or nearby breakdown channels,

with the exception of the first four millimeters from the central axis, where the tangential electric field becomes lower due to the presence of the bearing ball.

5.2 Estimation of barrier properties

This section presents the calculation of field enhancement factors and their impact on space charge injection.

5.2.1 Calculation of field enhancement factors

For the calculation of field enhancement factors, the most generic results of surface roughness measurement, obtained by means of optical profilometry, were imported to Matlab. 50 by 50 pixel surface sections were selected and interpolated with a cubic spline to create a well meshed surface section for importing it into the FEM calculation. Performing this interpolation prior to importing it into the FEM software was preferred over increasing the meshing in the FEM software itself, as this eliminated sharp peaks within the raw data as much as possible. A result of such interpolation is shown in Figure 59.

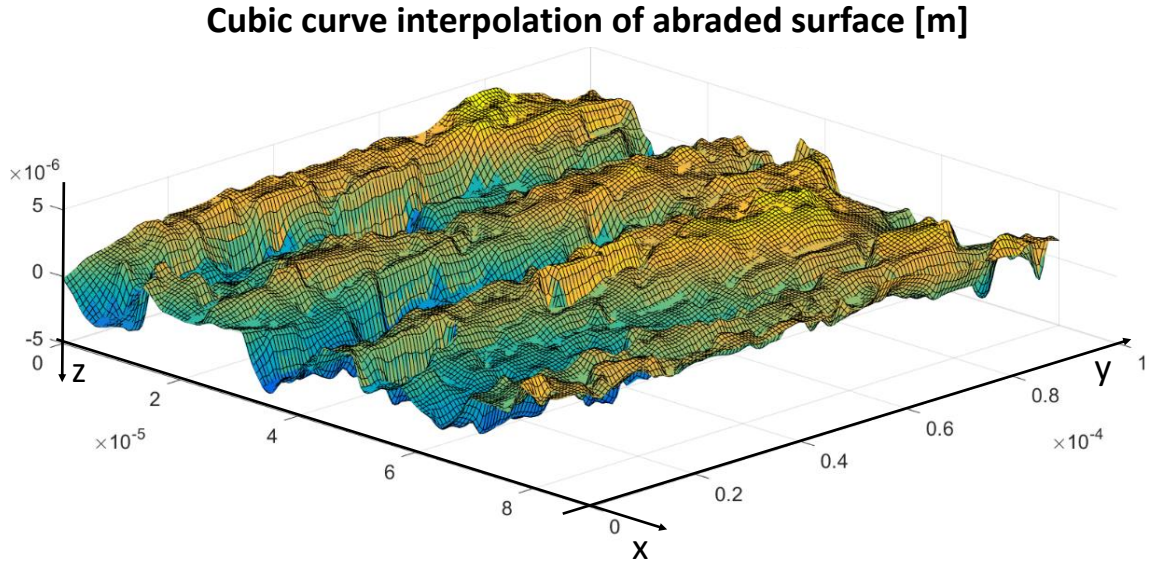

Figure 59. Coordinates of an interpolated section of the abraded surface.

As seen in the figure, the used interpolated surface has the dimensions 80 µm by 100 µm and it well presents the SEM image of the abraded surface shown previously in Figure 31. Histograms representing the statistical height distributions of the selected surfaces are shown in Figure 60.

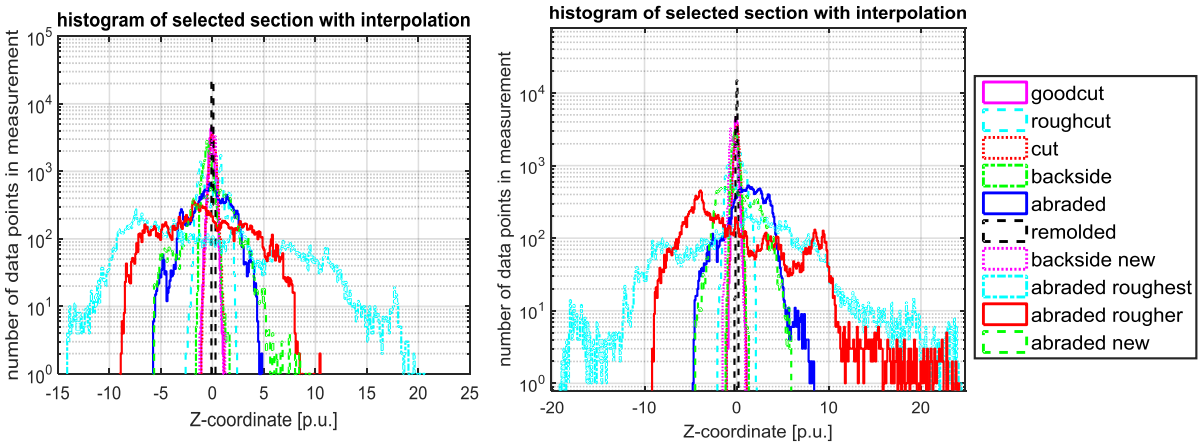

Figure 60. Histogram of the surface height for two sections taken at different positions on the measured surface. At least two calculations were made on each surface type as shown here in two separate histograms.

Most of the histograms shown in Figure 60, show consistent results when compared against the full surface shown in Figure 34. However, the two surfaces with highest roughness, i.e. rough abraded and roughest abraded, were not consistent as the size of the surface texture was approaching the size of the domain. As the domain size couldn't be increased any further due to memory limitations, the FEF distribution of the two roughest surface types were calculated four times each. Some additional surfaces were added, such as goodcut, and roughcut, which were surfaces in which the roughness parameter Sa was found respectively lower and higher as compared to the cut surface. A section of the roughly abraded surface after electric field calculation is shown in Figure 61 below.

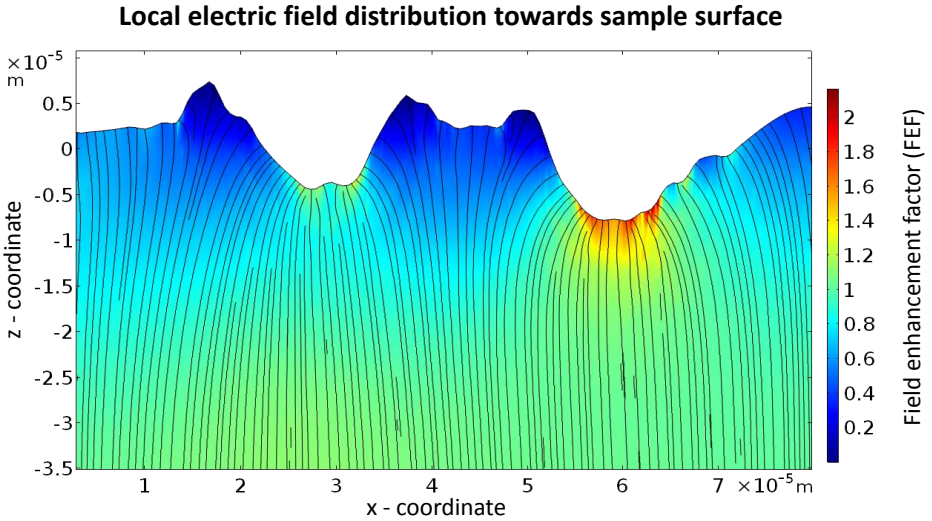

Figure 61. Surface field distribution of a roughly abraded surface. Only the section closest to the surface of the 100 μm Z-domain length is shown in the figure.

As anticipated and shown in Figure 61, the electric field strength is enhanced at the low points of the surface, while it becomes reduced at the high points of the surface. This behavior was observed for all of the measured surfaces, and resulted in the field distribution being dependent on both surface texture and roughness magnitude, as shown when observing the FEF against surface coordinates in Figure 62.

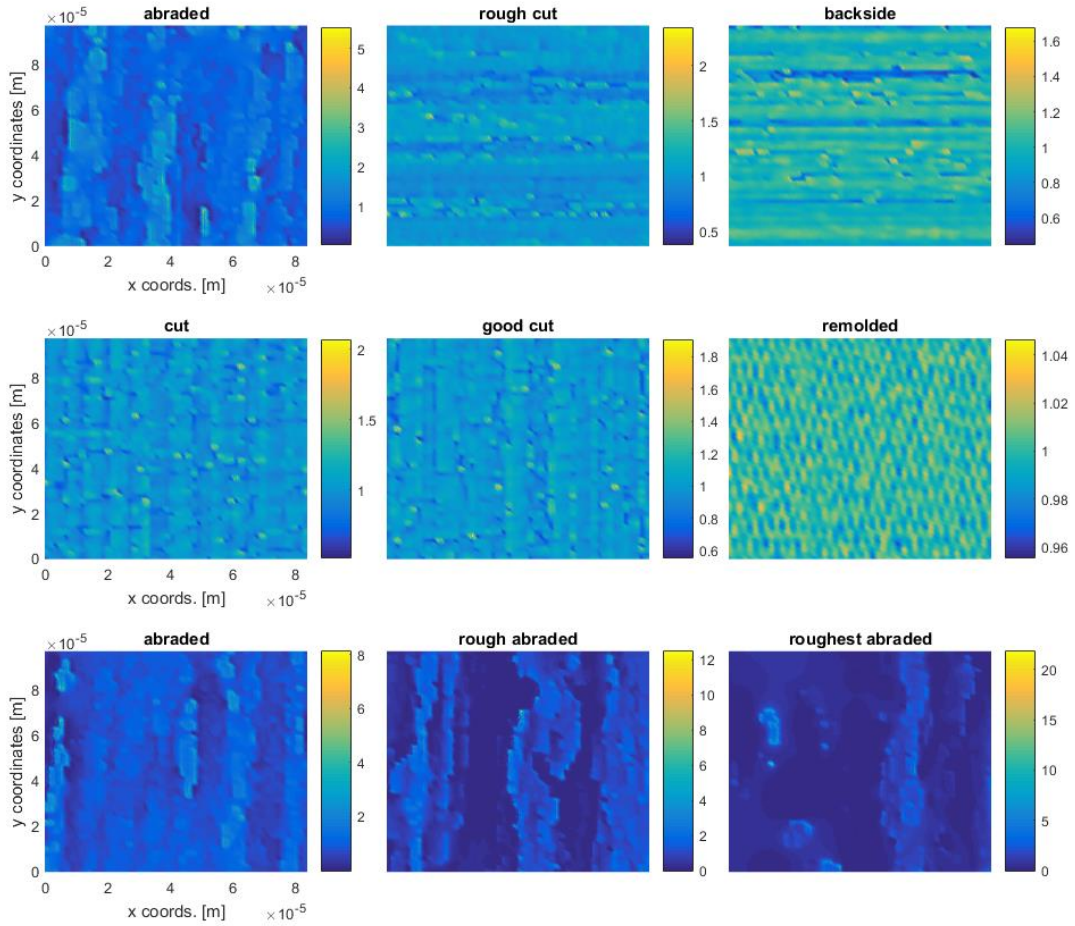

Figure 62. Texture and roughness magnitude dependency of FEF for various surface types.

The resolution of the surfaces shown in Figure 62 is around 1500 nm^2 for each point of the surface. The FEF distribution is to some degree influenced by the shape of the surface texture, as it is possible to observe parts of texture in the data, and some of the features are still comparable to the SEM observations shown in Figure 30. The texture observed on the remolded surface is originating from light interferometry pattern of the optical profilometry, and the FEFs obtained on this surface type are nearly representing an ideal surface. Varying the roughness of the cut surface had only little impact on the FEFs, while varying the roughness of the abraded surface showed a significant increase in FEF magnitude. The obtained data is comparable to the results obtained by Taleb et al [44]. Next, a histogram was calculated to investigate the FEF population of each surface as shown in Figure 63.

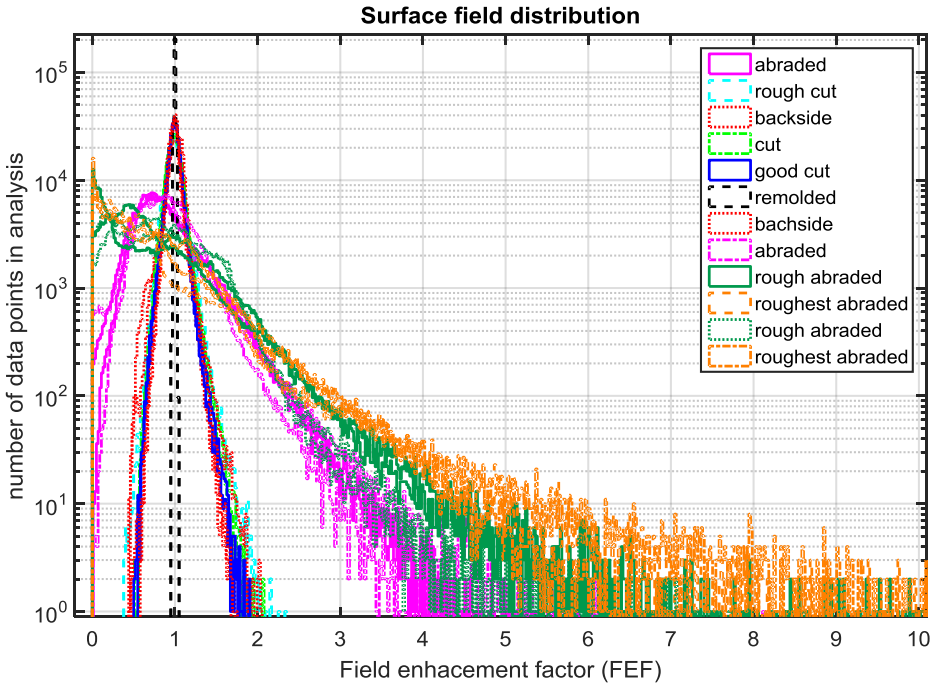

Figure 63. Histogram of the FEF population for each of the measured surfaces.

When investigating the histogram shown in Figure 63 and comparing it to the histogram of the surface roughness shown in Figure 34, it can be seen that the normal distribution of surface height develops a tail towards the right hand side in the FEF distribution, which can be fitted with a beta distribution. This fitting was not done however, as using the actual data for further calculation appeared to be more accurate. For assessing the position of tail, the averaged 100 highest points in the distribution, were plotted against the arithmetical mean height (Sa) for each of the surfaces, as shown in Figure 64.

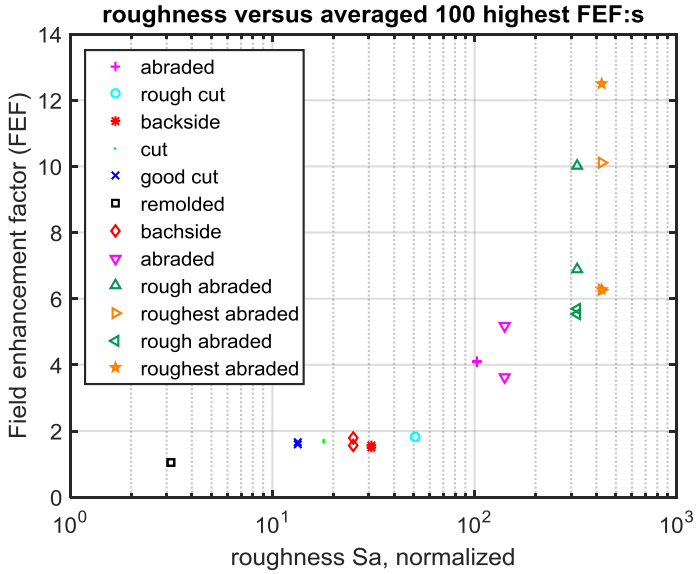

Figure 64. Logarithmic plot of the surface roughness parameters against the tail of the FEF distribution for each surface type.

Figure 64 clearly shows the correlation between the surface roughness and magnitude of the field enhancement, but its impact is also influenced by the sample type. As it is rather difficult

to fit the points in the figure with an analytical function, there seems to be a need for separate calculation for each surface type to account for the impact of the different texture types introduced by the preparation methods. As earlier illustrated in Figure 60, the high deviation of the two roughest surfaces depended on which part of the measured surface was chosen to create the section for the calculation, because of the texture size approaching the measurement domain.

As the calculations so far have excluded bulk conduction effects, additional calculations were also made including a field dependent bulk conductivity in the simulation. The field dependency, expressed by equation (6), makes the FEF dependent on electric field, requiring the calculation to be performed separately for different magnitudes of the applied electric field. The impact of on the FEF distribution of the abraded surface is shown in Figure 65.

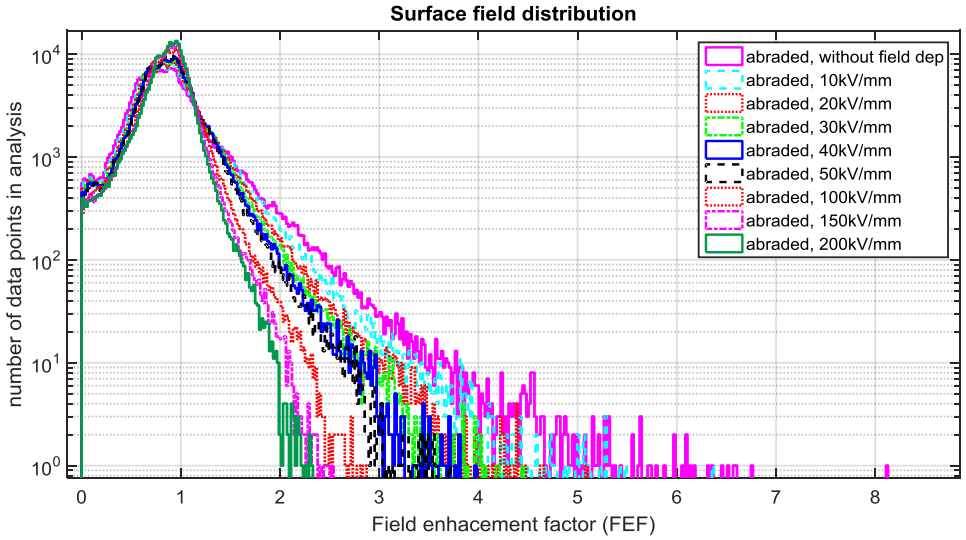

Figure 65. Surface field distribution of the abraded surface with field dependent conductivity at different levels of applied electric field.

Figure 65 shows that the FEF distribution becomes narrower when increasing the magnitude of the electric field, and the highest impact is seen in the tail of the distribution. This effect is explained by the exponential field dependency of the conductivity, which for higher levels of applied field, gives a steeper position on the conductivity curve. With the FEF introducing a spread in electric field at this position, this causes the high field simulation to give a bigger variation in conductivity than a simulation at low electric field. Figure 65 also shows that the tail of the distribution still remains, but is shifted to around 4 at around 30 kV/mm. Calculations performed at 100, 150 and 200 kV/mm show that the field distribution never disappears, even at extremely high electric fields (likely beyond the validity of equation (6)). Next the impact of field dependent conductivity was calculated for the rougher abraded surfaces, as shown in Figure 66.

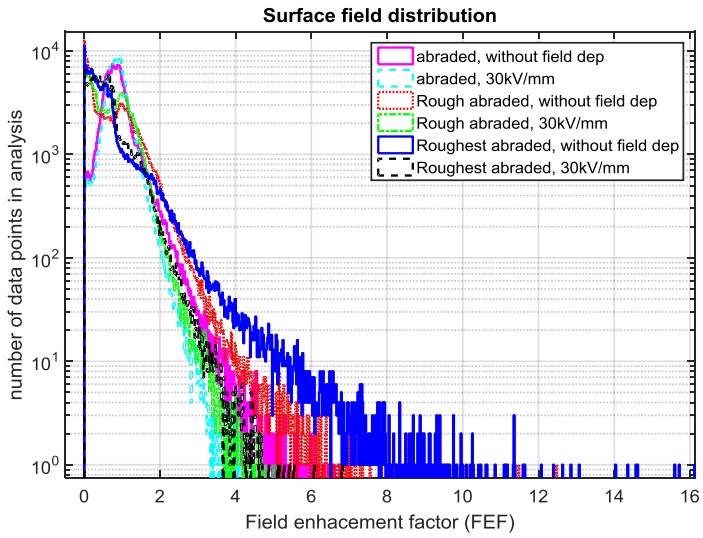

Figure 66. Surface field distribution with and without field dependent conductivity for the rougher abraded surfaces.

The narrowing in the FEF distribution is the greatest for the roughest surfaces and the distribution tail of all three abraded surface types is reduced to around 4 to 5. The field distribution's dependency on the roughness magnitude still remains, but it is significantly reduced by the field dependent conductivity.

5.2.2 Calculation of charge injection properties

For calculation of the charge injection properties of the surface under the impact of the previously estimated field enhancement factors, Schottky and Fowler-Nordheim equations were solved for each point on the surface, using the parameters listed in Table 8.

Table 8. Used parameters for injection calculation.

Parameter	Value	Parameter	Value
Richardson constant	1.2×10^6	Relative permittivity	2.3
Reflection coefficient	0.3	Barrier height	1.5 eV and 2 eV

As no detailed information is available concerning the bulk and surface trap distributions, these parameters where chosen to yield results comparable with those of the measurements. As many measurements had been carried out with the gold sputtered rough surface towards ground, and with the opposite electrode at negative polarity, the simulated barrier heights were chosen to be of similar magnitude. As gold is known to have a well-defined work function of around 5.1 eV, and with the valence band position of LDPE being somewhere in the range of 7 to 7.8 eV, this would create a barrier height for hole injection in the range of 1.9 to 2.7 eV. As mentioned in section 2.3.4.1, there could be some justification for using a lower barrier height to account for the effect of traps on the injection process, which is why around 1.2 eV is commonly used in simulations as Schottky barrier height for hole and electron injection [36][75].

The estimated surface distribution of field enhancement factors were taken without impact of field dependent bulk conductivity, as the use of field dependent FEF was not possible due to a lack in computational performance. Also, as the bulk conductivity parameters had been obtained from electrical tests, and comprise of injection properties, bulk properties and other space charge phenomena in these tests, it is not straight forward if such data can be accurately used in the microscopic charge injection behavior estimates.

For calculating the averaged injected Schottky current, equation (22) was used to calculate the current at each point on the surface, and then averaging it over the entire surface section was done by using equation (23). The results of the calculations are shown in Figure 67.

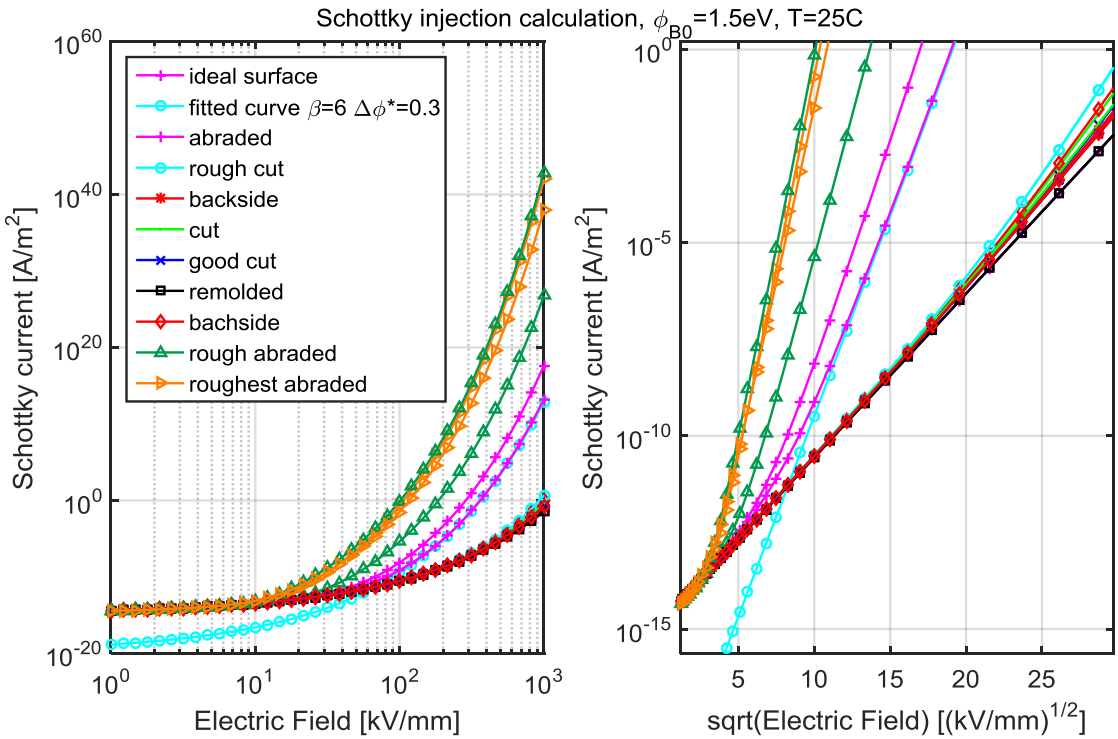

Figure 67. Schottky injection curves showing the impact of surface roughness in a logarithmic plot (left) and a Schottky plot (right)

A clear threshold effect is noticeable in the calculated current density for abraded surfaces, where little to no impact on charge injection is found below field levels of 10 kV/mm, and with the current density increasing significantly in the 10-100 kV/mm region. A curve fit was made for the high field region of the abraded surface, by increasing the barrier height to 1.8 eV and introducing a field parameter $\beta = 6$ in the exponent of equation (22). As such a fit is not able to estimate the current density in the low field region, it becomes evident that parameter modification or barrier height modification is unable to accurately explain the impact of local field enhancement on charge injection. The cut surfaces also show a threshold effect, but this effect is located at significantly higher field levels and is more difficult to observe. The remolded surface is inseparable from the calculated ideal surface, which indicates that the low level of roughness of such a surface is incapable of increasing the injected current density. On the other hand, the two calculations for the rough and roughest abraded surfaces show the biggest increases, but as the local field distribution can be lowered due to the field dependent bulk conductivity, the results calculated here may be over-estimated.

Next, Fowler-Nordheim injection was calculated using equation (27) for each point on the surface, and thereafter averaged using equation (23). The results are shown in Figure 68.

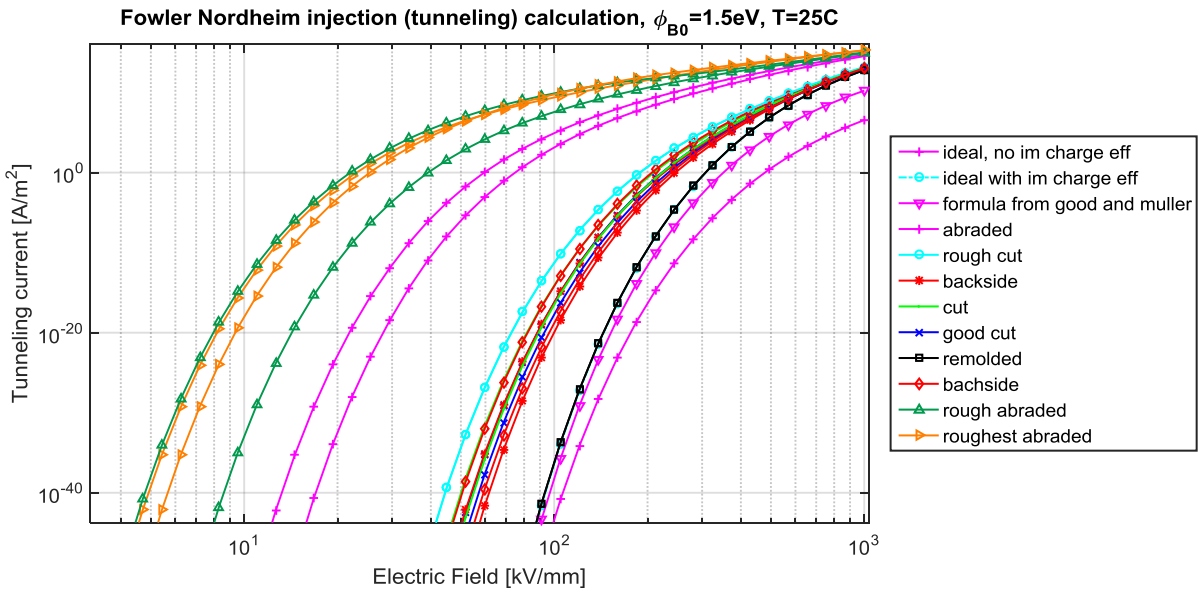

Figure 68. Fowler-Nordheim injection curves showing the impact of surface roughness for the different surface types.

Fowler-Nordheim injection is sensitive for surface roughness and increasing it shifts the injection current densities towards lower field levels. For the ideal surface, calculated without the impact of the image charge effect and temperature when using equation (25), a significantly lower current density is obtained as compared with a calculation at room temperature and with the image charge effect. The direct formula derived by Good and Muller [54] is also shown in the figure and provides a lower injected current density, but is only valid for field emission into vacuum.

The Fowler-Nordheim injection current densities were added to the Schottky current densities to obtain the total injected current densities. These are as shown in Figure 69, where the impact of barrier height, temperature and the image charge effect is illustrated.

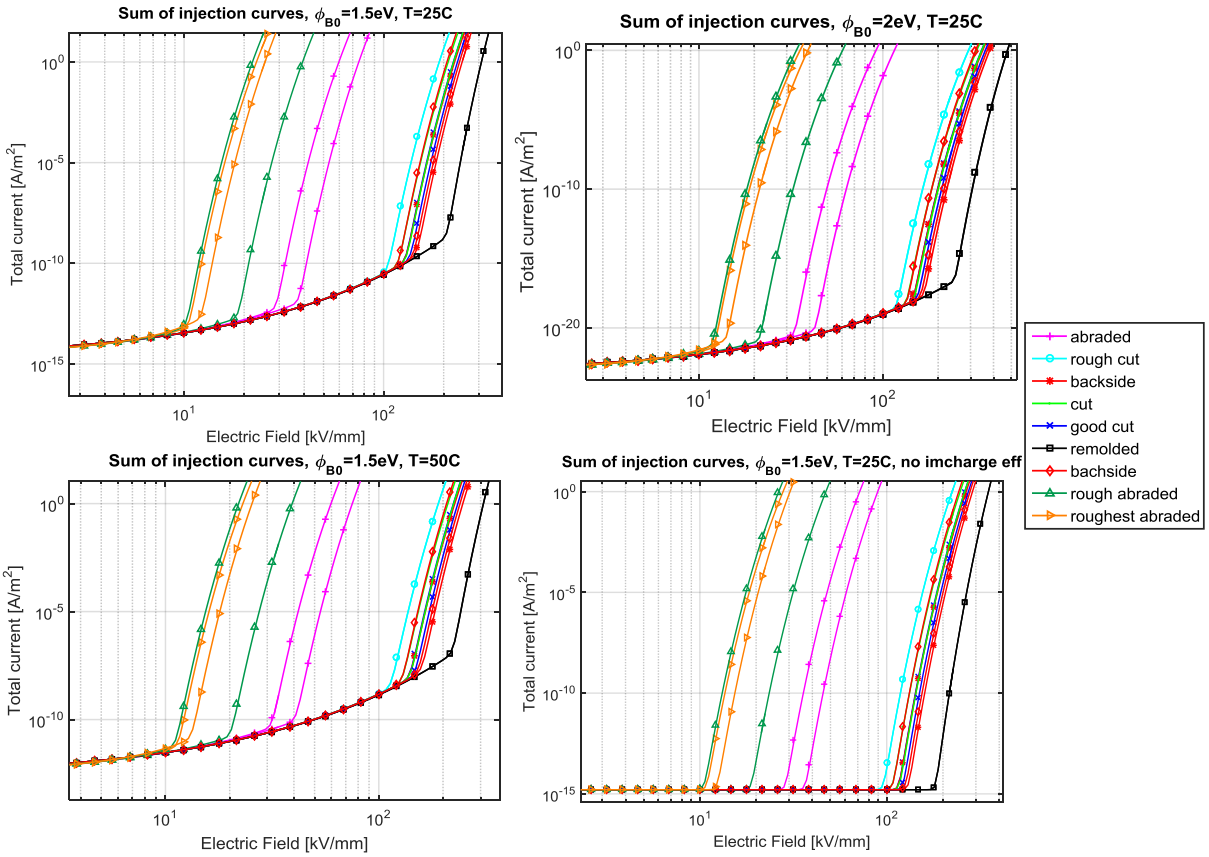

Figure 69. Sum of Schottky and Fowler-Nordheim injection showing the impact of barrier height (top right), temperature (bottom left) and the removal of image charge effect (bottom right).

The summed current densities show an additional threshold effect, which corresponds to the onset of Fowler Nordheim injection. This threshold effect seems to have a rather low sensitivity to the barrier height, temperature and image charge effect. Increasing the barrier height from 1.5 eV to 2 eV shifted the thresholds to higher field levels, and a lowering of barrier height should have an opposite effect. When the temperature was increased to 50 °C, the major effect was found in the Schottky curves, as Fowler-Nordheim injection has relatively low sensitivity to temperature and the inclusion of the temperature dependency introduced in equation (27). This was primarily done to provide a proper current density for room temperature, as this increased it by 2-3 decades in comparison to the current density at 0 K. Without the image charge effect, the field dependency for Schottky injection vanishes, but the onset of tunneling derived here remained at similar levels. This makes the threshold effect caused by the onset of Fowler-Nordheim injection persistent even for interfaces mated with air, oil, grease or other materials where permittivity is in the same order of magnitude as that of the insulation. The steep increase in current density above the threshold, could lead to significantly localized charge build up, which in turn would result in a lowering of the current density above the threshold. This would make the injected current density dependent on bulk conduction parameters and could make the current density to become bulk-limited. To investigate the localization of the charge injection process, the threshold field was found in the same manner as performed previously, but without calculating the average current from equation (23), but rather by finding the threshold field for each point on the surface separately, as shown in Figure 70.

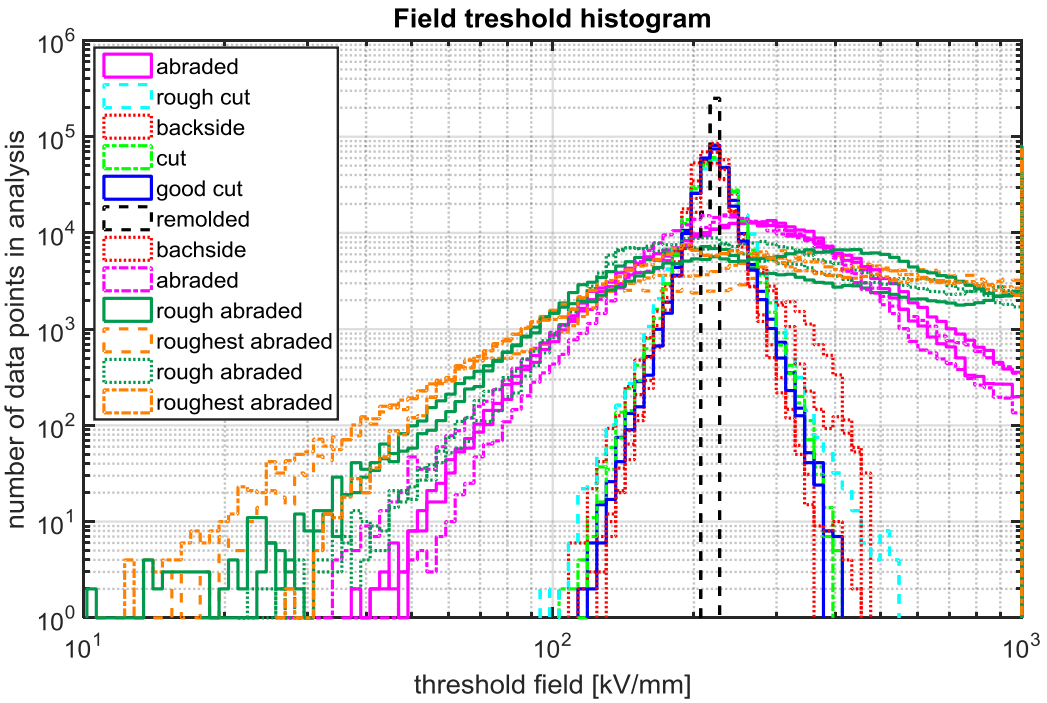

Figure 70. Histogram showing the possible onset of Fowler-Nordheim injection and the localization effect of charge injection.

Figure 70 shows that average current densities shown in Figure 69 are extremely localized to only a few points on the surface. The histogram also resembles the inverse of the FEF distribution shown in Figure 63, with a tail now flipped towards the left-hand side of the histogram. As the previously derived impact of field dependent bulk conductivity shifted the FEF distribution towards lower levels for the roughly abraded surfaces, and significantly reduced the magnitude of the difference in between these surface, a similar impact can be predicted for the threshold histograms. A similar yet less severe localization can be predicted to be present in the threshold effect of Schottky injection shown in Figure 67.

The localization of injected current density and the introduction of a threshold effect will be present for any injection law which has an exponential field dependency. The results shown in this section estimated the threshold effects for the Schottky injection and Fowler-Nordheim injection, but the effects shown could prevail even for a realistically modelled injection barrier including the impact of surface and bulk states. The exact field thresholds calculated here could be higher because of field dependent bulk conduction effects, but if a lower barrier height is used in addition, the same field level would remain. For this reason, no further calculation of these effects has been performed, as exact curve fitting and fine tuning will not further improve our understanding without detailed knowledge about the impact of bulk and surface states, and the physical relation between these injection curves and the observed breakdown phenomena.

5.3 FEF distribution for local defects

The previously shown lowering of the tail in the FEF distribution, caused by field dependent conductivity, showed dependency on surface geometric parameters. This could even be stronger for larger defects and protrusions. It is not the purpose of this work to calculate the exact impact of any defect, but its impact needs to be evaluated to see how the FEF distribution of an abraded surface distinguishes itself from an impact of a single local defect at various field levels. The defect was created artificially by adding a cylindrical indent with spherical tip, with radius *r*

and depth *z*, into the surface profile of a previously obtained backside surface. The resulting surface structure is shown in Figure 71 below.

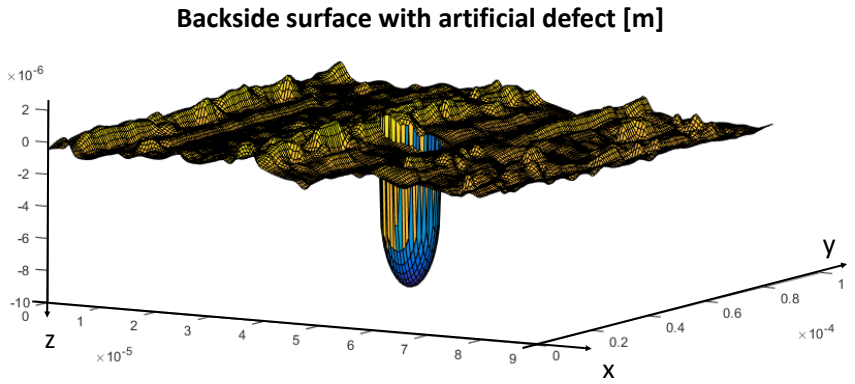

Figure 71. Surface profile of backside surface with added spherical indent with a 5 μm radius and 5 μm depth to the center of the sphere.

The same calculations as previously used ones were performed to obtain the respective FEF distributions and the results are shown in Figure 72 below, compared against the surface without defect.

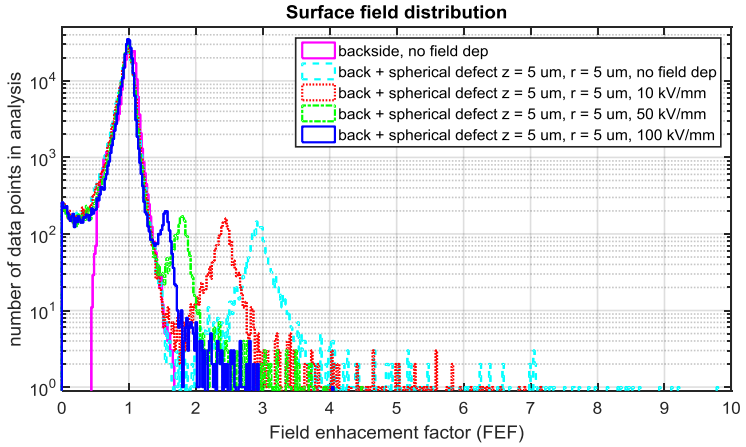

Figure 72. FEF distribution of backside surface with a 5 μm spherical indent at various field levels.

The addition of the defect resulted in a tail in the FEF distribution, along with a second peak. The tail originated from points around the circumference of the spherical defect, while the secondary peak was created by points located within the circumference. The tail and secondary peak were reduced in magnitude by the field dependent conductivity, and shifted to lower field enhancement levels when higher electric field was applied in the simulation. Adjacent points on the surface next to the defect were significantly reduced in magnitude, which also can be observed in the histogram.

Next, the sphere radius was reduced to 2 μm to confirm the influence of defect shape on the field distribution as shown in Figure 73.

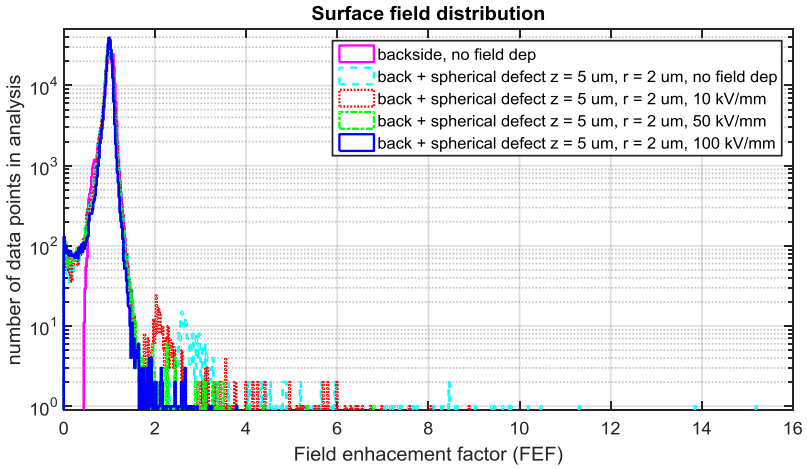

Figure 73. FEF distribution of backside surface with a 2 µm spherical indent at various field levels.

For the FEF distribution from a smaller defect, the distribution tail and the secondary peak remained present with similar magnitude, but with fewer data points. These findings indicate that the distribution tail can be related to the high derivatives in the surface profile, while the size of the defect itself could relate to surface area that is subjected to high field.

In comparison to previously obtained FEF distributions, when the measurement area is increased on rough surfaces, the FEF distribution will keep the same shape. For a single defect on the other hand, the distribution tail will shrink in amount (not in position), when the measurement area is increased. These are hardly any unexpected findings, but the implications they have on the injected current density is important. The averaged injected current density for a surface with a defect will remain low (given a small enough defect and large enough surface area), while a rough surface will give an increased current density independent of the surface area it is measured over. Looking close to a surface defect, higher electric fields and higher current density will be found than for a rough surface. Small surface defects can always be observed in real cable interfaces, but in DC, such defects are known to be significantly shielded and can lead to far higher breakdown levels compared to the rough interfaces tested in this thesis [76].

Chapter 6

Discussion

This discussion starts with an overview of the limitations in the presented study, after which the hypotheses, defined in section 2.4, are revisited and evaluated. It ends by trying to use the best fitting hypothesis to explain the observed phenomena in the electrical tests.

6.1 Limitations in the study

For optical profilometry, the surface was gold sputtered for three minutes to get a good reflection on the surface. This was longer than the gold sputtering used for the SEM, which was one minute. There is a small possibility that the longer sputtering time affected the surface structure to some degree, but the main features of the surface remained comparable to the SEM observations (Figure 31 and the profilometry results in Figure 59). Also, some additional tests with different sputtering times showed no deviating trends for the valid data points amongst these measurements. Some of the roughness results presented in this thesis have been compared against measurements obtained at different sites (Sintef and Nexans Lyon), using different measurement setups, for which the same roughness levels were found after the removal of the 3rd polynomial plane.

The contact angle measurements and calculated in this thesis surface energies showed some indicative trends, but had serious limitations in accuracy due to the quality of the setup. The results obtained on rough surfaces also showed an impact of the texture itself, which caused big deviation in the SFE depending on observation direction, as a global roughness parameter was used in the calculation. The usefulness of this measurement type to accurately determine physical surface properties which could be useful for charge injection simulations is therefore questionable.

The byproducts measured on the samples showed an overall low content in the cable peelings. It was also shown that the content was further reduced during storage time. It is not believed that a difference in storage time could have affected the results of the electrical measurements in this thesis. As the DCBD test results on cable peelings showed the same trends as the MV cable test results, it is believed that the breakdown effect has been recreated in the cable peeling test, and that the byproduct content has no significant contribution towards this breakdown level. To obtain incontrovertible proof of this assumption is however rather difficult, as increasing the byproduct content in the peeling tests and preventing outgassing during electrical testing is impossible without significant changes in the electrode design.

For the FTIR-ATR measurements, some interesting features were found for the abraded and the remolded surface. These findings could relate to the physical features of these surface types. For the abraded surface, the ever so slightly broadening of the carbonyl indicative peaks is an example, but will need additional verification by a separate measurement method. The double peak development on the remolded surface is an indication of a surface morphology change, which could be verified with differential scanning calorimetry (DSC) measurements. Also, the exact relation between space charge properties and these surface features will need further

attention, as multiple scenarios, as indicated in Table 3, can be considered, such as the formation of an extraction barrier, or alteration of the injection barrier height.

The surface charge decay measurements showed some interesting trends, but did suffer from unstable measurement equipment, which could have resulted in variation of the needle-sample and the probe-sample spacing. As the measurements were carried out in the alphabetic sample name order (A, B, C, …, Z, AA, BB, …) showed in legend of the figures, and no increasing/decreasing trends were observed against subsequent testing, it is believed that any gradual change in spacing and environmental conditions within the test cell can be ruled out.
The samples tested in the charge decay measurements all consisted of a gold sputtered ground electrode. As such a surface is not found in the HVDC cable system, a comparison against more realistic interface types, such as a chemical insulator-semiconductor and a physical insulator-semiconductor interface, should be performed. These tests are yet to be carried out to verify that these measurement results are applicable/comparable to the interfaces found in HVDC cable systems.

Most of the DC breakdown tests on cable peelings were performed with a physical aluminum-oil-insulation interface towards ground and with a physical insulation-oil-steel interface towards the high voltage electrode. These surfaces were significantly different from the interfaces in the MV cable end, which were a chemical semiconductor-insulation and an insulation-air interface. As per hypothesis A, the polymer surface type (e.g. abraded, cut) and its roughness is believed to be the main contributor towards the low breakdown strengths observed. The interface type could be a secondary effect capable of shifting the relevant phenomena towards higher or lower field levels depending on the created injection barrier height and other parameters.
The simulations of electric field distribution in the cable peeling, predicted a spreading of the electrical field to a greater area around the bearing ball, which was also observed in the peeling breakdown tests. However, for breakdowns occurring 10 mm or further away from the symmetry axis, it could have been the case that that the electric field at the breakdown position was lower than the electric field at the central axis due to the tangential electric field along the sample surface. To accurately estimate the electric field at such a position is not possible without an accurate bipolar charge model, so the use of the applied electric field at the central location is the best approach. It was observed that the breakdowns occurring further away were not caused by locally thinner sample thickness or defects on the ground electrode. Small pits were found from previous breakdowns, significantly limited in size by the current limiting resistor. The bearing ball electrode itself was free from pitting as the ball itself reoriented itself in its fixture, and was changed three times during the experiments.

The limitation in the FEF calculations, performed in section 5.2, is that the estimated FEF distributions correspond to the electric field perpendicular to the surface (the tangential field is zero as the surface is modelled with ground potential as the boundary condition). When this distribution is used to calculate the averaged charge injection from the electrode (z direction), the averaged injection does not account for the local variations in directions of electric field. While this could influence localized charge distribution it is believed that the effect is minimal.

The limitations in the injection calculations performed in section 5.3, arise from the simplification of the injection process, where the impact of surface states is neglected. Anyhow, some degree of validity should remain in the derived current densities for a chemical interface towards a material of higher permittivity, as the presence of image charge potential should result in significant thermal or electrical activation being required for an electron to inject or tunnel

into the insulator. For physical interfaces with interstitial material of similar permittivity to the insulator, or for surfaces towards oil or air, the Fowler-Nordheim contribution remains valid, while the Schottky contribution becomes questionable, as this will result in elimination of field dependency. Whether injection from a real interface lacking image charge effect is truly without field dependency below the onset of tunneling, can be questioned, but is in this work merely a result of neglecting of surface state impact in the injection process.

6.2 Discussion on Hypotheses

To put the proposed hypotheses from section 2.4 into new light, they should be evaluated based on the findings presented this thesis. For a hypothesis to show validity it should therefore explain most of these results. For explanation of all the observed effects, it is likely that additional effects not yet considered need to be taken into account.

The breakdown in the MV-sized cable test:

- Originated from the prepared cable surface.
- Occurred at low field levels slightly above the onset of charge injection for the abraded surface.
- Occurred at significantly higher field levels for smoother surfaces.
- Showed discharge channels in a cylindrical layer below the surface at high field levels.
- Occurred close to the SC break for rough surfaces, and for smooth surfaces it occurred within a wider area.

The breakdown in the peeling tests:

- Occurred at around 450 kV/mm for smooth surfaces.
- Occurred at around 205 kV/mm for the abraded ground surface.
- Occurred at around 205 kV/mm for the rough abraded ground surface.
- Occurred at around 180 kV/mm for the gold sputtered abraded ground surface.
- The breakdown field level showed no impact on peeling thickness in the range of 0.1 - 0.3 mm for the abraded ground sample.
- Occurred systematically away from the ball electrode for all samples with a rough ground electrode.

The charge decay process showed:

- Little impact of roughness orientation towards needle and probe surface.
- Significant impact of rough ground electrodes, through an increase in the decay speed against the reference above the threshold field levels:
    - Abraded: $21 < E_{th} < 32$ kV/mm, likely around 30 kV/mm
    - Rough abraded $21.5 < E_{th} < 31$ kV/mm, likely around 29 kV/mm
    - Roughest abraded $E_{th} < 21$ kV/mm

6.2.1 Hypothesis A – Roughness enhanced injection

Hypotheses A-1 and A-2, roughness enhanced injection, are supported by the results found in the charge decay measurements. Similar field threshold effects were observed both in the measurements and in the calculations. Also, the FEF distributions for the abraded and rough abraded surfaces became similar when high enough electric field was applied and the field dependent bulk conductivity was considered, which explains why the abraded and rough abraded surfaces showed similar breakdown levels. The lowering of breakdown level of the gold sputtered surface can be explained by a lowering of the injection barrier height, which

should move the field threshold to slightly lower levels. The systematic failure away from the bearing electrode could be explained by a different charge distribution at this location.

There is strong evidence for Hypothesis A, but the exact origin of the breakdown phenomenon is still unclear, which makes choosing between Hypothesis A-1 and A-2, and also other space charge related breakdown effects difficult. An attempt for explaining the breakdown process is made in section 6.3

6.2.2 Hypothesis B – Formation of extraction barrier

Hypothesis B, the formation of extraction barrier, could explain why abraded ground and rough abraded ground yielded similar results, as in both cases the roughness could have been significant enough to decouple the polymer surface from the image charge potential from the adjacent electrode. The increase in decay speed observed in the charge decay process is not supported by this hypothesis, but also, only chemical interfaces with gold sputtered ground electrodes were tested, for which this theory is not applicable. The main observations that show lack of support for this hypothesis is the systematic failure away from the ball electrode for abraded ground electrode, and the reduction of the breakdown field for the gold sputtered abraded ground. By changing this hypothesis to a situation where the extraction barrier is formed from localized surface states (which could originate from the slight increase of carbonyl groups on the abraded surface observed with FTIR-ATR), the extraction barrier could remain valid also for chemical interfaces, and explain a similar breakdown level of the gold sputtered ground abraded surface. This would on the other hand make the hypothesis contradict the results from the charge decay measurement.

6.2.3 Hypothesis C – Treeing initiation due to field enhancements

Hypothesis C-2, treeing initiation originating from interstitial material can be eliminated. The breakdown test on the chemical gold-sputtered abraded ground sample, could have no electric field in the cavities in between the gold sputtered surface and the aluminum ground electrode, but showed no increase in breakdown voltage. Also, changing the roughness from abraded to rough abraded showed no impact on breakdown field, even though this increased the roughness magnitude twofold and would have resulted in significant increase in cavity size.

Hypothesis C-1, treeing initiation caused by the local electric field distribution, without any impact from the developed space charge density, is more difficult to eliminate. As the calculated FEF distributions for the abraded and rough abraded surfaces became similar when the field dependent conductivity was considered, the similarity in breakdown fields for these surfaces is supported in this theory. While the tail of the abraded FEF distribution is located at 2 for the peeling test breakdown level, and at around 3-5 for MV-cable end breakdown field levels, there is no direct scaling observed from the impact of field dependent conductivity, but such a scaling effect could also originate from other effects. What this hypothesis cannot explain is the systematic failure away from the ball bearing electrode for the abraded ground surface and lowering of breakdown field level for the gold ground surface.

6.2.4 Hypothesis D – MWS charge due to electrode decoupling

Hypothesis D, MWS charge due to electrode decoupling can be eliminated on the same basis as for hypothesis C-2. The twofold change in roughness between rough abraded and abraded should in this case have resulted in a different magnitude of accumulated interfacial charge, and affected the breakdown voltage, which was not observed.

6.3 Proposed explanation – extension of hypothesis A

In this section, the space charge dynamics and breakdown phenomena are further discussed. This discussion is important as the nature of the breakdown phenomenon and charge distribution will influence the required methodology for any future modelling. It also identifies and further defines additional tests that may lead to an improvement of our understanding.

6.3.1 Extending the hypothesis

The cause of the breakdown due to the localized electric field and enhanced charge injection can be encompassed by different theories. If the breakdown is related to the localized field itself, such as described in hypothesis C-1, the breakdown could be of electronic nature (intrinsic or avalanche breakdown) or a localized thermal breakdown [33]. While this explains the origin of the breakdown from the rough surface, it cannot explain that localized defects, such as analyzed in section 5.3, can be sustained at field levels exceeding the breakdown level for the abraded surface. Therefore, the explanation should include the space charge effects. If the breakdown on the other hand is created by charge packets and propagation, such as described in hypothesis A-2, this has implications as the origin of the breakdown should start from the rough surface. This is also where such a charge packet would originate from, but an intrinsic or avalanche breakdown might be initiated first a certain distance from the insulator surface, or from the other electrode. The focus is therefore on hypothesis A-1, as it is the only one capable of explaining the systematic and repeatable breakdown phenomenon observed for rough surfaces.

The validity of hypothesis A-1 depends on how significant the accumulated charge can be close to the rough surface. As mentioned previously, the charge density needs to be 10^{22} m^{-3} or 10^{20} m^{-3} for exceeding the shallow or deep trap density respectively. Exceeding or at least coming close to these charge densities is a requirement for initiating ionizing collisions with the polymer matrix through hot electron degradation [34]. These values translate to a charge densities of 16 000 Cm^{-3} and 160 Cm^{-3} respectively. As such charge densities are extremely high, it should be evaluated if they can be accumulated locally or globally.

6.3.1.1 Global 1-dimensional approach

The injected current density, charge distribution, and field distribution is shown in Figure 74 considering a unipolar charging process. The field threshold E_{th} is here dependent on the surface type and roughness.

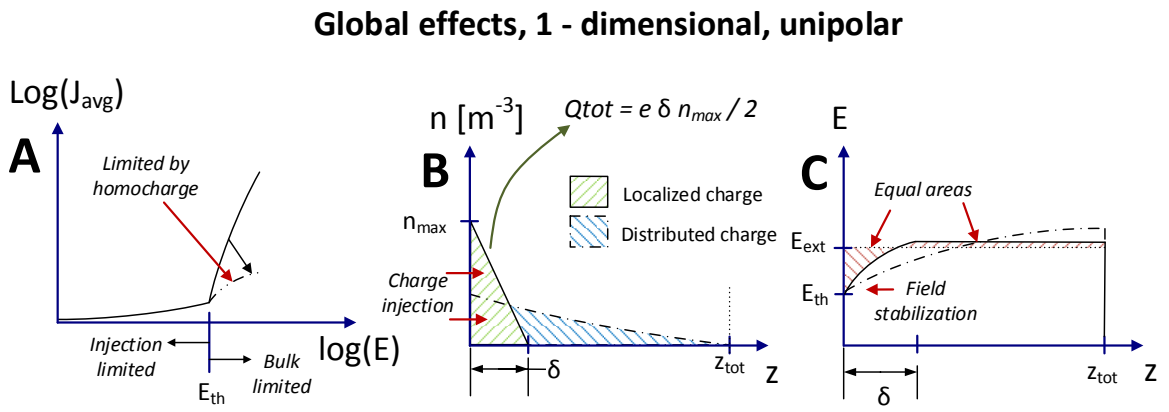

Figure 74. Unipolar global charge effects of roughness enhanced injection. The averaged injected current density against external field (A), charge profile (B) and field distribution (C) are shown for evaluating the effect of the injected charge. z is the spatial dimension of the sample.

When the field threshold is globally exceeded (A), charge injection will become bulk limited. This means that any increase in externally applied electric field over the threshold level will result in accumulation of homocharge (B), which in turn reduces the electric field at the injecting surface, stabilizing the field at the threshold level (C) (equation (37)).

$$\frac{dE_z}{dz} = \frac{e}{\varepsilon_0 \varepsilon_r} n(z) \tag{37}$$

Here E is the applied electric field and n is charge density profile in m^{-3}. A problematic aspect with adopting a 1-dimensional approach is that the calculated field thresholds E_{th} (originating from the FEF distributions) can increase when the charge locally shields the asperities of rough surfaces. Such an effect cannot be taken into account here as it will require a 2 or 3-dimensional model. In such a case, equation (37) will no longer hold, as the charge density is not uniform in the other *(x-y)* dimensions. Whether the FEF distribution can be shielded or not is further investigated in section 6.3.1.3. However, the global perspective can still to some extent explain why local defects are less problematic than rough surfaces. If spacing between local surface defects is high enough, the tail in the FEF distribution histogram will be of low significance in comparison to the overall distribution and the resulting average field threshold will be higher than for a rough surface.

The charge accumulation will not affect the external potential applied over the insulation. If the penetration depth δ in Figure 74 is comparable to sample thickness z_{tot}, the electric field at the opposite electrode will increase. This may lead to increased charge injection form the opposite electrode, such that a bipolar approach needs to be adopted. The slope of *n(z)* will become limited, due to a drift of the injected homocharges. For thin samples, such as cable peelings, it is thus more likely that the charge is distributed along sample thickness, giving rise to charge recombination within the sample, and limiting the charge amount accumulated close to the abraded surface. For thicker specimens, such as MV cables or full-size HVDC cables, it is likely that the field shift towards the opposite electrode is insignificant. This causes the injected homocharge layer to grow until a breakdown occurs when it locally exceeds the deep trap or shallow trap density.

6.3.1.2 Local 3-dimensional approach

For the local approach, the charge injection from an abraded asperity is compared to a single local defect. A surface defect can locally start injecting high amounts of charge at lower external field, but the effects can no longer be studied in one dimension as the local approach will result in the charge spreading also in the *x* and *y* dimensions, as shown in Figure 75.

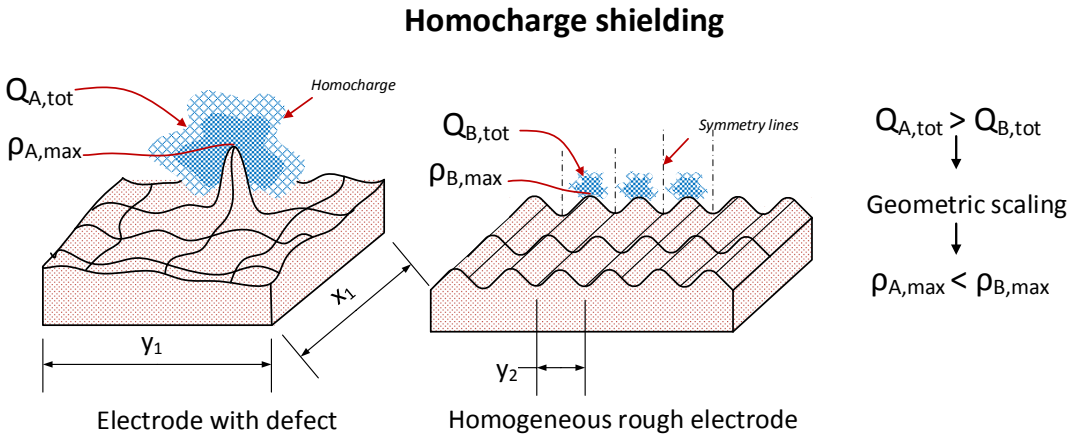

Figure 75. Three dimensional homocharge distribution adjacent to a surface defect or a heterogeneous rough surface.

As seen in Figure 75, the volume onto which the charge can be spread is likely to be higher for a localized defect as for a rough surface. While a point defect can benefit from three-dimensional charge spreading, a cut defect in the *x* direction will only benefit in two dimensions *(y, z)*. Also a homogeneous rough surface will benefit from the spreading in two dimensions *(y, z)* if the surface texture consists of striations in the *x* direction, which has been observed for nearly all surface types in this thesis. Since the area, or width over which the total charge Q_{tot} can spread can be significantly different $y_2 << y_1$, this will result in a higher charge density ρ_{max} for the rough asperity, despite of having a lower field enhancement factor than a local surface defect. The injected current density, charge distribution, and field distribution are now shown in Figure 76 from a local perspective for an abraded asperity or a local defect.

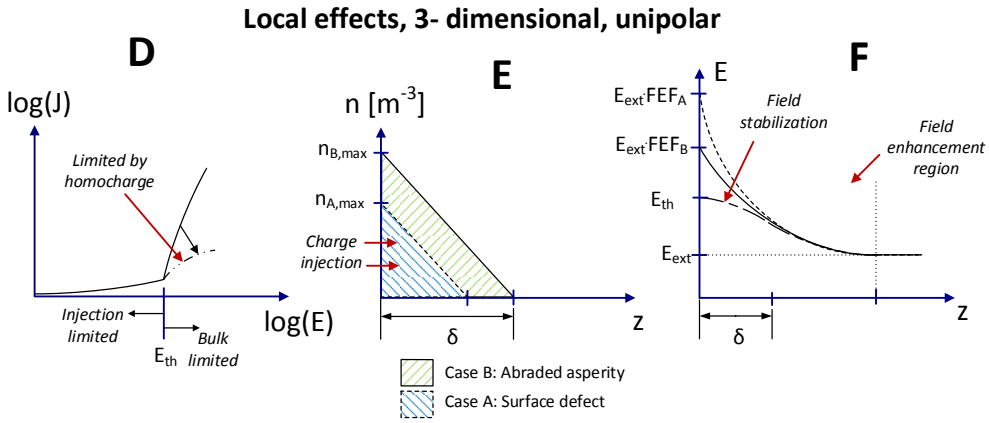

Figure 76. Unipolar local charge effects for a local defect or an abraded asperity. The injected current density against local field (D), charge profile (E) and local field distribution (F) are shown for evaluating the effect of the injected charge. z is the spatial dimension of the sample.

For the local approach, the field threshold E_{th} will be set at a certain level, independent of surface roughness, such as at the onset of tunneling. As seen in Figure 70, this threshold level

could be around 200 kV/mm, as this is center of the distribution. The local electric field is found by multiplying the external field E_{ext} with the FEF. From a local 3-dimensional perspective, the severity of the rough surface is therefore also related to geometric effects, which can result in a locally higher charge density. This clearly points out that the observed breakdown phenomenon must be closely related to the density of injected charge, and not solely to the level of electric field.

6.3.1.3 Exceeding the trap density

The total amount of charge that can be injected, before the field is significantly reduced is limited. The penetration depth δ of the injected charge layer therefore needs to be evaluated further, as reaching a charge density high enough for exceeding the deep trap density is only feasible if it is limited to a thin area towards the rough surface. For a charge density equal to the deep trap density or the shallow trap density, the resulting field reduction depends on the thickness of such a layer, as shown in Figure 77. The charge density profile is approximated with a triangular shape with maximum density at the electrode n_{max} and with width δ, as it is schematically drawn in Figure 74-B and Figure 76-E. The penetration depth δ is assumed to be low in comparison to the sample thickness, making the field reduction at the electrode proportional to the total charge within the triangular shape. This also assumes that the injected charge density below the field threshold is negligible in comparison to that injected above the field threshold, and only unipolar charge is considered.

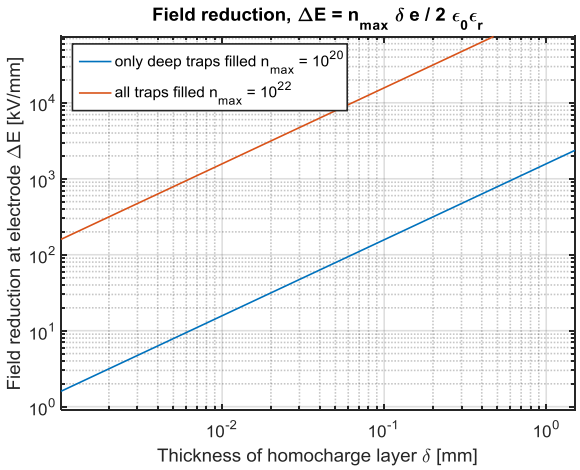

Figure 77. Field reduction at the electrode due to a thin charge layer assuming a triangular charge distribution within this layer.

Two observations can be made from the figure. The first observation is considering that if the FEF distribution is to be shielded from the charge distribution along the surface of the sample, the spacing between striations or defects is of importance. As previously indicated in Figure 75, for homogeneous rough surfaces the spacing (as indicated with the symmetry lines) can be in the range of 20 μm, while for defects this distance can be larger; in the range of 0.1-1mm. If a surface field discrepancy of around 30 kV/mm is to be smoothened out, this will need a local charge density exceeding the deep trap density (>160 Cm^{-3}) for the rough surface, while for the local defect this can be done with a charge density below the deep trap density. For rough surfaces, the main part of the FEF distribution should therefore remain and the field threshold should only increase with a few kV/mm before the deep trap density is exceeded.
The second observation is that the thickness of the charged layer should be significantly limited in the z direction into the sample. If we assume that the breakdown occurs only a few kV/mm above the field threshold level, the penetration depth δ, with similar charge density as the deep

trap density, is limited to only a few μm. Such low spreading of a high charge density (160 Cm^{-3}) is unrealistic as both drift and diffusion should contribute to spreading of this charge layer beyond a few μm. The exact breakdown of rough surfaces will therefore likely be a local phenomenon, and low conductivity of the material is a contributing factor.

6.3.1.4 Final remarks

The extended hypothesis proposed here consists of many simplifications and assumptions. It is thus proposed to evaluate it carefully in future work with a bipolar charge model and in the light of the observations made in this work. Parameters such as trapping rates, the exact charge injection equation accounting for surface states (not only use of Schottky equation with Fowler-Nordheim threshold effect), field dependent charge mobility, and many other parameters must be considered before any solid conclusions can be made. The discussion here implies that a global model alone cannot fully explain the breakdown effect, but should be able to provide somewhat realistic charge and current densities. Hamed et al [75] used a global bipolar model for polyethylene and found an initial homocharge density of 100 Cm^{-3} shortly after stepwise application of an electric field of 100 kV/mm, resulting in a field reduction of 40 kV/mm. Jihuan et al [77] obtained a maximal homocharge density of 20 Cm^{-3} for an external field of 120 kV/mm with a field reduction of 20 kV/mm. For both the references, the use of thin specimens (100 μm) resulted in recombination stabilizing the magnitude of accumulated charge. They used Schottky injection equation with the barrier heights in the range of 1.2 eV and tested only its minor variations (0.02 eV - 0.14 eV). The significant impact on charge injection from local field enhancements, as found in this work, should thus not be underestimated in the capability to cause premature failure at low field levels.

6.3.2 Applying the hypothesis

The list of observations presented in section 6.2, can now be again evaluated using the modified hypothesis. This is done first for the results of MV cable breakdown test, next for the cable peeling breakdown test and at last for the SPD measurement.

6.3.2.1 Proposed explanation for MV cable breakdown tests

For the MV cable breakdown tests, the similarities between measured breakdown levels and the calculated field threshold levels are striking and indicate that triggering of localized breakdowns takes place at the cable insulation surface shortly after the threshold field has been exceeded. For the abraded surface, the charge penetration depth δ is low enough for there not to be any observable traces in a cylindrical layer close to the surface. For the smoother surfaces, the charge penetration depth δ should be high enough for there to be a significant space charge accumulation away from the surface capable of creating the charge traces. In the latter case, the breakdown level has weak dependency on external materials and nature of the interface, as the injection mechanism works independent and even without the impact of the image charge effect. The localization of the breakdown channels close to the SC break for rough surfaces can be related to that the external field is low, giving a low dependency of bulk conductivity for the longitudinal field to spread out, and since the homocharge potential towards the surface could consist of a few kV, the first millimeters should have rather low longitudinal field. As the smooth surfaces have a higher field threshold, and a lower FEF distribution, the homocharge build up will spread further into the bulk. This requires that the applied electric field needs to exceed the threshold field by more for the breakdown to be initiated. This causes the insulation length subjected to $E > E_{th}$ to increase, and the breakdown to occur wherever the local charge density is the highest towards the surface. One should note that the longitudinal field was in the

range of 0.05-0.3 kV/mm during the tests and the radial electric field was approximately 300 times higher in its magnitude. The breakdown process is illustrated in Figure 78.

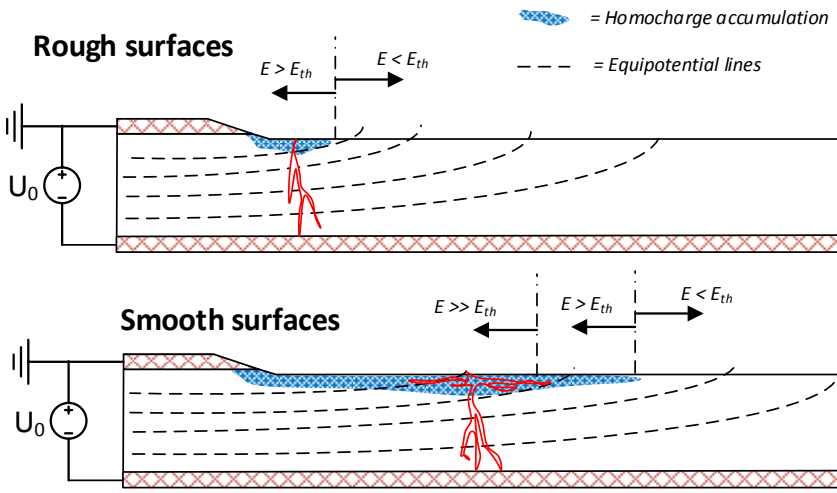

Figure 78. Proposed explanation of the breakdown process and charge distribution in the MV cable breakdown test

The hypothesis is thus capable of explaining the MV cable breakdown test. Also, localized defects will not influence the test significantly as these are to some degree shielded. The remolded surface showed lower breakdown values, yet a similar shape of the breakdown as the cut surface despite having an ideal FEF distribution. As mentioned earlier, this could originate from alteration of the injection barrier height due to the changed surface morphology, but also other effects could be possible.

6.3.2.2 Proposed explanation for cable peeling breakdown tests

For the breakdown tests on cable peelings, due to the low sample thickness in the range of 100 to 300 µm, the space charge accumulation can no longer be unipolar, as the injected homocharge from a rough surface will contribute to a field shift towards the opposite electrode, which in turn should lead to an increase in opposite charge injection. Also, due to field dependent charge mobility, the carrier transit time will be low through the sample. This would result in a bipolar space charge distribution. The total charge density that can be obtained at the rough surface is therefore limited, by charge extraction at the opposite electrode, opposite charge injection resulting in recombination, and a maximal gradient in the charge density profile. The limitation of the charge density at the rough surface results in that the field threshold can be exceeded significantly. The external current density is not necessarily high, as the homocharge accumulation results in a stabilization effect, but should increase once strong recombination takes place within the sample. This effect could be measurable in conduction current, but since a sphere-plane geometry was used in the breakdown test and the noise level was high, the effect could not be seen in the experiment. To explain the observed breakdown levels and breakdown position, the sphere-plane geometry and assumed charge densities are schematically shown in Figure 79.

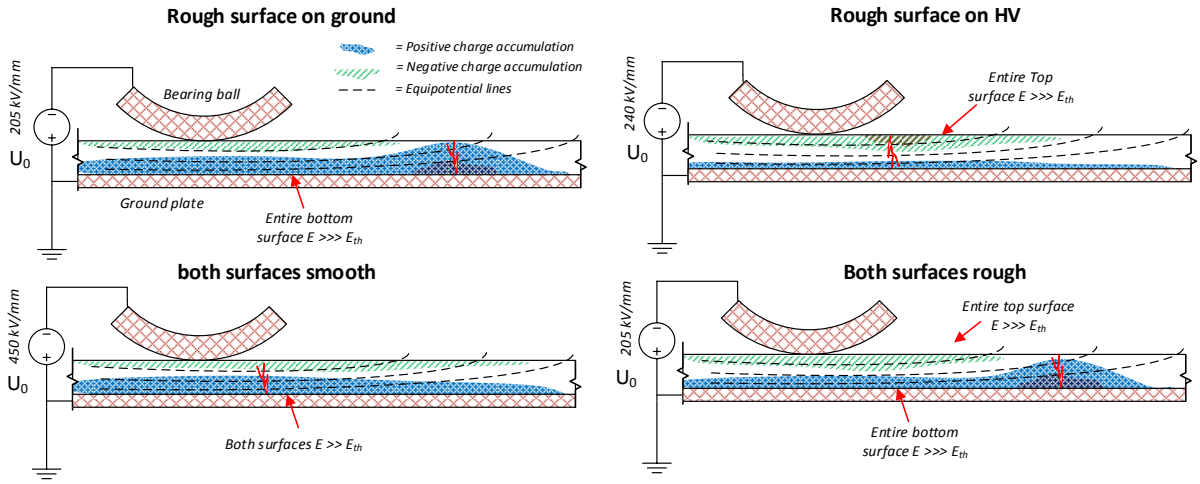

Figure 79. Schematic illustration of the proposed breakdown process and charge distribution in the cable peeling breakdown tests.

As shown in Figure 79, there should be a strong homocharge accumulation in the breakdown test, which makes the field distribution difficult to predict. For rough ground surfaces (top left), positions away from the bearing ball could either have less negative charge injection, or less positive charge extraction from the top surface, due to the geometric location, which could explain the systematic occurrence of the breakdown away from the ball electrode. As the positive charge growth is less restricted away from the ball electrode, the failure can occur due to high electric field towards the top surface, or exceeding the trap density at the bottom surface. For the samples with two rough surfaces (bottom right), very similar breakdown behavior was observed, indicating that the charge spreading from the ball electrode over the sample surface and through the oil could have been limited in both cases. For the abraded surface on high voltage side (top right), somewhat higher breakdown voltage was observed, along with some of the failures occurring under the ball electrode. As now opposite charge injection and extraction from the bottom surface was not limited by the geometry, the charge growth towards the top surface was more restricted, and there was no longer a systematic failure away from the ball bearing electrode. For smooth top and bottom surfaces (bottom left), a failure ultimately occurred due to high field or high local charge distributions, and occurred close to the electrode, as it is mentioned earlier that the field dependent bulk conductivity could limit the radial spreading of the electrical field, giving a field dependent upper limit to the distance between the bearing ball and breakdown location.

The low thickness dependency of the breakdown field for the rough-ground surfaces in the range of 100 to 300 μm as shown in Figure 45, is normally an indication of an injection limited process. The increase in thickness should have led to less field inversion towards the top electrode, less opposite charge injection, followed by a higher charge density towards the bottom electrode, ultimately leading to slightly lower breakdown fields for thicker samples. Explaining this exactly remains to be done with future modelling, as it involves the geometric field distribution in the setup.

6.3.2.3 Proposed explanation for the SPD measurements

For explaining the surface potential decay measurements in the light of the new hypothesis, a distinction needs to be made between the poling phase and subsequent measurement phase. During the poling phase, -10 kV was applied to the needle, leading consistently to -8 kV of surface potential, given that the needle-sample spacing was fixed. The surface potential is attributed to a layer of negative charge deposited into a layer with thickness δ. The poling phase,

related charge and field distributions, and the same charge distributions after stabilization are illustrated in a simplified manner in Figure 80.

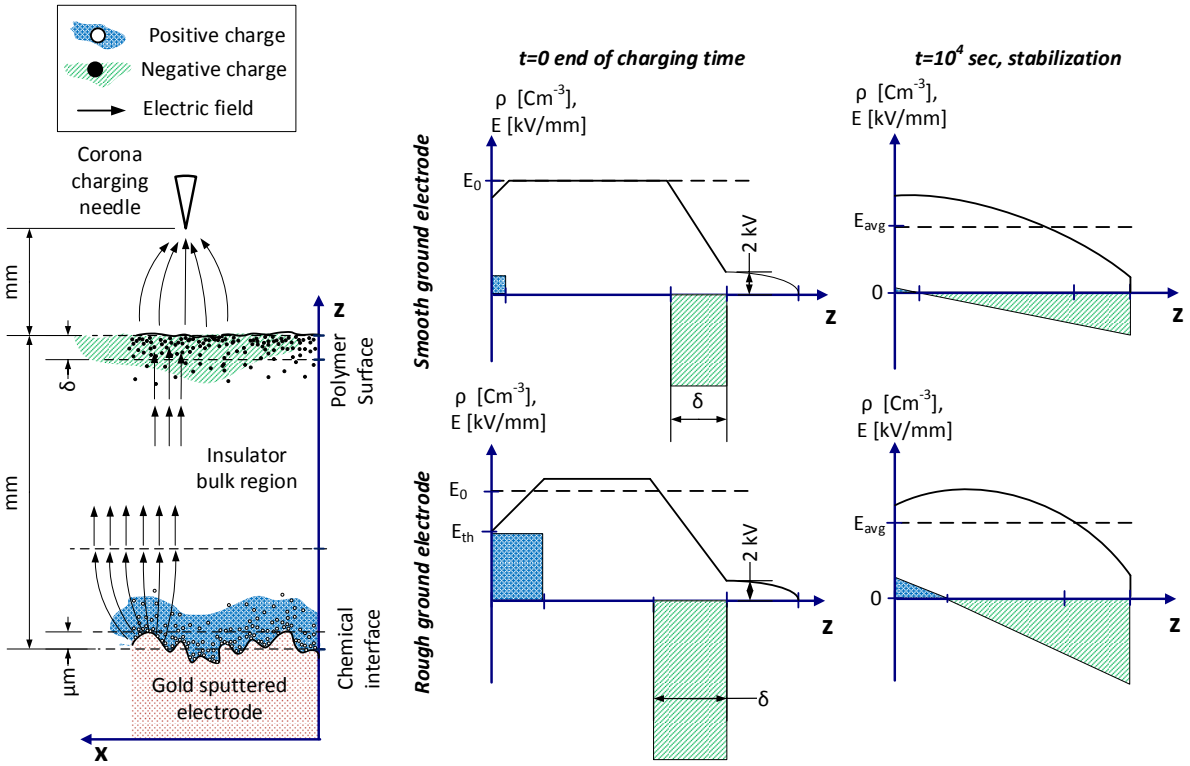

Figure 80. Proposed explanation of the electric field and space charge effects in the surface potential decay measurements.

As seen in Figure 80, there is a difference in space charge distributions for a rough ground surface, as significant opposite charge injection will occur if the threshold field is exceeded. During the poling phase, the positive charge injection from the bottom electrode results in an increase in the electric field in the bulk region over the average poling field E_0. As the surface is consistently subjected to ionized air particles, the surface potential can be assumed to be fixed at -8 kV. Any reduction to this surface potential during the poling phase, will result in more charge being deposited on the surface. This will lead to a higher positive and negative charge distribution in the sample, despite of using the same poling field E_0. After the poling phase, the sample is moved away from the needle, and the top surface is no longer at a fixed potential. Initially there will be a high charge propagation until the two charge fronts meet, and further decay is stabilized. The propagation of the two charge fronts will begin directly after the start of the poling and can be sensitive to various parameters. After stabilization, the decay speed is governed by the remaining charge distribution. The more positive charge that has been injected from the ground electrode, the more total charge will be in the system after the stabilization, resulting in a higher decay speed. By decreasing the thickness of the specimens, the average bulk electric field during the poling is increased, which allowed to find the threshold field E_{th} in the experiments for the rough surfaces. The thickness decrease for the smooth samples also increases the decay speed, as some increase in positive charge injection can occur, but also the thickness reduction can create a steeper charge profile after the stabilization time. The threshold found at around 20 kV/mm for smooth surfaces can therefore be related to both the charge injection from the ground electrode and to the bulk conduction effects, but the increase of the decay speed above this threshold is low as compared to the increase obtained with rough-ground surfaces.

In the light of the new hypothesis the field decay curves, Schottky plots and Poole-Frenkel plots can be fully explained. Coming back to sample C, which had a significant defect on the ground electrode, a high initial decay speed was observed after which it stabilized and behaved similar to the other samples. As the FEF distribution of a sample with a defect on ground can have a significant tail even when field dependent bulk conductivity is considered, there would have been a strong charge injection from the defect. As this charge is localized to the area around the defect and not across the entire bottom surface, as shown in Figure 75, the decay characteristics will be similar once the injected charge around the defect has been neutralized.

Chapter 7

Conclusions

This chapter summarizes the major outcomes of the work. After the major findings have been summarized, the applicability of the findings are also put into perspective.

7.1 Conclusions of the work

The main finding of this work has been the further development of hypothesis A-1, Roughness enhanced charge injection leading to locally high charge densities, as discussed in section 6.2 and section 6.3. As the electrical measurements have only assessed external quantities, such as average breakdown fields and surface potential, the promising outcome of this hypothesis needs further evaluation before any solid conclusions can be made about the exact process involved in the observed breakdown characteristics. A breakdown process initiated at electrodes with severe homocharge accumulation, is not a commonly observed and discussed phenomenon within research, and the findings in this work could create a framework for better understanding of this subject.

Surface roughness is a measurable surface quantity that can be assessed accurately with simple means. For high voltage applications, surface roughness within the mesoscale shown in Figure 5, can be commonly found and will result in field localization towards the surface. A normally distributed surface roughness will yield a FEF distribution with a tail towards higher electric field values as shown in Figure 81. An additional finding is that the exact surface structure has an effect in itself, which was shown when the roughness variation of cut surfaces showed less impact on the FEF distribution than expected. For the three different abraded surface types, there was an impact of the surface roughness, but this impact disappeared once the field dependent bulk conductivity had been taken into account, and disappeared only if high enough field was applied. This phenomenon was also observed in the SPD measurements. The FEF distribution is thus not fully a feature of the surface only, in addition there is an impact of bulk properties, which unfortunately introduces a field dependency in the FEF distribution itself. If this is not fully understood it complicates the comparison of test results obtained for different materials, geometries and field levels.

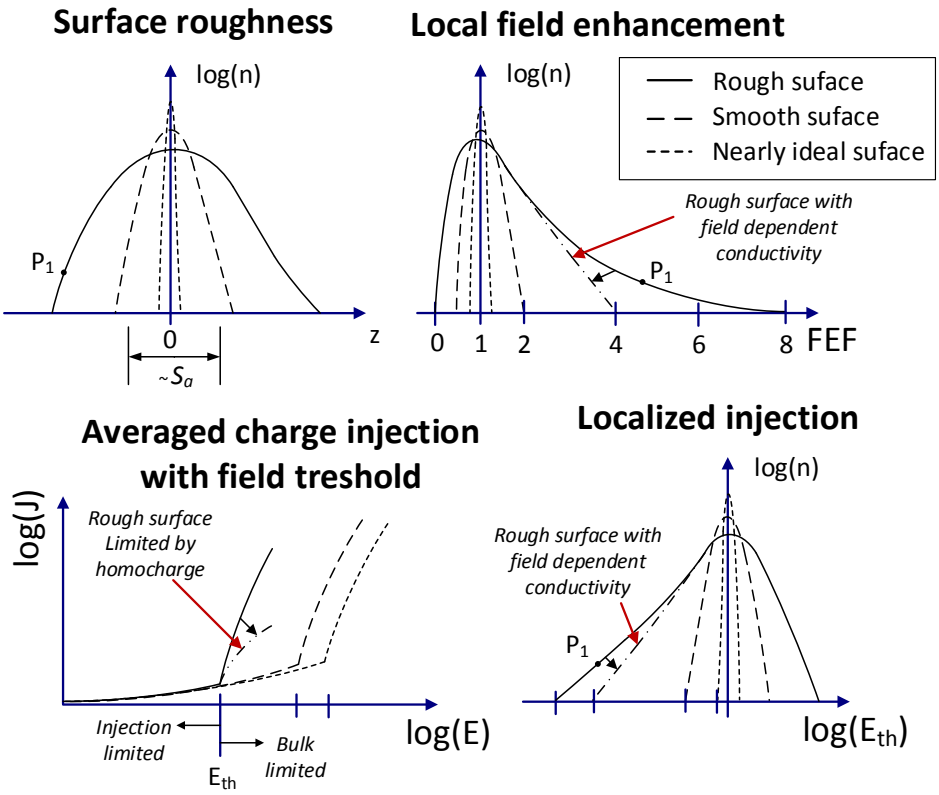

Figure 81. Schematic illustration showing the relation between the surface roughness histogram, the local field enhancement histogram, charge injection and the charge localization histogram. The same data point P_1 is indicated in the histograms.

The FEF distribution will certainly influence charge injection, as shown in Figure 81. Depending on the exact field dependency in any derived injection equation, the FEF distribution will localize and increase the injected current density, given that the FEF distribution is significant. Problematically, the impact on charge injection cannot be summarized with a fixed parameter added on in the equation, but requires a thorough analysis of the surface roughness and bulk properties of the material. If the injected current density is assumed to follow a combination of Schottky and Fowler-Nordheim injection laws, with similar barrier heights in their expressions, a distinct field threshold can be found. This field threshold will also be present in other injection equations, but is very clear when Fowler-Nordheim tunneling is considered. Below the threshold, at low electric fields, the effect is nearly unnoticeable. Above the field threshold, a significant increase in charge injection can be expected, which can result in the current density to become bulk-limited. Having bulk-limited injection, will result in homocharge accumulation in the material. The threshold fields have been confirmed in this work by utilizing the ground electrode in the SPD measurements, and have been in line with the results of the modelling. The bipolar nature of the SPD measurement at high electric fields has therefore also been confirmed in this work.

The injection characteristics of a rough surface differs from localized defects or needle electrodes in that the shape of the FEF distribution remains the same independently on the surface area. This can reduce the shielding effect of rough surfaces, as homocharge accumulation cannot shift the field away from the rough asperities to the same degree as for a localized defect, which could make rough surfaces capable of strong charge injection.

As the ideal electrical property of any electrode interface in the HVDC system is to minimize charge injection, a high surface roughness is an undesired feature and should be reduced to a possible lowest level. Charge extraction capability is, on the other hand, the electrode characteristic that should be maximized, which is best achieved through maintaining the image charge effect and controlling the material properties in the material bulk.

7.2 Applicability of the results

The findings of this work are applicable for most of the material interfaces listed in Table 1, which are commonly found within the components of HVDC cable systems. The theoretical framework can however be extended onto other high voltage systems. As the bulk properties have been that of a well degassed commercial grade XLPE in this work, one should evaluate the relevancy of this theory depending on the bulk conduction properties in the system it is applied to.

For HVDC systems using other insulation materials the field dependency of their bulk conductivity is often a desired feature, as for example in field grading materials that provide better shielding of the FEF distribution. Nanoparticle based materials may on the other hand increase the robustness through the increase of the deep trap density, which stabilizes the injected homocharge given that electric field inversion is not required in the system.

Other high voltage industries, such as the capacitor film industry as well as manufacturing of dry type transformers and other maintenance free components using solid insulation types should have the same aim towards reducing surface roughness at interfaces in their applications. When it comes to gas and air insulated systems, the FEF distribution approach would remain valid, but as the insulation medium differs significantly, other additional aspects will affect charge and the injection/emission processes.

For HVAC applications, electric field is permittivity controlled such that the system is without shielding properties from field dependent conductivity and homocharge accumulation. This makes the estimation of the FEF distribution straightforward and applicable for all field levels. As charge injection is known to be involved in the initiation of the electrical treeing process in polyethylene [78], there is also a desire to assess the FEF distribution and strive towards lowering the roughness for robust HVAC applications.

When it comes to other research areas, the most common sample type is the press molded plate. The roughness in such a configuration is likely very low (given that high-quality press films have been used), which could lead to unforeseen scaling effects when using a different surface type in the final application. The cable peeling is therefore superior, as it shares its interfaces with the application, but does require sophisticated practical skills for obtaining accurate and stable dimensions of the samples. Extruded small scale samples such as the one tested in the DCBD tests in this work shown and in Figure 44, could have a certain degree of roughness depending on the quality of the die. Electrical measurements on such samples should therefore be corrected for roughness if the applied electric fields are high.

Chapter 8

Future Work

The future research to be performed is divided into gathering further proof and understanding about the hypothesis proposed in this thesis. Further, other charge injection properties are identified that require development of their understanding.

8.1 Extending understanding of the involved BD phenomenon

Further proof of the exact nature of the charge distribution and the breakdown phenomenon is required. The best way for obtaining this knowledge is through space charge measurements. A commonly known technique is the pulsed electroacoustic measurement (PEA), which should be capable of detecting the global homocharge accumulation when the field threshold has been exceeded. Specific design of the test setup will be required to adapt it for the cable peeling geometry and for ensuring that high enough electric field can be applied in the measurement.

Bipolar charge simulations will be required to further elucidate the global (macroscopic) and local (microscopic) space charge distributions, and pinpoint the exact nature of the breakdown process of rough interfaces. As spatial dimensions will make it difficult to construct a model that encompassed both the global insulation behavior and the local injection behavior, the two systems might need to be separated from each other. A global one-dimensional model will be the best starting point capable of determining the space charge distributions for small and large samples. To exactly identify whether local electron avalanches or hot electron degradation is the initiator of the breakdown, a local two- or three-dimensional model with the electrode profile accounted for could be the most accurate approach.

Conductivity measurements may further increase our understanding. As it is anticipated that the homocharge shielding will initially not lead to significant external current densities, the field threshold will need to be exceeded enough so that it can be identified in the external current measurement due the increased charge recombination within the test sample. This will put requirements on the electrode design as the balance of high field, low noise level, and avoidance of surface flashovers will need to be optimized.

Additional DCBD tests and charge decay measurements will be performed to investigate the applicability and nature of realistic interface types, such as samples including extruded semiconductor-insulation interfaces or physical joint semiconductor–insulation ones. Materials with higher trap densities could be analyzed to check if they also feature the field threshold effect and improve or reduce the breakdown level of rough surfaces. One topic that has been covered very little in this thesis is temperature dependency. This will introduce a slight difference in the field dependent bulk conductivity and its impact on the FEF distribution, but it could also be used to understand more about the charge injection process. If the measured field threshold has low dependency on temperature, it can confirm the contribution of Fowler-Nordheim injection. Also, the impact of polarity should be further studied.

As there are a lot of parameters and their combinations to investigate, the corona charging of the charge decay measurement could be replaced with a thin fixed electrode in contact with the

surface. This would eliminate the deposited corona charge, and by measuring on the polymer surface in the near vicinity of the permanent electrode, the field threshold could be identified by a sudden drop in the surface potential while slowly increasing the voltage. Finding the threshold field would then only require a single sample, and could be done within short time, in contrast to the current setup, where it requires around 6 samples and 6 weeks of work.

8.2 Investigating additional factors influencing charge injection

Some interesting features were found on the remolded samples in the FTIR-ATR measurements, which could be further investigated as they can provide more information about the impact of surface morphological properties on electrical interfacial effects.

Other investigations could encompass investigating the relation between surface states and charge injection. Different interface types may be prepared, and the new understanding of surface roughness and FEF distributions could be used to determine the threshold fields of chemically altered surfaces with known heterogenous surface structures. In this way, the impact of surface states and metal work functions could be investigated from an alternative perspective, without usage of the highly questioned Schottky injection law.

Further improvements will be made to the peeling process, to ensure that thin, high quality peelings can be obtained from the surface and bulk of any high voltage cable, independent of its geometrical perfection. So far the peeling procedure has shown to be the superior method to obtain samples from short cable sections for estimating their electrical properties. The peeling process can have many purposes in the high voltage cable industry besides the measurements performed here. Such electrical applications, being destructive for the sample to be analyzed, can be for quality control, insulation degradation assessment or bulk space charge assessment using the SPD measurement.

References

[1] "BP Energy Outlook, Energy economics, BP Global." [Online]. Available: http://www.bp.com/en/global/corporate/energy-economics/energy-outlook.html. [Accessed: 06-Jun-2017].

[2] "Electricity Map | Live CO2 emissions of electricity consumption." [Online]. Available: https://www.electricitymap.org/?page=country&solar=false&remote=true&wind=false&countryCode=DK-DK1. [Accessed: 13-Mar-2018].

[3] "Cross-Linked Polyethylene (XLPE) Cables - Nexans." [Online]. Available: http://www.nexans.no/eservice/Norway-en/navigate_342597/Cross_Linked_Polyethylene_XLPE_Cables.html. [Accessed: 09-Jun-2017].

[4] "Nexans supplies 320 kV cables for 'DolWin6' offshore DC link to TenneT - Nexans." [Online]. Available: http://www.nexans.com/eservice/Corporate-en/navigatepub_0_-35910_297_40_11229/TenneT_awards_Nexans_a_100_million_worth_contract_.html. [Accessed: 01-Aug-2017].

[5] T. Worzyk, "Submarine Power Cables: Design, Installation, Repair, Environmental Aspects," *Power Syst.*, vol. 39, 2009.

[6] N. G. McCrum, C. P. Buckley, and C. B. Bucknall, *Principles of polymer engineering*. .

[7] M. Hao, A. Fazal, A. S. Vaughan, G. Chen, Y. Zhou, and C. Zhang, "The impacts of degassing on space charge characteristics and DC conductivity in semicon-bonded XLPE for HVDC cable applications," in *Annual Report - Conference on Electrical Insulation and Dielectric Phenomena, CEIDP*, 2016, vol. 2016–Decem, pp. 97–100.

[8] B. Crist and J. M. Schultz, "Polymer spherulites: A critical review," *Prog. Polym. Sci.*, vol. 56, pp. 1–63, May 2016.

[9] T. Andritsch, A. Vaughan, and G. C. Stevens, "Novel insulation materials for high voltage cable systems," *IEEE Electr. Insul. Mag.*, vol. 33, no. 4, pp. 27–33, Jul. 2017.

[10] S. Nilsson, T. Hjertberg, and A. Smedberg, "Structural effects on thermal properties and morphology in XLPE," *Eur. Polym. J.*, vol. 46, no. 8, pp. 1759–1769, Aug. 2010.

[11] U. H. Nilsson and J.-O. Bostrom, "Influence of the semiconductive material on space charge build-up in extruded HVDC cables," in *2010 IEEE International Symposium on Electrical Insulation*, 2010, pp. 1–4.

[12] D. Fabiani *et al.*, "Polymeric HVDC Cable Design and Space Charge Accumulation. Part 1: Insulation/Semicon Interface," *IEEE Electr. Insul. Mag.*, vol. 23, no. 6, pp. 11–19, Nov. 2007.

[13] P. Morshuis, "Interfaces: To be avoided or to be treasured? What do we think we know?," in *2013 IEEE International Conference on Solid Dielectrics (ICSD)*, 2013, pp. 1–9.

[14] L. C. Sawyer and D. T. Grubb, *Polymer Microscopy*. Dordrecht: Springer Netherlands, 1996.

[15] J. W. Carr and C. Feger, "Ultraprecision machining of polymers," *Precis. Eng.*, vol. 15, no. 4, pp. 221–237, Oct. 1993.

[16] K. Xiao and L. Zhang, "The role of viscous deformation in the machining of polymers," *Int. J. Mech. Sci.*, vol. 44, no. 11, pp. 2317–2336, Nov. 2002.

[17] M. Hasheminezhad and E. Ildstad, "Partial discharge inception of interface voids versus mechanical surface pressure," in *2010 International Conference on High Voltage Engineering and Application, ICHVE 2010*, 2010, pp. 397–400.

[18] Z. Yuanxiang, W. Yunshan, W. Ninghua, and S. Qinghua, "Effect of surface topography and morphology on space charge packets in polyethylene," *J. Phys. Conf. Ser.*, vol. 183, no. 1, p. 12009, Aug. 2009.

[19] M. Hasheminezhad and E. Ildstad, "Application of contact analysis on evaluation of breakdown strength and PD inception field strength of solid-solid interfaces," *IEEE Trans. Dielectr. Electr. Insul.*, vol. 19, no. 1, pp. 1–7, Feb. 2012.
[20] S. M. Hasheminezhad, E. Ildstad, and A. Nysveen, "Breakdown strength of solid|solid interface," in *Proceedings of the 2010 IEEE International Conference on Solid Dielectrics, ICSD 2010*, 2010, pp. 1–4.
[21] A. Haddad, D. F. Warne, and Institution of Engineering and Technology., *Advances in high voltage engineering*. Institution of Engineering and Technology, 2009.
[22] D. J. Lacks and R. Mohan Sankaran, "Contact electrification of insulating materials," *J. Phys. D. Appl. Phys.*, vol. 44, no. 45, p. 453001, Nov. 2011.
[23] P. Zhang, G. Fitzpatrick, T. Harrison, W. A. Moussa, and R. J. Zemp, "Double-SOI Wafer-Bonded CMUTs With Improved Electrical Safety and Minimal Roughness of Dielectric and Electrode Surfaces," *J. Microelectromechanical Syst.*, vol. 21, no. 3, pp. 668–680, Jun. 2012.
[24] E. Chibowski, "Surface free energy of a solid from contact angle hysteresis," *Adv. Colloid Interface Sci.*, vol. 103, no. 2, pp. 149–172, Apr. 2003.
[25] D. Jacek and K. Anna, "Comparison of Surface Free Energy Calculation Methods."
[26] M. Żenkiewicz, "Methods for the calculation of surface free energy of solids," vol. 24, 2007.
[27] I. A. Tsekmes, D. van der Born, P. H. F. Morshuis, J. J. Smit, T. J. Person, and S. J. Sutton, "Space charge accumulation in polymeric DC mini-cables," in *2013 IEEE International Conference on Solid Dielectrics (ICSD)*, 2013, pp. 452–455.
[28] D. Fabiani *et al.*, "HVDC Cable Design and Space Charge Accumulation. Part 3: Effect of Temperature Gradient [Feature article]," *IEEE Electr. Insul. Mag.*, vol. 24, no. 2, pp. 5–14, Mar. 2008.
[29] G. C. Montanari and P. H. F. Morshuis, "Space charge phenomenology in polymeric insulating materials," *IEEE Trans. Dielectr. Electr. Insul.*, vol. 12, no. 4, pp. 754–767, Aug. 2005.
[30] R. Bodega, P. H. F. Morshuis, E. Redjosentono, and J. J. Smit, "Dielectric Interface Characterization by Means of Space Charge Measurements," in *2003 Annual Report Conference on Electrical Insulation and Dielectric Phenomena*, 2003, pp. 728–733.
[31] C.Kitte, "Introduction to Solid State Physics." Wiley, p. 680, 1976.
[32] D. A. Neamen, *An introduction to Semiconductor devices*. McGraw-Hill, 2006.
[33] L. A. Dissado and J. C. Fothergill, *Electrical Degradation and Breakdown in Polymers*. P. Peregrinus, 1992.
[34] G. Teyssedre and C. Laurent, "Charge transport modeling in insulating polymers: from molecular to macroscopic scale," *IEEE Trans. Dielectr. Electr. Insul.*, vol. 12, no. 5, pp. 857–875, Oct. 2005.
[35] A. Moyassari, M. Unge, M. S. Hedenqvist, U. W. Gedde, and F. Nilsson, "First-principle simulations of electronic structure in semicrystalline polyethylene," *J. Chem. Phys.*, vol. 146, no. 20, p. 204901, May 2017.
[36] A. T. Hoang, Y. V. Serdyuk, and S. M. Gubanski, "Charge Transport in LDPE Nanocomposites Part II—Computational Approach," *Polymers (Basel).*, vol. 8, no. 4, p. 103, 2002.
[37] D. Min and S. Li, "Simulation on the influence of bipolar charge injection and trapping on surface potential decay of polyethylene," *IEEE Trans. Dielectr. Electr. Insul.*, vol. 21, no. 4, pp. 1627–1636, Aug. 2014.
[38] M. Fukuma, M. Nagao, and M. Kosaki, "Computer analysis on transient space charge distribution in polymer," in *Proceedings of 1994 4th International Conference on Properties and Applications of Dielectric Materials (ICPADM)*, vol. 1, pp. 24–27.

[39] O. Magen and N. Tessler, “On electrode pinning and charge blocking layers in organic solar cells,” *J. Appl. Phys.*, vol. 121, no. 19, p. 195502, May 2017.
[40] M. Kleefstra and G. C. Herman, “Influence of the image force on the band gap in semiconductors and insulators,” *J. Appl. Phys.*, vol. 51, no. 9, pp. 4923–4926, Sep. 1980.
[41] Y. Jiang, Z. An, C. Liu, F. Zheng, and Y. Zhang, “Influence of oxyfluorination time on space charge behavior in polyethylene,” *IEEE Trans. Dielectr. Electr. Insul.*, vol. 17, no. 6, pp. 1814–1823, Dec. 2010.
[42] D. M. Taylor and T. J. Lewis, “Electrical conduction in polyethylene terephthalate and polyethylene films,” *J. Phys. D. Appl. Phys.*, vol. 4, no. 9, p. 315, Sep. 1971.
[43] B. S. G. and R. H. F. T. E. Stern, “Further Studies in the Emission of Electrons from Cold Metals on JSTOR,” *Proc. R. Soc. London. Ser. A, Contain. Pap. a Math. Phys. Character*, vol. 124, no. 795, pp. 699–723, 1929.
[44] M. Taleb, G. Teyssedre, and S. Le Roy, “Role of the interface on charge build-up in a low-density polyethylene: Surface roughness and nature of the electrode,” in *2009 IEEE Conference on Electrical Insulation and Dielectric Phenomena*, 2009, pp. 112–115.
[45] N. Koenigsfeld, R. Kalish, A. Cimmino, D. Hoxley, S. Prawer, and I. Yamada, “Effect of surface roughness on field emission from chemical vapor deposited polycrystalline diamond,” *Appl. Phys. Lett.*, vol. 79, no. 9, pp. 1288–1290, Aug. 2001.
[46] L. J. Brillson, *Surfaces and interfaces of electronic materials*. Wiley-VCH, 2010.
[47] L. Chen, T. D. Huan, Y. C. Quintero, and R. Ramprasad, “Charge injection barriers at metal/polyethylene interfaces,” *J. Mater. Sci.*, vol. 51, no. 1, pp. 506–512, Jan. 2016.
[48] M. A. Baldo and S. R. Forrest, “Interface-limited injection in amorphous organic semiconductors,” *Phys. Rev. B*, vol. 64, no. 8, p. 85201, Aug. 2001.
[49] V. I. Arkhipov, E. V. Emelianova, Y. H. Tak, and H. Bässler, “Charge injection into light-emitting diodes: Theory and experiment,” 1998.
[50] D. Blossey, “One-dimensional Onsager theory for carrier injection in metal-insulator systems,” *Phys. Rev. B*, vol. 9, no. 12, pp. 5183–5187, Jun. 1974.
[51] P. R. Emtage and J. J. O’Dwyer, “Richardson-Schottky Effect in Insulators,” *Phys. Rev. Lett.*, vol. 16, no. 9, pp. 356–358, Feb. 1966.
[52] G. G. M. J.Campbell Scott, “Charge injection and recombination at the metal–organic interface,” *Chem. Phys. Lett.*, vol. 299, no. 2, pp. 115–119, 1999.
[53] R. H. Fowler and L. Nordheim, “Electron Emission in Intense Electric Fields,” *Proceedings of the Royal Society of London. Series A, Containing Papers of a Mathematical and Physical Character*, vol. 119. Royal Society, pp. 173–181.
[54] R. H. Good and E. W. Müller, “Field Emission,” Springer, Berlin, Heidelberg, 1956, pp. 176–231.
[55] Y. Chang, Z. Guo, A. Koneru, and Y. Wang, “Surface roughness realized and evaluated in different dimensional range and its effect on field emission behavior,” *Vacuum*, vol. 136, pp. 36–39, Feb. 2017.
[56] M. Taleb, G. Teyssedre, S. Le Roy, and C. Laurent, “Modeling of charge injection and extraction in a metal/polymer interface through an exponential distribution of surface states,” *IEEE Trans. Dielectr. Electr. Insul.*, vol. 20, no. 1, pp. 311–320, Feb. 2013.
[57] E. M. Conwell and M. W. Wu, “Contact Injection into Polymer Light-Emitting Diodes,” Feb. 1997.
[58] M. A. Abkowitz, H. A. Mizes, and J. S. Facci, “Emission limited injection by thermally assisted tunneling into a trap-free transport polymer,” *Appl. Phys. Lett.*, vol. 66, no. 10, pp. 1288–1290, Mar. 1995.
[59] S. Delpino, D. Fabiani, and G. C. Montanari, “High Space Charge Dynamics in EVA-based Nanocomposite Flat Specimens,” in *2008 Annual Report Conference on Electrical Insulation and Dielectric Phenomena*, 2008, pp. 137–140.

[60] T. J. Lewis, “Electrical Effects at Interfaces and Surfaces,” *IEEE Trans. Electr. Insul.*, vol. EI-21, no. 3, pp. 289–295, Jun. 1986.
[61] J. L. Hartke, “The Three-Dimensional Poole-Frenkel Effect,” *J. Appl. Phys.*, vol. 39, no. 10, pp. 4871–4873, Sep. 1968.
[62] P. N. Murgatroyd, “Theory of space-charge-limited current enhanced by Frenkel effect,” *J. Phys. D. Appl. Phys.*, vol. 3, no. 2, p. 308, Feb. 1970.
[63] H. Ghorbani, C. O. Olsson, A. Abbasi, and M. Saltzer, “Influence of press films on conduction in polyethylene plaque samples,” in *2016 IEEE International Conference on Dielectrics (ICD)*, 2016, pp. 1179–1182.
[64] L. A. Dissado *et al.*, “Characterizing HV XLPE cables by electrical, chemical and microstructural measurements on cable peeling: Effects of surface roughness, thermal treatment and peeling location,” *Conf. Electr. Insul. Dielectr. Phenom. (CEIDP), Annu. Rep.*, vol. 1, pp. 136–140, 2000.
[65] J. C. Fothergill *et al.*, “Electrical, microstructural, physical and chemical characterization of hv xlpe cable peelings for an electrical aging diagnostic data base,” *IEEE Trans. Dielectr. Electr. Insul.*, vol. 10, no. 3, pp. 514–527, Jun. 2003.
[66] N. Zebouchi, P. Carstensen, A. A. Farkas, A. Campus, and U. H. Nilsson, “Electric characterization of films peeled from the insulation of extruded HVDC cables,” in *CEIDP ’05. 2005 Annual Report Conference on Electrical Insulation and Dielectric Phenomena, 2005.*, pp. 79–82.
[67] S. Alam, Y. Serdyuk, and S. Gubanski, “Potential decay on silicone rubber surfaces affected by bulk and surface conductivities,” *IEEE Trans. Dielectr. Electr. Insul.*, vol. 22, no. 2, pp. 970–978, Apr. 2015.
[68] Y. Zhuang, G. Chen, and M. Rotaru, “Charge injection in gold ground electrode corona charged polyethylene film: Surface potential decay and corona charging current measurement,” in *2011 - 14th International Symposium on Electrets*, 2011, pp. 125–126.
[69] Y. Zhuang *et al.*, “Effect of ground electrode on charge injection and surface potential of corona charged polyethylene film,” *J. Electrostat.*, vol. 90, pp. 139–146, Dec. 2017.
[70] E. H. Doedens, N. B. Frisk, M. Jarvid, L. Boyer, and S. Josefsson, “Surface preparations on MV-sized cable ends for ramped DC breakdown studies,” in *2016 IEEE Conference on Electrical Insulation and Dielectric Phenomena (CEIDP)*, 2016, pp. 360–362.
[71] M. A. Brown, G. Chen, A. S. Vaughan, and P. A. Norman, “High voltage performance of bulk, and amalgamated, PE insulation systems. Part II. Breakdown, morphology and lifetime,” *J. Phys. D. Appl. Phys.*, vol. 36, no. 24, pp. 3197–3204, Dec. 2003.
[72] J. P. Coates, “The Interpretation of Infrared Spectra: Published Reference Sources,” *Appl. Spectrosc. Rev.*, vol. 31, no. 1–2, pp. 179–192, Jan. 1996.
[73] S. Deipino *et al.*, “Feature article - Polymeric HVDC cable design and space charge accumulation. Part 2: insulation interfaces,” *IEEE Electr. Insul. Mag.*, vol. 24, no. 1, pp. 14–24, Jan. 2008.
[74] Z. Li, N. Liu, S. Gabriel, and G. Chen, “Thermal ageing and its impact on charge trap density and breakdown strength in polyethylene,” in *2016 IEEE Conference on Electrical Insulation and Dielectric Phenomena (CEIDP)*, 2016, pp. 907–910.
[75] H. Boukhari and F. Rogti, “Simulation of Space Charge Dynamic in Polyethylene Under DC Continuous Electrical Stress,” *J. Electron. Mater.*, vol. 45, no. 10, pp. 5334–5340, Oct. 2016.
[76] E. Doedens, A. Johansson, M. Jarvid, S. Nilsson, M. Bengtsson, and J. Kjellqvist, “Effects of inclusions of oxidized particles in XLPE on treeing phenomena,” in *2012 Annual Report Conference on Electrical Insulation and Dielectric Phenomena*, 2012, pp. 597–600.
[77] J. Tian, Y. Zhou, and Y. Wang, “Simulation of space charge dynamics in low-density

polyethylene under external electric field and injection barrier heights using discontinuous galerkin method," *IEEE Trans. Dielectr. Electr. Insul.*, vol. 18, no. 5, pp. 1374–1382, Oct. 2011.

[78] T. Tanaka, "Space charge injected via interfaces and tree initiation in polymers," *IEEE Trans. Dielectr. Electr. Insul.*, vol. 8, no. 5, pp. 733–743, 2001.